

# Jordan Journal of Mechanical and Industrial Engineering (JJMIE)

JJMIE is a high-quality scientific journal devoted to fields of Mechanical and Industrial Engineering. It is published by Hashemite University in corporation with the Jordanian Scientific Research Support Fund.

## EDITORIAL BOARD

---

### Editor-in-Chief

Prof. Ahmed M. Al-Ghandoor

### Cukucpv/Gf lqqt

Dr. Mohammad A Gharaibeh.

### Editorial board

Prof. **Mohammad Ahmad Hamdan**  
University of Jordan

Prof. **Naseem Sawaged**  
Mutah University

Prof. **Amin Al Robaidi**  
Al Balqa Applied University

Prof. **Naser Al-Huniti**  
University of Jordan

Prof. **Mohammad Hayajneh**  
Jordan University of Science and Technology

## THE INTERNATIONAL ADVISORY BOARD

---

**Abu-Qudais, Mohammad**  
Jordan University of Science & Technology, Jordan

**Abu-Mulaweh, Hosni**  
Purdue University at Fort Wayne, USA

**Afaneh Abdul-Hafiz**  
Robert Bosch Corporation, USA

**Afonso, Maria Dina**  
Institute Superior Tecnico, Portugal

**Badiru, Adedji B.**  
The University of Tennessee, USA

**Bejan, Adrian**  
Duke University, USA

**Chalhoub, Nabil G.**  
Wayne State University, USA

**Cho, Kyu-Kab**  
Pusan National University, South Korea

**Dincer, Ibrahim**  
University of Ontario Institute of Technology,  
Canada

**Douglas, Roy**  
Queen's University, U. K

**El Bassam, Nasir**  
International Research Center for Renewable  
Energy, Germany

**Haik, Yousef**  
United Arab Emirates University, UAE

**Jaber, Jamal**  
Al- Balqa Applied University, Jordan

**Jubran, Bassam**  
Ryerson University, Canada

**Kakac, Sadik**  
University of Miami, USA

**Khalil, Essam-Eddin**  
Cairo University, Egypt

**Mutoh, Yoshiharu**  
Nagaoka University of Technology, Japan

**Pant, Durbin**  
Iowa State University, USA

**Riffat, Saffa**  
The University of Nottingham, U. K

**Saghir, Ziad**  
Ryerson University, Canada

**Sarkar, MD. Abdur Rashid**  
Bangladesh University of Engineering &  
Technology, Bangladesh

**Signer, Dennis**  
Wichita State University, USA

**Sopian, Kamaruzzaman**  
University Kebangsaan Malaysia, Malaysia

**Tzou, Gow-Yi**  
Yung-Ta Institute of Technology and Commerce,  
Taiwan

## EDITORIAL BOARD SUPPORT TEAM

---

### Language Editor

Dr. Qusai Al-Debyan

### Publishing Layout

Eng. Ali Abu Salimeh

## SUBMISSION ADDRESS:

---

Prof. Ahmed Al-Ghandoor, Editor-in-Chief  
Jordan Journal of Mechanical & Industrial Engineering,  
Hashemite University,  
PO Box 330127, Zarqa, 13133 , Jordan  
E-mail: jjmie@hu.edu.jo



Hashemite Kingdom of Jordan



Hashemite University

Jordan Journal of  
Mechanical and Industrial Engineering

JJMIE

*An International Peer-Reviewed Scientific Journal*  
*Financed by Scientific Research Support Fund*

<http://jjmie.hu.edu.jo/>

ISSN 1995-6665

# Jordan Journal of Mechanical and Industrial Engineering (JJMIE)

JJMIE is a high-quality scientific journal devoted to fields of Mechanical and Industrial Engineering. It is published by The Jordanian Ministry of Higher Education and Scientific Research in corporation with Hashemite University.

**Introduction:** The Editorial Board is very committed to build the Journal as one of the leading international journals in mechanical and industrial engineering sciences in the next few years. With the support of the Ministry of Higher Education and Scientific Research and Jordanian Universities, it is expected that a heavy resource to be channeled into the Journal to establish its international reputation. The Journal's reputation will be enhanced from arrangements with several organizers of international conferences in publishing selected best papers of the conference proceedings.

**Aims and Scope:** *Jordan Journal of Mechanical and Industrial Engineering* (JJMIE) is a refereed international journal to be of interest and use to all those concerned with research in various fields of, or closely related to, mechanical and industrial engineering disciplines. *Jordan Journal of Mechanical and Industrial Engineering* aims to provide a highly readable and valuable addition to the literature which will serve as an indispensable reference tool for years to come. The coverage of the journal includes all new theoretical and experimental findings in the fields of mechanical and industrial engineering or any closely related fields (Materials, Manufacturing, Management, Design, Thermal and Fluid, Energy, Control, Mechatronics, and Biomedical). The journal also encourages the submission of critical review articles covering advances in recent research of such fields as well as technical notes.

## Guide for Authors

---

### **Manuscript Submission:**

High-quality submissions to this new journal are welcome now and manuscripts may be either submitted online or email.

**Online:** For online and email submission upload one copy of the full paper including graphics and all figures at the online submission site, accessed via <http://jjmie.hu.edu.jo>. The manuscript must be written in MS Word 2010 Format. All correspondence, including notification of the Editor's decision and requests for revision, takes place by e-mail and via the Author's homepage, removing the need for a hard-copy paper trail.

### **Submission address and contact:**

Prof. Ahmed Al-Ghandoor  
Editor-in-Chief  
*Jordan Journal of Mechanical & Industrial Engineering*,  
Hashemite University,  
PO Box 330127, Zarqa, 13115, Jordan  
E-mail: [jjmie@hu.edu.jo](mailto:jjmie@hu.edu.jo)

**Types of contributions:** Original research papers and Technical reports

**Corresponding author:** Clearly indicate who is responsible for correspondence at all stages of refereeing and publication, including post-publication. Ensure that telephone and fax numbers (with country and area code) are provided in addition to the e-mail address and the complete postal address. Full postal addresses must be given for all co-authors.

**Original material:** Submission of an article implies that the work described has not been published previously (except in the form of an abstract or as part of a published lecture or academic thesis), that it is not under consideration for publication elsewhere, that its publication is approved by all authors and that, if accepted, it will not be published elsewhere in the same form, in English or in any other language, without the written consent of the Publisher. Authors found to be deliberately contravening the submission guidelines on originality and exclusivity shall not be considered for future publication in this journal.

**Withdrawing:** If the author chooses to withdraw his article after it has been assessed, he shall reimburse JJMIE with the cost of reviewing the paper.

### **Manuscript Preparation:**

---

**General:** Editors reserve the right to adjust style to certain standards of uniformity. Original manuscripts are discarded after publication unless the Publisher is asked to return original material after use. Please use MS Word 2010 for the text of your manuscript.

**Structure:** Follow this order when typing manuscripts: Title, Authors, Authors title, Affiliations, Abstract, Keywords, Introduction, Main text, Conclusions, Acknowledgements, Appendix, References, Figure Captions, Figures and then Tables. Please supply figures imported into the text AND also separately as original graphics files. Collate acknowledgements in a separate section at the end of the article and do not include them on the title page, as a footnote to the title or otherwise.

**Text Layout:** Use 1.5 line spacing and wide (3 cm) margins. Ensure that each new paragraph is clearly indicated. Present tables and figure legends on separate pages at the end of the manuscript. If possible, consult a recent issue of the journal to become familiar with layout and conventions. All footnotes (except for table and corresponding author footnotes) should be identified with superscript Arabic numbers. To conserve space, authors are requested to mark the less important parts of the paper (such as records of experimental results) for printing in smaller type. For long papers (more than 4000 words) sections which could be deleted without destroying either the sense or the continuity of the paper should be indicated as a guide for the editor. Nomenclature should conform to that most frequently used in the scientific field concerned. Number all pages consecutively; use 12 or 10 pt font size and standard fonts.

**Corresponding author:** Clearly indicate who is responsible for correspondence at all stages of refereeing and publication, including post-publication. The corresponding author should be identified with an asterisk and footnote. Ensure that telephone and fax numbers (with country and area code) are provided in addition to the e-mail address and the complete postal address. Full postal addresses must be given for all co-authors. Please consult a recent journal paper for style if possible.

**Abstract:** A self-contained abstract outlining in a single paragraph the aims, scope and conclusions of the paper must be supplied.

**Keywords:** Immediately after the abstract, provide a maximum of six keywords (avoid, for example, 'and', 'of'). Be sparing with abbreviations: only abbreviations firmly established in the field may be eligible.

**Symbols:** All Greek letters and unusual symbols should be identified by name in the margin, the first time they are used.

**Units:** Follow internationally accepted rules and conventions: use the international system of units (SI). If other quantities are mentioned, give their equivalent in SI.

**Maths:** Number consecutively any equations that have to be displayed separately from the text (if referred to explicitly in the text).

**References:** All publications cited in the text should be presented in a list of references following the text of the manuscript.

*Text:* Indicate references by number(s) in square brackets in line with the text. The actual authors can be referred to, but the reference number(s) must always be given.

*List:* Number the references (numbers in square brackets) in the list in the order in which they appear in the text.

**Examples:**

**Reference to a journal publication:**

[1] M.S. Mohsen, B.A. Akash, "Evaluation of domestic solar water heating system in Jordan using analytic hierarchy process". Energy Conversion & Management, Vol. 38 (1997) No. 9, 1815-1822.

**Reference to a book:**

[2] Strunk Jr W, White EB. The elements of style. 3rd ed. New York: Macmillan; 1979.

**Reference to a conference proceeding:**

[3] B. Akash, S. Odeh, S. Nijmeh, "Modeling of solar-assisted double-tube evaporator heat pump system under local climate conditions". 5th Jordanian International Mechanical Engineering Conference, Amman, Jordan, 2004.

**Reference to a chapter in an edited book:**

[4] Mettam GR, Adams LB. How to prepare an electronic version of your article. In: Jones BS, Smith RZ, editors. Introduction to the electronic age, New York: E-Publishing Inc; 1999, p. 281-304

**Free Online Color :** If, together with your accepted article, you submit usable color and black/white figures then the journal will ensure that these figures will appear in color on the journal website electronic version.

**Tables:** Tables should be numbered consecutively and given suitable captions and each table should begin on a new page. No vertical rules should be used. Tables should not unnecessarily duplicate results presented elsewhere in the manuscript (for example, in graphs). Footnotes to tables should be typed below the table and should be referred to by superscript lowercase letters.

**Notification:** Authors will be notified of the acceptance of their paper by the editor. The Publisher will also send a notification of receipt of the paper in production.

**Copyright:** All authors must sign the Transfer of Copyright agreement before the article can be published. This transfer agreement enables Jordan Journal of Mechanical and Industrial Engineering to protect the copyrighted material for the authors, but does not relinquish the authors' proprietary rights. The copyright transfer covers the exclusive rights to reproduce and distribute the article, including reprints, photographic reproductions, microfilm or any other reproductions of similar nature and translations.

**Proof Reading:** One set of page proofs in MS Word 2010 format will be sent by e-mail to the corresponding author, to be checked for typesetting/editing. The corrections should be returned within **48 hours**. No changes in, or additions to, the accepted (and subsequently edited) manuscript will be allowed at this stage. Proofreading is solely the author's responsibility. Any queries should be answered in full. Please correct factual errors only, or errors introduced by typesetting. Please note that once your paper has been proofed we publish the identical paper online as in print.

**Author Benefits:**

*No page charges:* Publication in this journal is free of charge.

*Free offprints:* One journal issues of which the article appears will be supplied free of charge to the corresponding author and additional offprint for each co-author. Corresponding authors will be given the choice to buy extra offprints before printing of the article.



---

<b>PAGES</b>	<b>PAPERS</b>
85 - 98	<b>Repowering Old Thermal Power Station by Integrating Concentrated Solar Power Technology.</b> <i>Taieseer Abu Rahmeh, Ahmad Abbas, Jamal Jaber, Aiman Alawin.</i>
99 - 104	<b>Computational Fluid Dynamics Simulation of Plate Fin and Circular Pin Fin Heat Sinks.</b> <i>Mohammad Saraireh</i>
105– 113	<b>Three-Dimensional Investigations of Stress Intensity Factors in a Rotating Thick-Walled FGM Cylinder.</b> <i>Hadi Eskandari</i>
115– 122	<b>Optimization of Resistance Spot Welding Process Parameters on Shear Tensile Strength of SAE 1010 steel sheets Joint using Box-Behnken Design.</b> <i>Shashi Dwivedi , Satpal Sharma</i>
123– 131	<b>Estimation Bending Deflection in an Ionic Polymer Metal Composite (IPMC) Material using an Artificial Neural Network Model.</b> <i>Bahaa Kazem , Jasim Khawwaf</i>
133– 140	<b>Conceptual Design of Congregational Prayer Chair .</b> <i>Farouk Daghistani</i>
141– 147	<b>Preparation and Corrosion Behavior of Bronze -40%w Composite.</b> <i>Malek Ali , Balakumeren Suppiah, Zaid Muayaduldeen</i>
149– 160	<b>Investigation of Local Hemodynamics Effect in Disturbed Flow Interactions.</b> <i>Abdullah Alshorman .</i>

---



# Repowering Old Thermal Power Station by Integrating Concentrated Solar Power Technology

Taieseer Abu Rahmeh<sup>a</sup>, Ahmad Abbas<sup>b</sup>, Jamal Jaber<sup>\*a</sup>, Aiman Alawin<sup>a</sup>

<sup>a</sup>Faculty of Engineering Technology, Al-Balqa' Applied University, Jordan

<sup>b</sup>Dept. of Mechanical Engineering, University of Wisconsin-Milwaukee, USA

Received 25 February 2016

Accepted 19 May 2016

## Abstract

The present study aims to investigate technical, economic and environmental aspects of integrating a Parabolic Trough Collector with existing feed-water heating system in an old "33 MW unit" in Al-Hussein Thermal Power Plant in Jordan. Such integration should improve the performance of the existing power plant and reduce the rate of fuel consumption, consequently the resultant pollutants, including Greenhouse Gases (GHG), emissions will be reduced. System Advisor Model software was used as a simulation tool in this study to optimize the required solar field aperture area and to predict the performance of employed solar system. Thermodynamic basic relations, energy and mass balances, are used to simulate various main components of the existing standard steam, Rankine, cycle. Different scenarios of feed-water heating arrangement with solar-replacement are presented and discussed. It was found that efficiency of the existing power unit could be increased by 3% due to higher turbine's output as a result of increased steam flow rate at later stages of the turbine. The estimated avoided GHG emissions exceed 10,000 ton CO<sub>2</sub> annually. But economics of such system may not be very attractive due to decreasing oil prices: at present the estimated payback period is more than 10 years.

© 2016 Jordan Journal of Mechanical and Industrial Engineering. All rights reserved

**Keywords:** Repowering, CSP, Solar Energy, Thermal Power Plants, Jordan.

## 1. Background

Concerns of security of energy supplies, fossil fuels prices and resultant negative environmental impacts are main drivers behind moving towards utilizing indigenous energy resources including renewables. This is typically the case in Jordan, which is a non-oil producing country with limited natural resources and totally dependent on imported energy from Gulf States and Egypt. Recently the regional political upheaval which caused instability in the whole MENA region had impacted Jordan economically through:

- The sharp drop in natural gas supplies from Egypt which led to a surge in Jordan's current account and fiscal deficits; and
- The large influx of refugees, especially from Syria, which increased the population by more than 25% and further straining Jordan's difficult fiscal position.

Thus, the Government of Jordan (GOJ) has taken few actions aiming to develop the energy sector to and promote energy efficiency in all sectors of the economy in order to reduce dependence on imported oil and gas. It is aimed to cut the current level of approximately 97%, while increasing the share of renewable energy meeting to 10% (i.e., 600-100 MW wind, 300-600 MW solar and 30-50 MW biomass) of energy demand by 2020 as reported by

the Minister of Energy and Mineral Resources at different occasions. However, in the past few years (2011-2014) electricity produced from renewable sources was less than 0.5% [1].

Among all renewable sources, solar and wind energy are most promising and could be used in green electricity generation. The annual solar intensity (2000-2500 kWh/m<sup>2</sup>) in Jordan is among the highest in the world which supports the development of solar based central power plants either by using PV or CSP technologies. At present there is a long list of PV projects, as central power plants, either connected to the grid or in the pipeline and soon will be completed. But CSP technology is still not deployed due to the fact that the required capital investment is very high compared with other renewable or non-renewable technologies. In this study, repowering of an old 33 MW steam unit at Al-Hussein Thermal Power Plant (HTPP), in Jordan is presented. The repowering is achieved by integrating a Parabolic Trough Collector (PTC) system with the Feed-Water Heaters (FWHs) to substitute for steam extractions from the steam turbine. Such integration of a new technology will lead to improve the performance of the existing power plant and reduce its fuel consumption; consequently, the resultant pollutant emissions will be reduced. The paper is organized as follows: the next section presents the literature review related to the research subject; section 3 describes the adopted methodology in this research; the results and

\* Corresponding author e-mail: jojaber@gmail.com.

discussion are then introduced in section 4; and section 5 presents some concluding remarks.

## 2. Introduction

The early works about hybridization of Rankine cycle with solar thermal energy started in 1975 with Zoschak and Wu studying seven alternatives of absorbing solar energy as direct input to 800 MW fossil-fuelled steam power plant [2]. It was reported that combined evaporation and superheating is the preferred option for hybridization. Gupta and Kaushik [3,4] analyzed exergy characteristics for different components of a proposed conceptual solar thermal power plant and they concluded that heating feed-water using solar energy is more advantageous than using the same solar energy in a stand-alone solar thermal power plant. Hu *et al.* [5] studied the advantages of the Solar Aided Power Generation (SAPG) concept using THERMOSOLV software. They proved that energy and exergy efficiencies of a power station can be improved by using solar energy to replace the extracted steam for heating feed-water. Qin Yan *et al.* [6] studied the overall efficiencies of the SAPG with different solar systems to substitute partially for steam extraction in the regenerative cycle. It was found that solar integration assisted the existing power plant in reducing coal consumption and pollution emissions due to increased net power output. Suresh *et al.* [7] analyzed energy, exergy, economic, and environmental impacts of hybrid solar-coal-fired power plants, in India, by using the Cycle Tempo software. It was shown that there is an instantaneous fuel conservation of about 5-6% with the substitution of turbine bleed streams to the feed-water heaters. Popov [8] modeled three options to repower an existing 130 MW steam power plant with solar heating using THERMOFLEX software. The off-design calculations indicated that the most attractive option, especially for existing power plants, is the replacement of High Pressure (HP) heaters with an adequate solar field to raise boiler feed-water temperature up to the desired approach temperature.

Xiuyan *et al.* [9] proposed using solar steam as an auxiliary thermal source of a 600 MW coal-fired supercritical unit, by integrating solar system with the de-aerator. Yang *et al.* [10] demonstrated SAPG through a case study of a 200 MW coal-fired power plant, and discussed different replacement schemes. Reddy *et al.* [11] carried out a comparative energetic and exergetic analysis of a solar aided coal-fired supercritical thermal power plant. It was reported that there was an instantaneous increase in power generation capacity up to 20% when substituting turbine bleed streams for all the LP- and HP-FWHs. Yan *et al.* [12] developed a model to evaluate SAPG, studying energy and economic benefits if integrating solar system to preheat feed-water in the range from 90°C to 260°C. Their results indicated that the benefits of SAPG vary for different steam extraction positions and power plant configuration: in general, the larger the power plant, the higher the benefit for the same level of integrated solar power.

There are various options for integrating CSP technologies with a steam cycle. In the current investigation, the boiler and feed-water heaters are the only sources of thermal energy in the cycle; however, all steam is generated in the boiler. Integrating solar system with the boiler requires a high-temperature solar technology like solar tower or advanced parabolic trough collectors, in addition to controls complexity. But the integration with feed-water heaters to replace steam extraction from the steam turbine appears to be a more practical option due to relatively medium temperature required in this case. Benefits of solar-aided power plant, i.e., hybridization or solar repowering, are numerous but the most important are:

- Reduce consumption of fossil fuel(s) and resultant emissions
- Improve cycle efficiency
- Lower capital cost than solar-only plants
- Guarantee full capacity plant operation

In the market, there are four CSP technologies available and used; these are (i) Stirling-dish engine, (ii) Central Receiver System (CRS), (iii) Parabolic Trough Collectors (PTC) and (iv) Linear Fresnel reflectors (LFR). In the present study the PTC has been considered as preferred technology for producing the required heat for FWHs due to the followings:

1. Proven technology in commercial projects
2. Low cost
3. Low relative area required ( $\text{m}^2/\text{kW}$ )

In future research, LFR system will be considered and final results should be compared with findings of the study in hand. PTC could work with Heat Transfer Fluid (HTF) such as thermal oils where oil transfers thermal energy to the water to produce saturated or superheated steam, or water can be used as a heat transfer fluid with direct steam flashing (below 100 bar steam). As the objective here is simply to heat FWHs with steam outlet conditions below 100 bar, then a Direct Steam Generation (DSG) option, without any type of thermal storage, was considered due to the following advantages [13]:

1. No need for additional heat exchangers
2. Reduced size of the solar field
3. Low investment cost as well as O&M costs
4. No danger of pollution or fire

The present investigation is the 1<sup>st</sup> attempt in Jordan to study the integration of CSP with an existing thermal power plant. For this purpose, researchers have developed a tailor-made simulation of an old steam unit of 33 MW<sub>e</sub>, which was installed in the second half of 1970s at HTPP near Zarqa in Jordan, based on principles of thermodynamics and energy conversion. This model was used to evaluate the performance (energy balance, consumption, power output, efficiency, etc.) of this power station. Then a Concentrated Solar Power system (CSP) is introduced to preheat boiler feed-water instead of live-steam extraction from the steam turbine and compared to the base case scenario. But it should be remembered that it is not the aim of this research work to redesign the steam cycle or its components, rather providing a techno-economic and environmental assessment of such hybrid systems.

### 3. Methodology

The HTPP is an old power plant, located nearby Zarqa, approximately 30 km northeast of the Capital Amman. The plant site is situated at 560 m above sea level. It consists of seven generating units and split into two groups: old 3×33 MW and new 4×66 MW steam units. The nominal design efficiency of old 33 MW units was 33%. Such low efficiency is due to the fact that air-cooled condensers are used because of lack of fresh water supplies. The plant was connected to the grid and came on commercial operation in 1977, and after 38 years of operation the real efficiency dropped to 26%, as reported by the Central Power Generation Company [14]. In this study, one of these 33 MW units has been selected and analyzed. The employed thermal cycle is a standard regenerative Rankine cycle, in which the boiler feed-water heating system consists of four closed and single open feedwater heaters. Fig.1 shows the original heat and mass balance and flow diagram for this unit, with heavy fuel oil being the prime fuel. The blocks in red dashed-line are main components: fuel-fired boiler, multi-stage steam turbine, condenser, water pumps, feed-water heaters and other accessories.

The design point energy and mass balances are presented for each component; which represent the base case in the current study, i.e., before integrating the proposed CSP system. Based on this diagram, a detailed thermodynamic analysis was carried using a tailor-made simulation program, which enabled calculating all properties such as temperature, pressure, enthalpy, and flow rate, etc., at each point of the cycle and for each

component. Followed by discussing different scenarios for integrating the selected CSP technology with the existing cycle, the simulation of CSP technology is conducted by using the System Advisor Model (SAM) software, which is developed by the National Renewable Energy Laboratory (NREL) of USA, to study and analyze the performance of the CSP system as part of the hybrid Solar-Rankine cycle.

SAM software, which is used to evaluate the CSP system, requires a resource data file describing the solar energy source and weather conditions on site such as hourly values of solar radiation and weather data. These include but not limited to solar and weather parameters (GHI, DNI and DHI) and dry/wet ambient temperatures, relative humidity, atmospheric pressure, wind speed, direction and albedo, in addition to latitude, longitude and elevation as summarized in Table 1. The reference solar parameter, DNI, employed in this study is shown in Fig. 2. The basic assumptions used in this study are (i) average DNI 950 W/m<sup>2</sup>, (ii) ambient temperature 20°C, and (iii) wind velocity 10 m/s.

The input parameters, for simulation with SAM, for all proposed options are summarized in Table 2, each option is taken as a separate case in order to calculate the optimal area required for the PTC solar field. This enabled the determination of best and optimal performance with feasible initial/capital costs. But it should be remembered here that the land area depends on different factors such as the distance between the PTC rows and aperture area. The latter depends on required thermal capacity, DNI, ambient temperature, wind velocity and Solar Multiple (SM), etc.

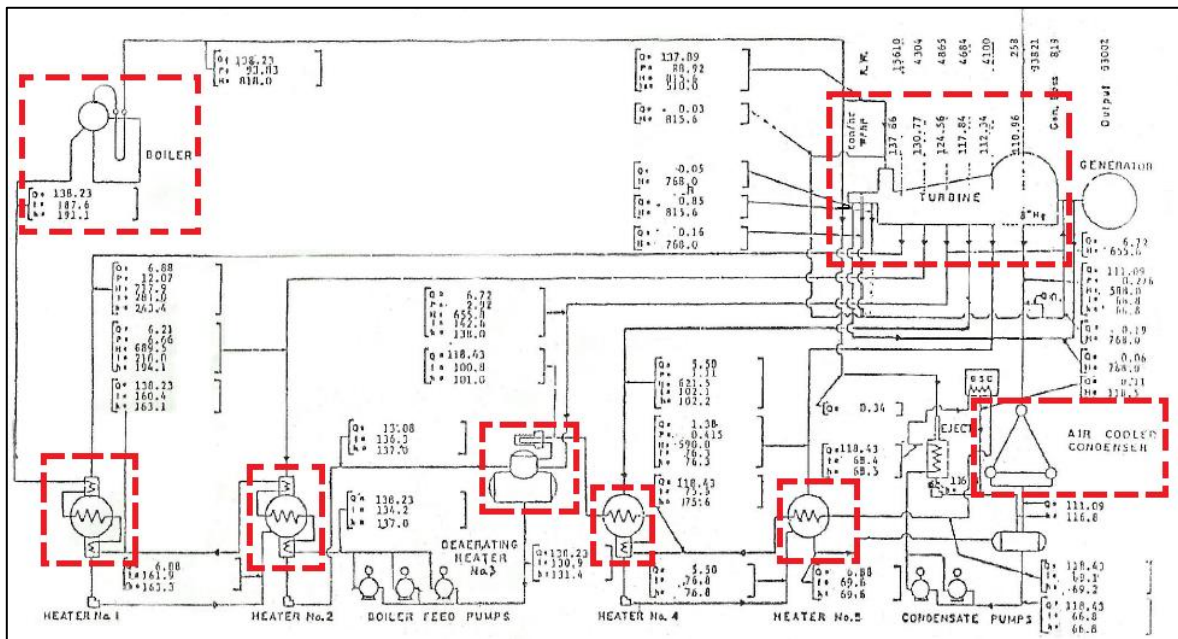


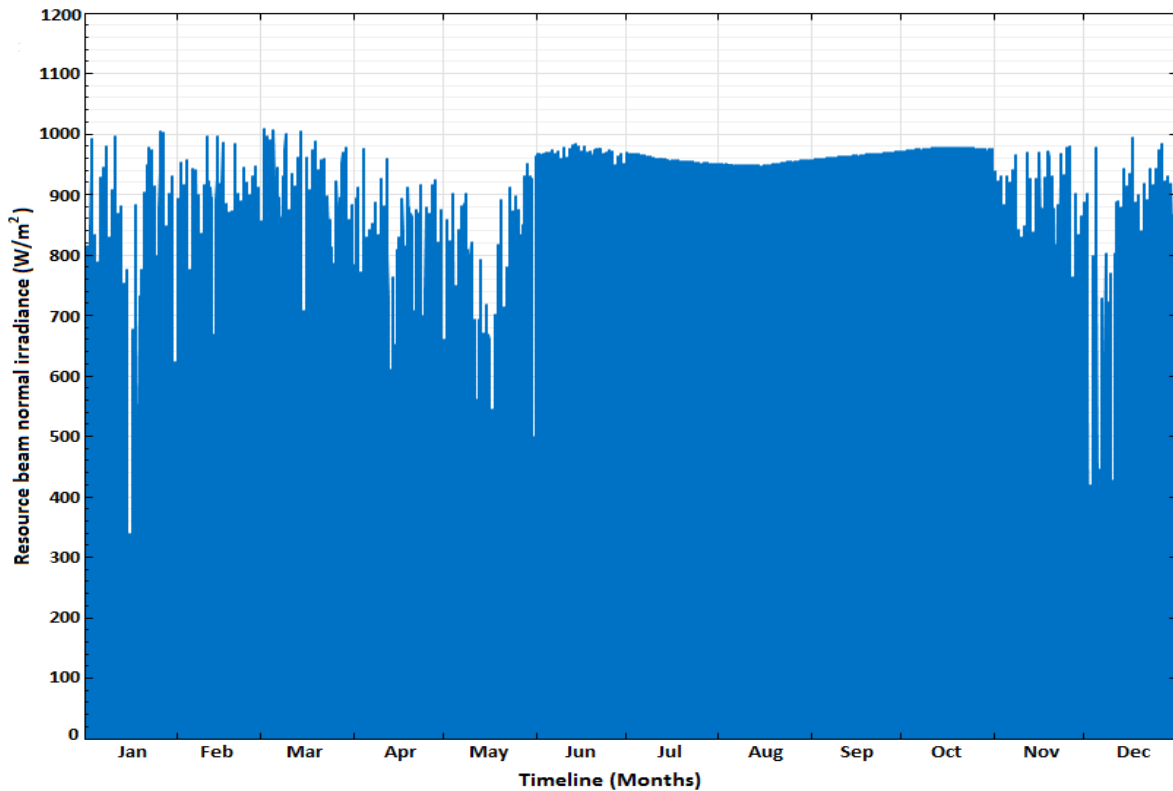
Figure 1. Heat balance and flow diagram for the 33 MW steam-unit

**Table 1.** Solar and weather data for plant location

State, City	Zarqa, Al-Hashemyyeh
Country	Jordan
Time Zone	GMT 2
Elevation (m)	560
Data Source	TMY3
Latitude (°)	32.07 N
Longitude (°)	36.07 E
GHI (kWh/m <sup>2</sup> /day)	5.13
DNI (kWh/m <sup>2</sup> /day)	6.39
DHI (kWh/m <sup>2</sup> /day)	1.04
Avg. Temperature (°C)	18.6
Avg. Wind Speed (m/s)	10.4

**Table 2.** Parameters for different FWHs replacement options

Replacement Option	Mass Flow Rate (ton/h)	Thermal Energy Rate (kcal/h)	Thermal Energy (MW)	Water/Steam Inlet Temp. (°C)	Water/Steam Outlet Temp. (°C)	Water/Steam Inlet Pressure (bar)		
FWH #1	6.88	4,939,152	5.74	281.0	161.9	12.07		
FWH #1+2	#1	6.88	9,220,947	10.72	281.0	12.07		
	#2	6.21			13.09	218.0	136.3	6.66
FWH #1+2+3	#1	6.88	13,627,923	15.85	281.0	12.07		
	#2	6.21			19.81	218.0	136.3	6.66
	#3	6.72			19.81	142.6	130.9	2.92
FWH #1+2+3+4	#1	6.88	17,046,173	19.82	281.0	12.07		
	#2	6.21			25.31	218.0	136.3	6.66
	#3	6.72			25.31	142.6	130.9	2.92
	#4	5.50			25.31	102.1	76.8	1.11
FWH #1+2+3+5	#1	6.88	14,442,123	16.79	281.0	12.07		
	#2	6.21			21.19	218.0	136.3	6.66
	#3	6.72			21.19	142.6	130.9	2.92
	#5	1.38			21.19	76.3	69.6	0.42
FWH #4+5	#4	5.50	4,232,450	4.92	102.1	1.11		
	#5	1.38			6.88	76.3	69.6	0.42
FWH #5	1.38	814,200	0.95	76.3	69.6	0.42		
All FWHs	26.69	17,860,373	20.77	281.0	69.6	0.42 - 12.07		

**Figure 2.** Resource beam normal irradiance (DNI) in Zarqa around the year

In the present study, integration of CSP system with feed-water heaters is considered and eight different options of replacing feed-water heaters are presented and discussed, as follows:

1. Feedwater heater No.1 (one high pressure FWH).
2. Feedwater heaters No.1 and No.2 (two high pressure FWHs).
3. Feedwater heaters No.1 to No. 3 (two high pressure FWHs and one open FWH).
4. Feedwater heaters No.1 to No. 4 (two high pressure FWHs, one open FWH and one low pressure FWH).
5. Feedwater heaters No.3 to No. 5 (one open FWH and two low pressure FWHs).
6. Feedwater heaters No.4 and No.5 (two low pressure FWHs).
7. Feedwater heater No.5 (one low pressure FWH).
8. All feedwater heaters (five FWHs).

In all of these scenarios, there will be no water/steam mixing between the solar system and the steam unit due to using a closed-loops system which should provide FWHs with adequate steam/water flow rate at the specified conditions. The obtained results are presented and discussed in the following section, with the basic assumption applying for all these scenarios is that the plant running at full load in order to simplify calculations. Bearing in mind that the aim of this research is to demonstrate the impacts of integrating the proposed CSP system with an existing steam unit, and not to redesign the power plant or its components.

## 4. Results and Discussion

### 4.1. Energy and Mass Balance

In this study, all engineering calculations for supplying

the required heat as steam, generated by the PTC to the FWH No.1, was taken as a sample for the rest of FWHs (see Fig. 1). Such solar add-on would eliminate steam extraction from the steam turbine, consequently more steam mass flow expand in later stages of the turbine. Finally, this will produce more network output to the generator.

The effect of first replacement (i.e., FWH No.1) on the T-s diagram is shown in Fig. 3. It is clear that steam at point 1 is no longer extracted from the turbine, since the required heat load is supplied by the PTC system. Based on thermodynamic principles and analysis, after establishing mass and energy balances, the predicted effect on different cycle parameters ( $\dot{Q}_{in@Boiler}$ ,  $\dot{W}_{Turbine}$ ,  $\dot{W}_{Pumps}$ ,  $\dot{Q}_{out@condenser}$ , etc.) is determined and the final efficiency ( $\eta$ ) of the steam cycle can be estimated.

This replacement of source of steam, to FWH No.1, showed positive effect on turbine's output, which is reflected on the cycle efficiency: increased cycle's efficiency by about 1.04%. Similar procedure was followed for the rest of proposed options (see Figs. 4 & 5). Close look at these two figures clearly confirms that substitution for FWH No. 5 would result in least improvement on the cycle due to the fact that needed steam here is at low pressure and mass-flow rate, which has insignificant influence on the work produced by the turbine. While supplying all FWHs with steam generated by the PTC system would increase the final efficiency by approximately 3%. Main performance indicators of the cycle for all studied options are summarized in Table 3. It is clear that replacing all FWHs, or high (1&2) and low (3&4) pressure, is the best option. Since the steam will continue expansion in the turbine resulting in more output instead of being extracted for feedwater heaters.

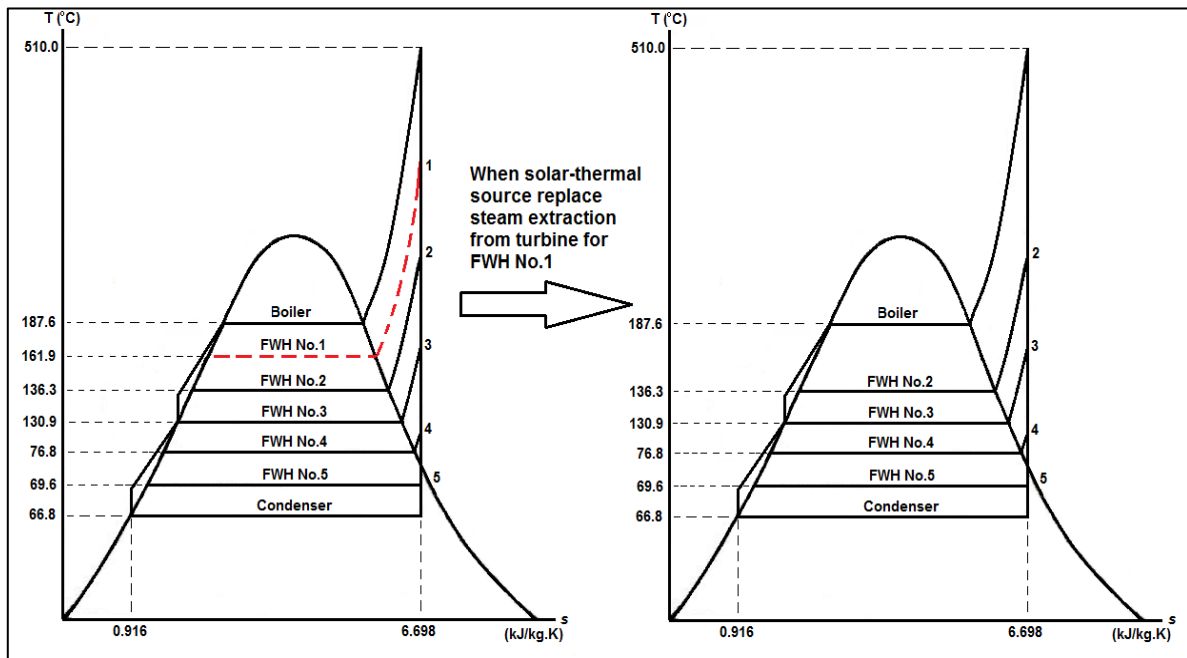


Figure 3. Replacement of FWH No.1 on T-s diagram

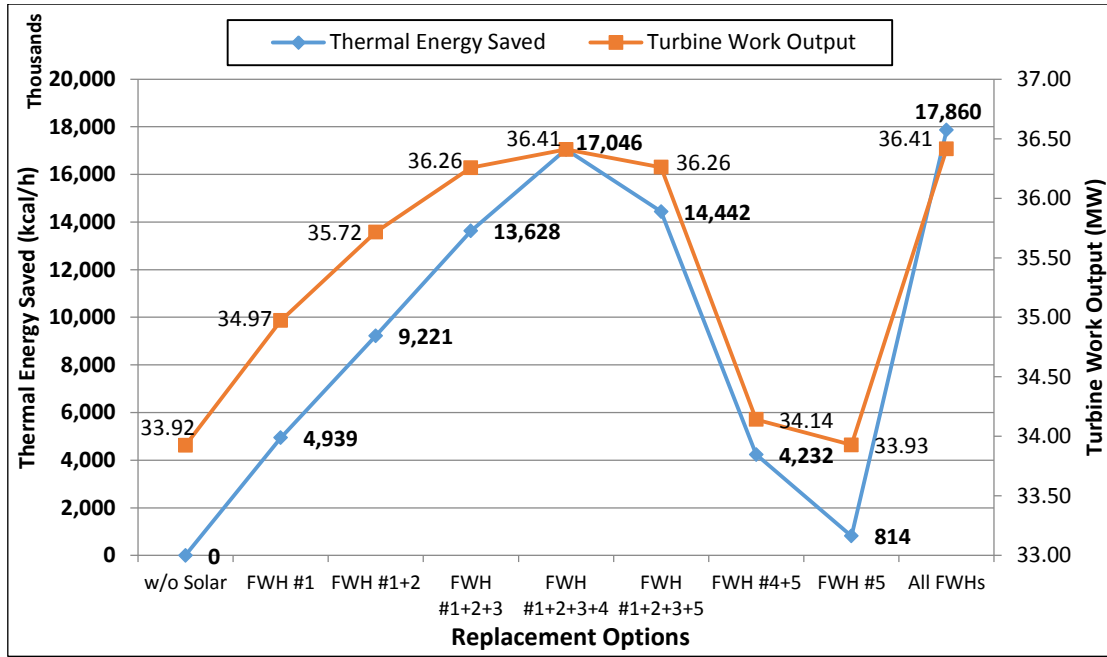


Figure 4: Saved thermal energy and turbine work output for various replacement options of FWHs

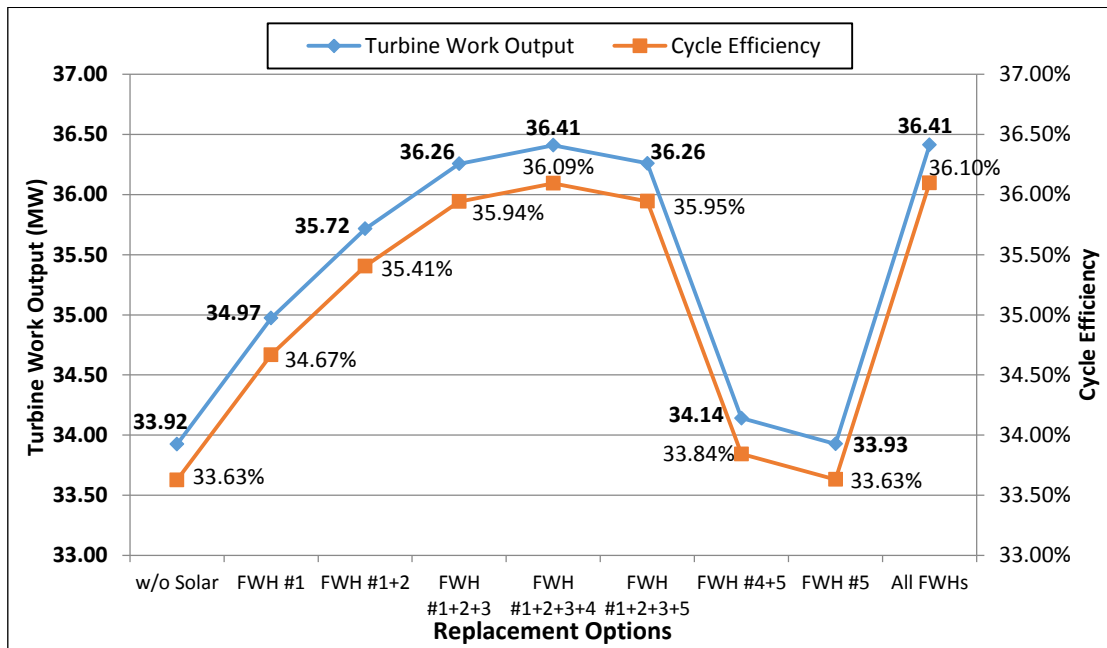


Figure 5: Steam turbine work output and cycle efficiency for various replacement options of FWHs

Table 3: Main performance indicators for all studied options

Replacement Option	Saved Steam (ton/h)	FWH(s) Thermal Energy (kcal/h)	$\dot{W}_{Turbine}$ (MW)	$\dot{Q}_{Condenser}$ (MW)	$\dot{W}_{Cond.Pump}$ (kcal/h)	$\eta$ (%)
Base Case	0	---	33.92	67.21	$2.6 \times 10^{-3}$	33.63%
FWH #1	6.88	4,939,152	34.97	71.38	$2.7 \times 10^{-3}$	34.67%
FWH #1+2	13.09	9,220,947	35.72	75.14	$2.9 \times 10^{-3}$	35.41%
FWH #1+2+3	19.81	13,627,923	36.26	79.22	$3.0 \times 10^{-3}$	35.94%
FWH #1+2+3+4	25.31	17,046,173	36.41	82.55	$3.0 \times 10^{-3}$	36.09%
FWH #1+2+3+5	21.19	14,442,123	36.26	80.05	$3.0 \times 10^{-3}$	35.95%
FWH #4+5	6.88	4,232,450	34.14	71.38	$2.6 \times 10^{-3}$	33.84%
FWH #5	1.38	814,200	33.93	68.05	$2.6 \times 10^{-3}$	33.63%
All FWHs	26.69	17,860,373	36.41	83.39	$3.0 \times 10^{-3}$	36.10%

4.2. Required Solar Field

Optimization of required solar field aperture area and performance prediction of the proposed PTC system was achieved by employing SAM, as a simulation tool, as illustrated previously. Fig. 6 shows the schematic-flow diagram of the steam-unit after integrating the PTC system with FWH No.1 and simulation results are summarized in Table 4. The minimum value of solar multiple is assumed to be 1.5 to ensure that the system will work all over the year at its rated capacity. The field thermal energy produced by the PTC system over the year is shown in Fig. 7.

Table 4: Simulation data of PTC for FWH No.1

Replacement Option	Input Parameters			Output of PTC		
	Solar Multiple (SM)	Required Thermal Power Output (MW <sub>th</sub> )	Steam Output/Input Temperatures (°C)	Solar Field Aperture (m <sup>2</sup> )	Active Hours <sup>1</sup> (hour)	Out of Service Days <sup>2</sup>
FWH#1	1.50	5.74	300/160	13,160	2,043	91

1: Active hours (out of 8,760 hours)

2: Out of service days (out of 365 days)

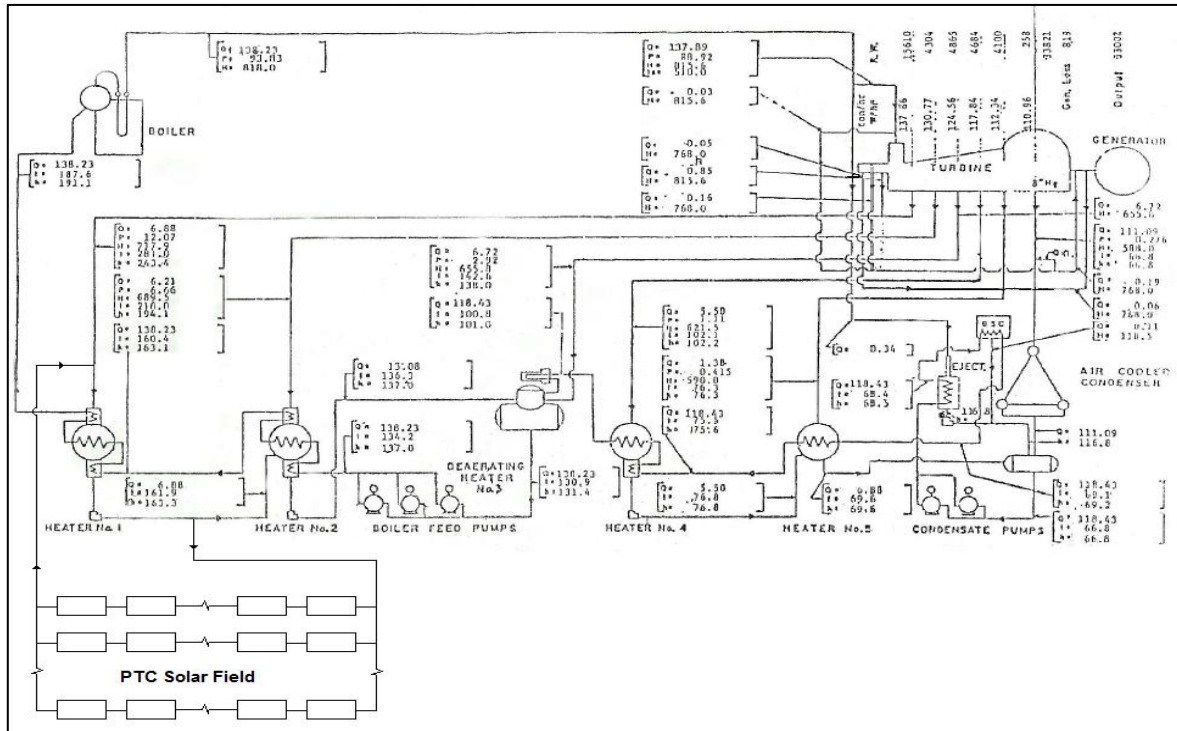


Figure 6: Schematic diagram with PTC system to supply FWH No.1

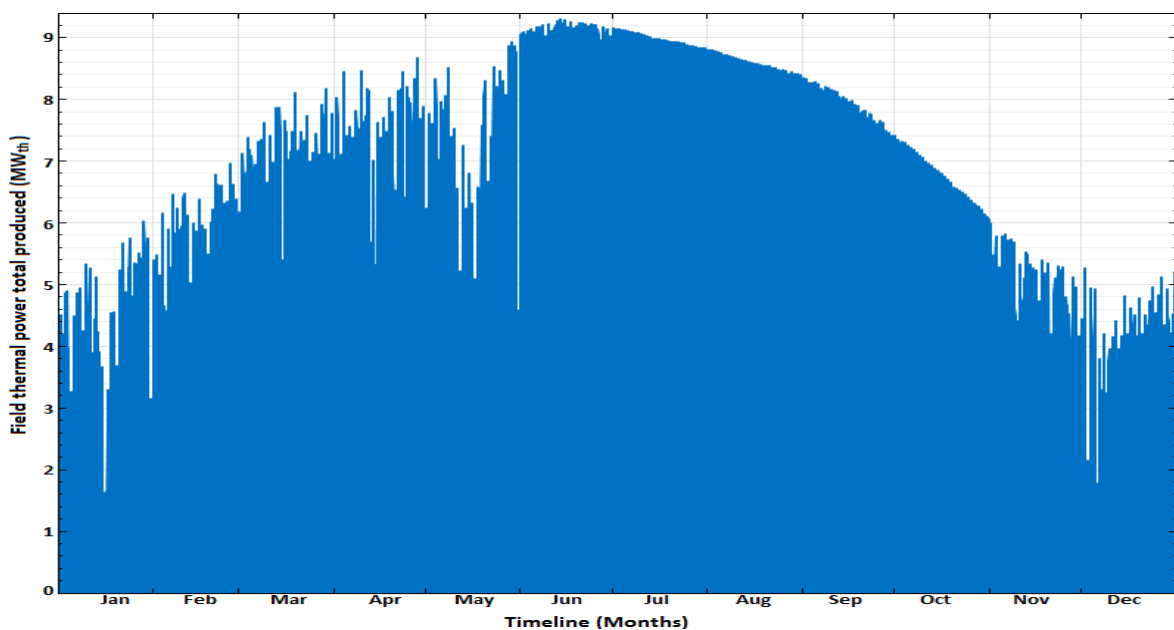


Figure 7. Field thermal power produced for FWH No.1 with SM = 1.5 over a year

In order to meet the minimum required thermal energy demand all around working days, i.e. during winter season and cloudy days, and to increase active hours of the proposed PTC system, the SM factor should be enlarged to satisfy the demand. In this study, to calculate the optimal solar field aperture area, different trials were carried out, for FWH No. 1, by changing the SM value between 1.50 and 2.75 with a step of 0.25. Same procedure applied for all FWHs replacement options and sample of results of FWH No.1 option are summarized in Table 5.

**Table 5:** Simulation results of FWH No.1 with variant SM values

Input Parameters			Output of PTC		
Solar Multiple (SM)	Required Thermal Power Output ( $MW_{th}$ )	Steam Output/Input Temperatures ( $^{\circ}C$ )	Solar Field Aperture ( $m^2$ )	Active Hours <sup>1</sup> (hour)	Out of Service <sup>2</sup> (Days)
1.50	5.74	300/160	13,160	2,043	91
1.75			15,275	2,426	55
2.00			17,390	2,703	26
2.25			19,505	2,911	8
2.50			21,855	3,080	7
2.75			23,970	3,168	3

1: Active hours (out of 8,760 hours)

2: Out of service days (out of 365 days)

It is clear from the tabulated figures in Table 5 that solar field aperture area for any replacement option is directly proportional to solar multiple as well as PTC system's active hours. Doubling SM factor would lead to a sharp drop in the out of service days, i.e., from 91 to 3, but the aperture area almost doubled which will increase the required capital investment and O&M costs. This direct proportional relationship between SM value and aperture area is shown in Fig. 8, for all replacement options.

Configuration of PTC system and number of collectors in each of preheating, evaporation and superheating sections of the solar field are not part of this work. Only

models of each collector and receiver are mentioned here. So a commercially available system "SCHOTT PTR 70" is selected as receiver and "Luz LS-2" as collector. Characteristics of receiver and collector are shown in Table 6 [15] and Table 7 [13].

**Table 6:** Characteristics of "SCHOTT PTR 70" receiver

Absorber steel pipe outer/inner diameter (m)	0.070 / 0.066
Glass envelope outer/inner diameter (m)	0.120 / 0.115
Inner roughness of steel absorber pipes (m)	$4.5 \times 10^{-5}$
Absorber absorption	0.96
Absorber emittance	0.095
Glass envelope transmittance	0.97
Selective coating	Black Cr
Heat losses (W/m)	58.29
Thermal losses (W/m and $W/m^2$ )	77.03 / 15.40
Optical efficiency	0.75

**Table 7:** Characteristics of "Luz LS-2" collector

Solar collector assembly (SCA) length (m)	50
SCA aperture (m)	5
SCA aperture reflective area ( $m^2$ )	235
Distance between SCAs in row (m)	1
Row spacing; center to center (m)	15
Number of SCAs per Row	4
Deploy angle ( $^{\circ}$ )	10
Stow angle ( $^{\circ}$ )	170
Average focal length (m)	1.8
Solar tracking accuracy ( $^{\circ}$ )	0.10
Maximum wind velocity to operate (km/h)	56
Mirror reflectivity	0.935
Aperture angle	80
Geometric accuracy	0.98
Dust on envelope	0.98

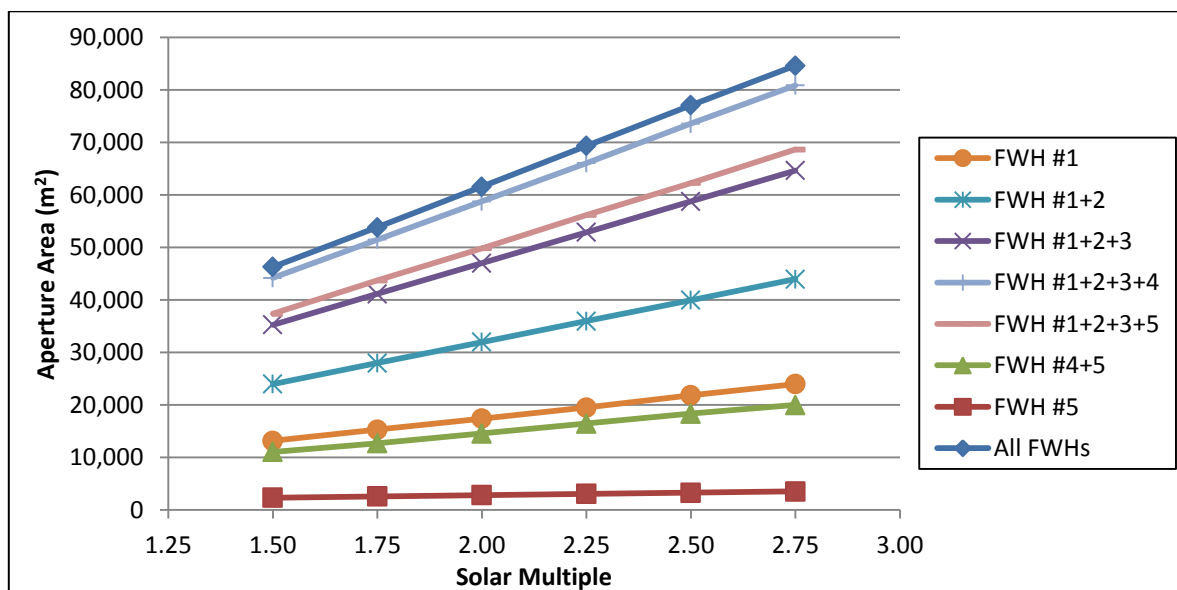


**Figure 8:** Relationship between solar multiple and solar field aperture area

4.3. Economic Analysis

In open literature there is limited information about cost breakdown of CSP systems. In addition to lack of local experience in such new systems from EPC point of view which prevents making reasonable assumptions. The only dependable available sources are the World Bank report, 2011, which included the investment cost of different subsystems of Andasol-1 plant in Spain [16] and the cost model developed by the National Renewable Energy Laboratory (NREL) with assistance from Worley Parsons Group Inc., for use with NREL's System Advisor Model (SAM) [17]. Based on these reports, estimates of capital and running costs factors of the proposed PTC system are summarized in Table 8.

**Table 8:** Estimated capital and annual running cost factors for the proposed PTC system

Parameter	Cost Factor
Direct Capital Cost	
Site Improvement (US\$/m <sup>2</sup> )	10.0
Solar Field (US\$/m <sup>2</sup> )	400.0
HTF System (US\$/m <sup>2</sup> )	5.0
Contingency (% of total direct cost)	3%
Indirect Capital Cost	
Engineering, procurement and construction (% of total direct cost)	10%
Annual Running Cost	
O&M (labor and material) (US\$/kW-year)	12.0

Based on basic assumptions provided in Table 8 and previous calculations, the total capital cost of PTC system needed to replace FWH No.1 (with SM = 1.5 and aperture area of 13,160 m<sup>2</sup>) are assessed as shown in Table 9. This could provide an initial projection of costs related to integrating a CSP system with an existing steam power unit. The share of each of main components of the proposed PTC system in the total capital cost is shown in Fig. 9.

**Table 9:** Total capital cost of PTC for FWH No.1 (SM = 1.5)

Parameter	Cost (US\$)
Direct Capital Cost	
Site Improvement	131,600.0
Solar Field	5,264,000.0
HTF System	65,800.0
Contingency	163,850.0
Indirect Capital Cost	
EPC Contract	562,530.0
Total	6,187,780.0

It is clear that solar field cost is the major one with sharing ratio of 85%, while all other items represent less than 15%. Table 10 summarizes total capital costs and cost per energy unit produced by the new system (US\$/kW<sub>th</sub>) for replacing FWH No.1, with variable SM values as discussed previously. Based on previous calculations and assumptions, the projected simple payback period for this project is not very attractive since it exceeded 11-12 years. But with prevailing low oil prices in the international market, in 2016, the payback period is much longer. In Fig. 10 which illustrates the relation between SM, capital cost and SPBP for FWH No.1 replacement option, it is obvious that the optimal SM values is around 1.75 and estimated SPBP not less than eleven years.

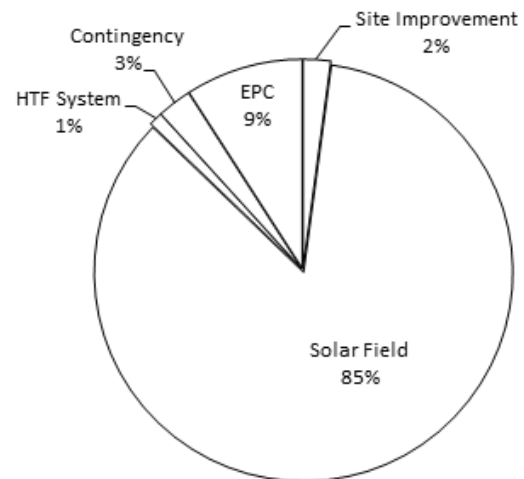


**Figure 9:** Cost share of main components of proposed PTC system to replace FWH No.1

**Table 10:** Cost analysis for replacement FWH No.1 option

SM	Aperture Area (m <sup>2</sup> )	Capital Cost (10 <sup>6</sup> US\$)	Unit Energy Cost (US\$/kW <sub>th</sub> )	Actual Active Hours (hour)	Thermal Energy Saved* (kcal×10 <sup>9</sup> /yr.)	Fuel Saving** (US\$/yr.)	Simple Payback Period (year)
1.50	13,160	6.188	1,077	2,002	11.237	541,046	11.44
1.75	15,275	7.182	1,251	2,377	13.344	642,476	11.18
2.00	17,390	8.177	1,424	2,649	14.868	715,834	11.42
2.25	19,505	9.171	1,597	2,853	16.012	770,918	11.90
2.50	21,855	10.276	1,789	3,018	16.941	815,674	12.60
2.75	23,970	11.271	1,962	3,105	17.425	838,979	13.43

\*Calorific value of HFO (fuel used in 33 MW unit of HTPP) = 10,139 kcal/kg [18]

\*\*HFO price used for power generation based on fuel prices in Jordan considered as US\$ 488.2/ton as in March 2015 [19]

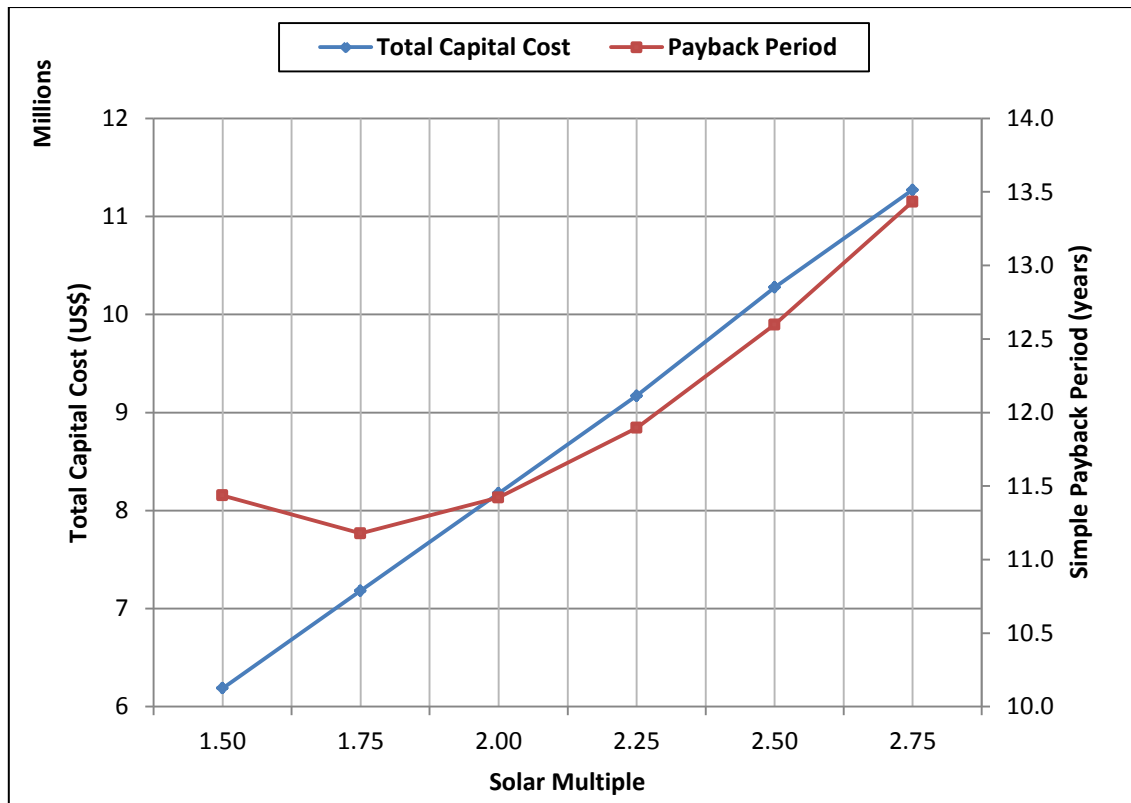


Figure 10: Relation between SM, capital cost and SPBP for FWH No.1 replacement option

Same procedure was applied for all studied options, taking also different SM values. It was found that SPBPs for any replacement option range between 10 and 14 years and the optimum SM between 1.75 and 2.0.

For such long-term project, calculating SPBP is enough to judge on its economics and thus the cash flow over the lifetime of the proposed PTC system should be considered. The long-term investment analysis presented by cash-flow diagram and Net Present Value (NPV) of money were simulated for all cases of FWHs replacement, with various financial parameters as shown in Table 11. The results of such simulation are presented in Figs. 11 and 12 which show annual net cash flow and cumulative cash flow, respectively.

Based on net yearly values cash flow diagram (Fig. 11); NPV at a discount rate of 7% was about +191,503 US\$. While PBP based on cumulative cash flow diagram (Fig. 12) was about 12 years and 6 months. But since the NPV has a positive value, then project is acceptable and may prove to be feasible in the future.

Table 11. Financial parameters and assumptions for investment analysis

Financial Parameter	Value	Notes
Project lifetime (investment period)	20 years	---
Inflation rate	5%	Average value for years (2010-2014) in Jordan [20]
Discount rate	7%	---
Net salvage value	10%	% of total capital cost (Conservative assumption for the value of the project at the end of the lifetime)
Income tax rate	14%	Income tax rate in Jordan due to date 2015 [21]
Insurance	0.3%	% of total capital cost
Debt ratio	70%	% of total capital cost
Loan term	10 years	---
Loan rate	6%	---

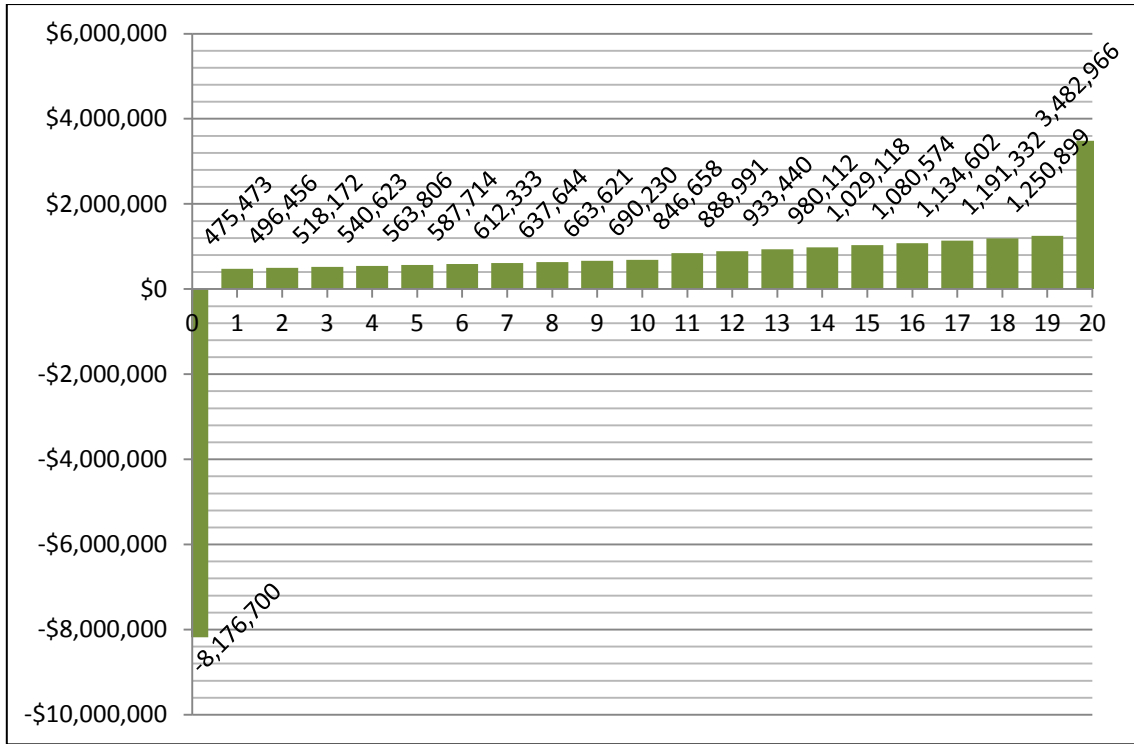


Figure 11: Net values cash flow diagram for FWH No.1 (SM = 2)

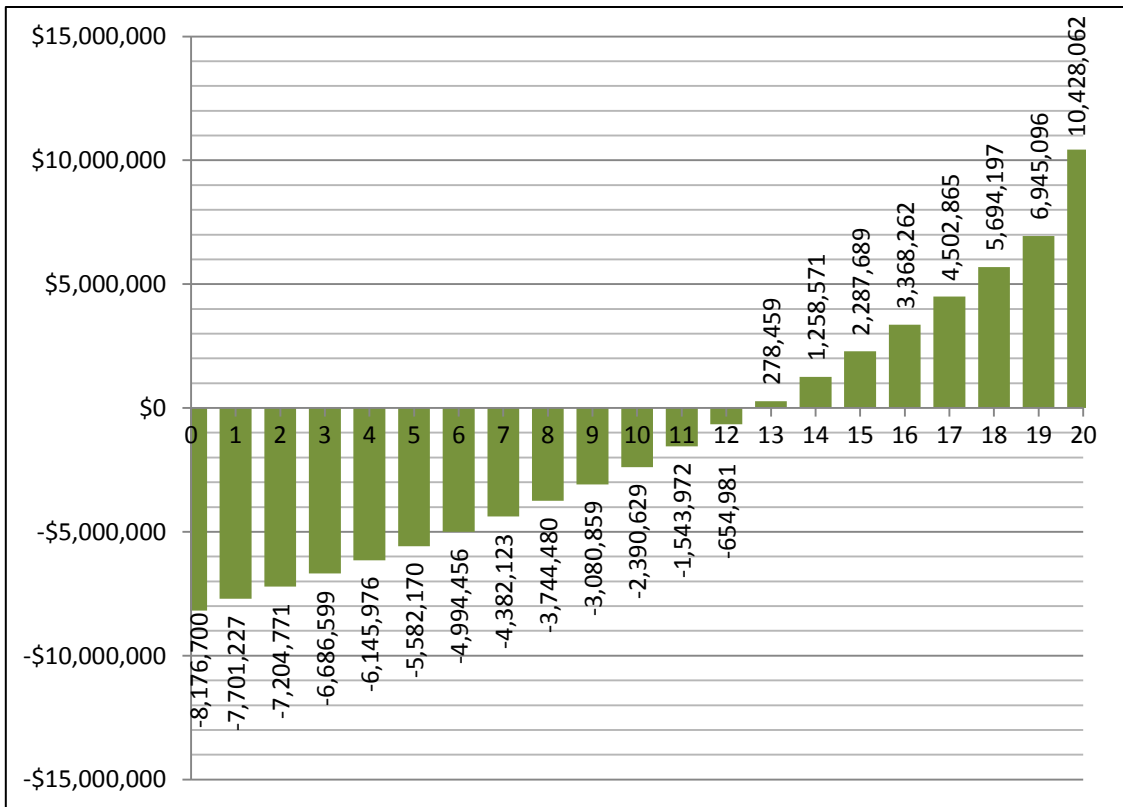


Figure 12: Cumulative cash flow diagram for FWH No.1 (SM = 2)

But, any change in the proposed financial parameters and basic assumptions would have a significant change on NPV and PBP calculations, e.g. increasing debt fraction to 100% of total capital cost will reduce NPV to only +52,011 US\$ and increase PBP by 3 months or more. Since such economic analysis was conducted based on variables and assumptions that are uncertain, then

sensitivity analysis was carried out in order to test the robustness of obtained results and understand better the relationships between most influential input and output variables. As shown in Fig. 13 that most important two variables are capital cost, represented by the cost of required solar field and fuel prices. It is followed by other less important factors, such as construction cost.

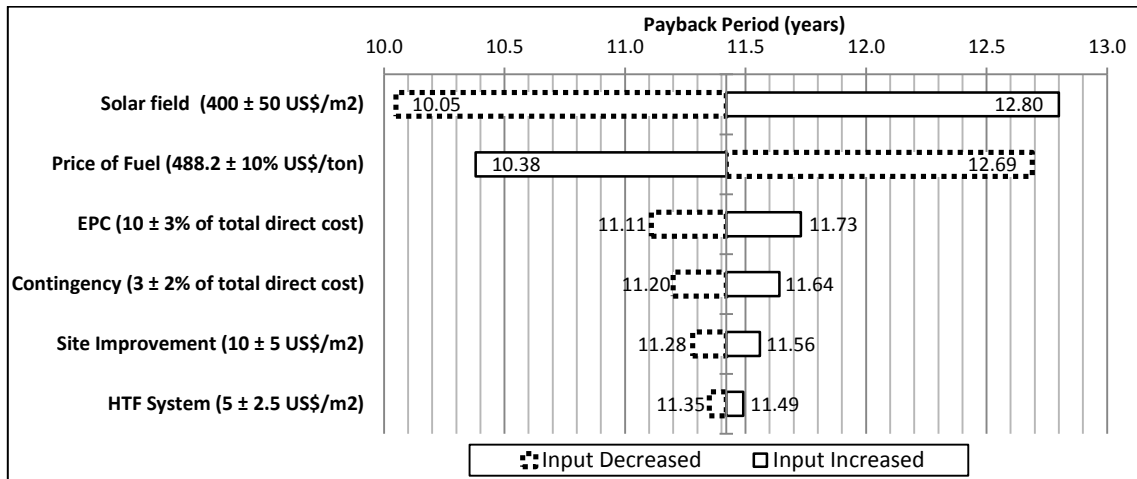


Figure 13: Sensitivity analysis of key parameters and their influence on SPBP

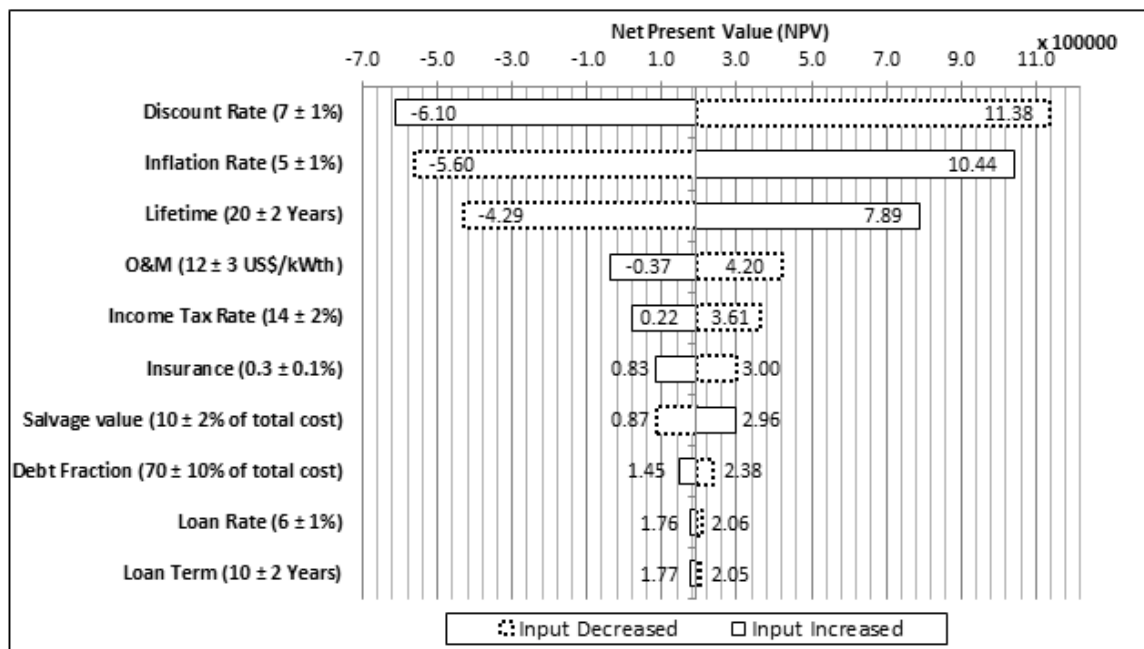


Figure 14: Sensitivity analysis of NPV in relation with employed financial parameters

When looking at the financial parameters, as expected the most important factor on economics of this project is the discount rate (when increased by 1%, the NPV decreased to about -610,000 US\$ and therefore the project is not accepted and invested in such project is not feasible) followed by the local inflation rate and other factors as illustrated in Fig. 14.

#### 4.4. GHG Emissions

As demonstrated earlier that the new CSP integration with existing steam plant saved energy, represented by the amount of HFO needed to generate steam, consequently

there will be net reduction of pollutant gases including GHG emissions. The amount of avoided GHG emissions, represented by CO<sub>2</sub> equivalent was calculated using an emission factor of 77.4 ton CO<sub>2</sub>/TJ [22]. Nevertheless, cost reduction of such project could be achieved through financing from grants and/or CO<sub>2</sub> emissions trading. Based on the European Union Emissions Trading Scheme (EU ETS), each ton of CO<sub>2</sub> avoided could be sold in the international market for approximately 26 US\$ [23]. When such cost is taken into consideration and added to fuel savings, then the SPBP is reduced significantly, by about 15%, as shown in Fig. 15.

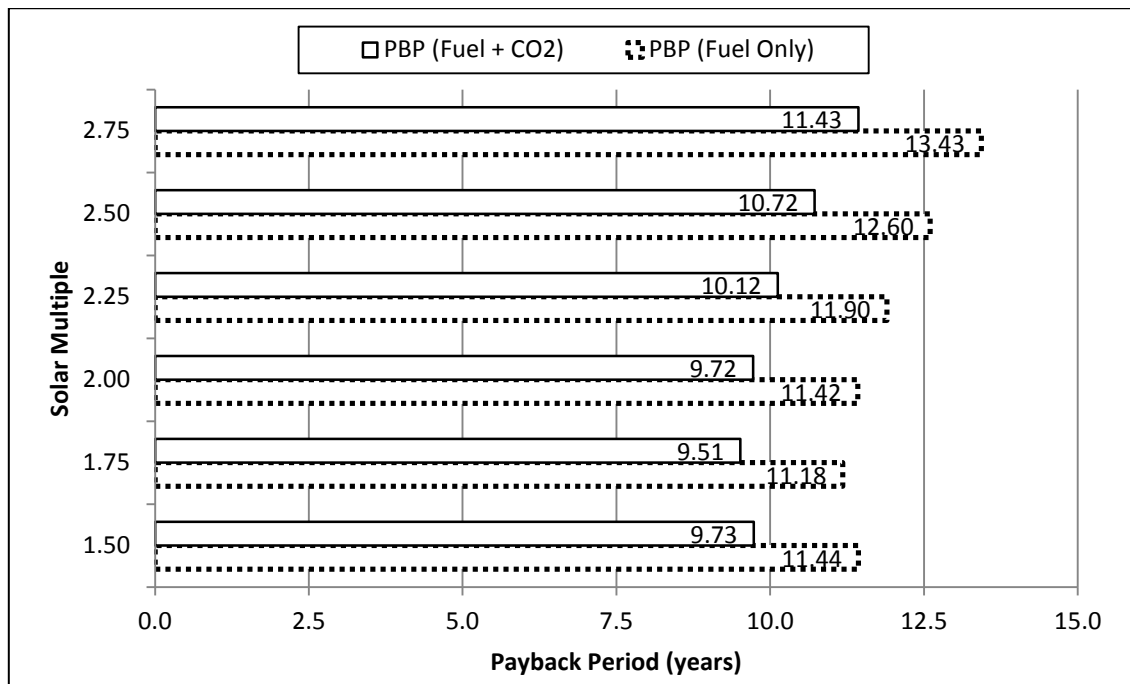


Figure 15: Calculated SPBP for FWH No.1 before and after considering CO<sub>2</sub> emissions

## 5. Conclusion

In the present work, the integration of CSP technology with an old HFO fired steam (standard Rankine cycle) unit of 33 MW is proposed based on a Parabolic Trough Collector system (PTC). This will be used to heat boiler's feed water heaters instead of extracting the required steam from the steam turbine. Technical, economic and environmental analyses were conducted for different scenarios for such integration. Each of the studied scenarios has different thermal capacity; consequently dissimilar solar field aperture areas were required. To conduct such analysis, a trailer-made simulation tool was developed based on basics of thermo-fluids relations. The PTC solar field aperture areas and its performance as well optimal solution were conducted by using the System Advisor Model (SAM) software. The introduced PTC system has increased efficiency by 2.5% due to the net increase (of 7.5%) in turbine's work output and reduced rate of fuel consumption. But this value varied as different FWHs integration scenarios were assumed. The economics of such system under studied circumstances were found not encouraging since the SPBP ranged between 10 and 12 years for different scenarios. The environmental impacts are positive since pollutant emissions were reduced significantly: about 17,500 ton/year of CO<sub>2</sub> could be avoided.

## References

- [1] Jaber JO, Elkarmi F, Alasis E, Kostas A. Employment of renewable energy in Jordan: current status, SWOT and problem analysis, *Renewable & Sustainable Energy Reviews*, Vol. 49, pp. 490-499, 2015.
- [2] Zoschak RJ, Wu SF. Studies of the direct input of solar energy to a fossil-fueled central station steam power plant", *Solar Energy*, Vol. 17, pp. 297-305, 1975.
- [3] Gupta MK, Kaushik SC. Exergetic utilization of solar energy for feed water preheating in a conventional thermal power plant, *International Journal of Energy Research*, Vol. 33, pp. 593-604, 2009.
- [4] Gupta MK, Kaushik SC. Exergy analysis and investigation for various feed water heaters of direct steam generation solar-thermal power plant, *Renewable Energy*, Vol. 35, pp. 1228-1235, 2010.
- [5] Hu E, Yang Y, Nishimura A, Yilmaz F, Kouzani A. Solar thermal aided power generation, *Applied Energy*, Vol. 87, pp. 2881-2885, 2010.
- [6] Qin Yan YY, Nishimura Akira, Kouzani Abbas, Eric Hu. Multi-point and multi-level solar integration into a conventional coal-fired power plant, *Energy Fuels*, Vol. 24, pp. 3733-3738, 2010.
- [7] Suresh MVJJ, Reddy KS, Kolar AK. 4-E (energy, exergy, environment, and economic) analysis of solar thermal aided coal-fired power plants, *Energy for Sustainable Development*, Vol. 14, pp. 267-279, 2010.
- [8] Popov D. An option for solar thermal repowering of fossil fuel fired power plants, *Solar Energy*, Vol. 85, pp. 344-349, 2011.
- [9] Xiuyan W, Mengjiao W, Xiyuan G. Thermal performance analysis of solar steam aided coal-fired power generation, *Materials for Renewable Energy & Environment (ICMREE)*, International Conference, pp. 209-212, 2011.
- [10] Yang Y, Yan Q, Zhai R, Kouzani A, Hu E. An efficient way to use medium or low temperature solar heat for power generation-integration into conventional power plant, *Applied Thermal Engineering*, Vol. 31, pp. 157-162, 2011.
- [11] Reddy V, Kaushik S, Tyagi S. Exergetic analysis of solar concentrator aided coal fired super critical thermal power plant (SACSCTPT)", *Clean Technologies and Environmental Policy*, pp. 1-13, 2012.

- [12] Yan Q, Hu E, Yang Y, Zhai R. Evaluation of solar aided thermal power generation with various power plants, International Journal of Energy Research, Vol. 35, pp. 909-922, 2011.
- [13] Romero-Alvarez M, Zarza E. Concentrated solar thermal power in "Energy Conversion" edited by Goswami D & Kreith F, 1<sup>st</sup> edition, CRC Press, USA, pp. 38, 2008.
- [14] Anon, Central Electricity Generation Company, Annual Report 2014, Amman, Jordan.
- [15] Official website of "SCHOTT PTR<sup>®</sup>70" receiver: [http://www.schott.com/csp/english/download/schott\\_ptr70\\_4th\\_generation\\_datasheet.pdf](http://www.schott.com/csp/english/download/schott_ptr70_4th_generation_datasheet.pdf)
- [16] Ernst & Young Global Limited Co., (France), Goswami Institute for Solar Energy Systems (ISE) and Fraunhofer Institute for Systems and Innovation Research (ISI), Middle East and North Africa Region assessment of the local manufacturing potential for concentrated solar power (CSP) projects, Energy Sector Management Assistance Program (ESMAP), The World Bank, Washington, DC, USA, 2011.
- [17] Turchi C. Parabolic trough reference plant for cost modeling with the System Advisor Model (SAM), Technical Report No. NREL/TP-550-47605 by NREL, Department of Energy, USA, 2010.
- [18] Average calorific value of petroleum products, internal report, personal contact with Laboratories Dept., Jordan Petroleum Refinery Co. Ltd., Jordan, November 2013.
- [19] Fuel prices in Jordan, March 2015, Al-Manaseer Oil and Gas Co., Amman, Jordan [<http://www.mgc-gas.com/fuel-prices/>].
- [20] Inflation rate: <http://www.tradingeconomics.com/jordan/inflation-cpi>
- [21] Income tax in Jordan, 2015 <http://www.tradingeconomics.com/jordan/personal-income-tax-rate>
- [22] CO<sub>2</sub> emission factor for stationary combustion in the energy industries by Darío R. Gómez and John D. Watterson, Chapter 2: Stationary combustion from 2006 IPCC (International Panel on Climate Change) Guidelines for National Greenhouse Gas Inventories, Switzerland.
- [23] Fact sheet: Carbon pricing around the world: <http://www.eesi.org/papers/view/fact-sheet-carbon-pricing-around-the-world?fact-sheet-carbon-pricing-around-the-world-17-oct-2012>

# Computational Fluid Dynamics Simulation of Plate Fin and Circular Pin Fin Heat Sinks

Mohammad Saraireh \*

Mechanical Engineering Department, Assistant Professor, Mutah University, Mutah 61710, Karak, Jordan

Received 4 Desember 2015

Accepted 22 May 2016

## Abstract

In the present paper, the three-dimensional Computational Fluid Dynamics (CFD) simulation of heat transfer and fluid flow in two types of heat sinks are presented. The plate fin and circular pin fin heat sinks are simulated for different air velocity inlet. Thermal and hydraulic performances of plate fin and circular pin fin heat sinks are obtained. Numerical predictions of thermal resistance and pressure drop in the heat sinks are compared with experimental results from the literature and an excellent agreement is found. The results also show that the circular pin fin heat sink has better performance than the plate fin heat sink. For the plate fin heat sink, the thermal resistance varied from 2.92 oC/W to 0.99 oC/W, whereas the pin fin heat sink varied from 2.69 oC/W to 0.89 oC/W.

© 2016 Jordan Journal of Mechanical and Industrial Engineering. All rights reserved

**Keywords:** thermal resistance, pressure drop, heat sink.

## Nomenclatures

$C_p$	specific heat ( $J kg^{-1} K^{-1}$ )
$E$	energy ( $J$ )
$G_b$	generation of turbulence kinetic energy due to buoyancy
$G_k$	generation of turbulence kinetic energy due to mean velocity gradients
$h$	sensible enthalpy ( $J kg^{-1}$ )
$k$	thermal conductivity ( $W m^{-1} K^{-1}$ )
$k$	turbulence energy ( $m^2 s^{-2}$ )
$P_{in}$	inlet pressure ( $Pa$ )
$P_{out}$	outlet pressure ( $Pa$ )
$Q$	heat dissipation rate ( $W$ )
$R_{th}$	thermal resistance ( $^{\circ}C/W$ )
$S_k, S_{\varepsilon}$	source terms in Equations 8 and 9, respectively
$T$	temperature ( $^{\circ}C$ )
$u, v, w$	velocity components ( $m s^{-1}$ )
$V$	velocity ( $m s^{-1}$ )

## Greek symbols

$\sigma_k, \sigma_{\varepsilon}$	turbulent Prandtl numbers for $k$ and $\varepsilon$ , respectively
$\varepsilon$	dissipation in Equations 8 and 9 ( $m^2 s^{-3}$ )
$\mu$	dynamic viscosity ( $kg m^{-1} s^{-1}$ )
$\mu_t$	turbulent viscosity ( $kg m^{-1} s^{-1}$ )
$\rho$	density ( $kg m^{-3}$ )
$\tau$	stress tensor ( $N m^{-2}$ )

## 1. Introduction

Air cooled heat sink is the most widely used type of cooling device because of their many advantages, such as easy fabrication, low cost, and easy maintenance. Using heat sinks to transfer thermal energy has received considerable attention from researchers.

Tuckerman and Pease [1] made a micro-channel heat sink which capable of dissipating a heat flux of 790W/cm<sup>2</sup>. Wesberg *et al.* [2] solved numerically a two-dimensional conjugate heat transfer problem which consists of calculation of heat conduction in the solid and convective heat transfer in the fluid. Temperature distributions, heat flux and Nusselt number along a micro-channel heat sink cross-section were obtained. Teertstra *et al.* [3] developed

\* Corresponding author e-mail: m.saraireh@yahoo.com.au.

an analytical model to predict the average heat transfer rate for forced convection plate fin heat sinks for electronics applications. Jonsson and Moshfegh [4] conducted experiments in a wind tunnel with seven types of heat sinks including plate fin, strip fin, and pin fin heat sinks. They developed an empirical correlation for different fin designs and predicted the Nusselt number and the dimensionless pressure drop. Duan and Muzychka [5] presented a simple semi-empirical model for predicting the heat transfer coefficient of plate-fin heat sinks. Yang and Peng [6] presented a numerical computations of the plate-circular pin-fin heat sink and examined the thermal and hydraulic performance of the heat sink. Their results show that the performance of the in-line design is better than the staggered design. Betz and Attinger [7] designed a polycarbonate heat sink consisting of an array of seven parallel microchannels each with a square cross-section of 500  $\mu\text{m}$  wide. They found that the segmented flow increases the Nusselt number of laminar flow by more than 100%.

Mohammed *et al.* [8, 9] presented numerical simulations to compare the zigzag, curvy, and step heat sinks and concluded that the zigzag design has the best thermal performance. For the wavy heat sink the temperature was always lower than that of plate-fin heat sink. Numerical and experimental study for thermal performances of plate fin heat sinks for various fin spacing were investigated by Chen *et al.* [10]. Yang *et al.* [11] investigated numerically the turbulent fluid flow and heat transfer characteristics of air jet impingement onto the rotating and stationary heat sink.

Hatami and Ganji [12] studied the heat transfer of a fin shaped heat sink cooled by Cu- water. Temperature distributions in the solid section and fluid section were obtained numerically by using the least square method. Jeng *et al.* [13] Experimentally discussed the fluid flow and heat transfer characteristic of square pin fin heat sink filled with packed brass beads. Zhai *et al.* [14] conducted simulations to investigate flow and heat transfer performance of de-ionized water flowing through different micro heat sinks with complex structure under a uniform heat flux.

The present article aims at examining the thermal and hydraulic performances of plate fin and circular pin fin heat sinks by implementing CFD simulation. Numerical solutions are obtained for wide velocity ranges and are compared with the experimental data of Jonsson and Moshfegh [4].

## 2. 2. Mathematical Model and Simulation

### 2.1. Geometrical Parameters of Heat Sinks

The plate fin and circular pin fin heat sinks are shown schematically in Figure 1. The geometrical parameters of the models in this paper are based on Jonsson and Moshfegh [4], and shown in Table 1.

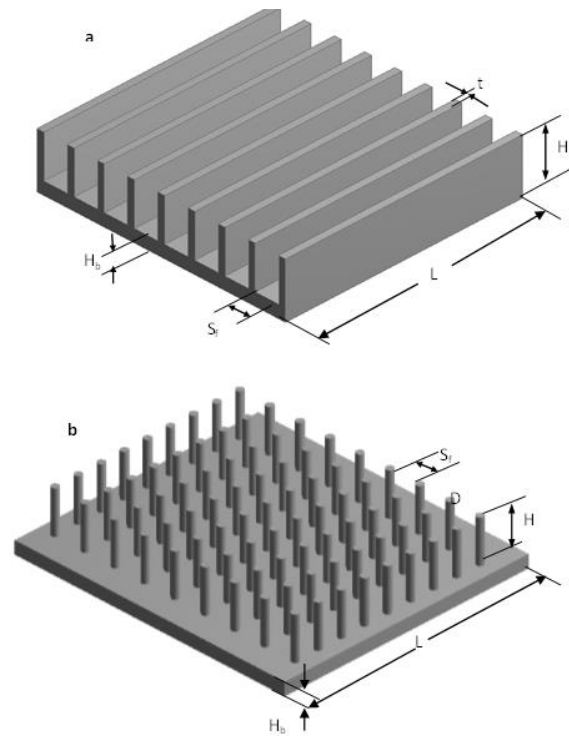


**Figure 1.** Schematic diagrams of heat sinks: (a) plate fin heat sink and (b) circular pin-fin heat sink

**Table 1.** Geometrical parameters of heat sink

Parameters	Dimensions (mm)
Height of the base $H_b$	3
Height of the fin $H$	10
Length of the fin $L$	52.8
Fin spacing $S_f$	5
Fin thickness $t$	1.5
Fin number $N$	9
Diameter of the pin fin $D$	1.5

### 2.2. The Governing Equations

The system is assumed to be a steady state, incompressible and turbulent flow. The mass continuity equation is [15]:

$$\frac{\partial}{\partial x}(\rho u) + \frac{\partial}{\partial y}(\rho v) + \frac{\partial}{\partial z}(\rho w) = 0 \quad (1)$$

where  $\rho$  is the density and  $u, v, w$  are the velocity components.

The following equations represent the conservation of momentum [15]:

$$\frac{\partial}{\partial x}(\rho u u) + \frac{\partial}{\partial y}(\rho u v) + \frac{\partial}{\partial z}(\rho u w) =$$

$$-\frac{\partial P}{\partial x} + \frac{\partial \tau_{xx}}{\partial x} + \frac{\partial \tau_{xy}}{\partial y} + \frac{\partial \tau_{xz}}{\partial z} \quad (2)$$

$$\frac{\partial}{\partial x}(\rho v u) + \frac{\partial}{\partial y}(\rho v v) + \frac{\partial}{\partial z}(\rho v w) =$$

$$-\frac{\partial P}{\partial y} + \frac{\partial \tau_{yx}}{\partial x} + \frac{\partial \tau_{yy}}{\partial y} + \frac{\partial \tau_{yz}}{\partial z} \quad (3)$$

$$\frac{\partial}{\partial x}(\rho w u) + \frac{\partial}{\partial y}(\rho w v) + \frac{\partial}{\partial z}(\rho w w) = -\frac{\partial P}{\partial z} + \frac{\partial \tau_{zx}}{\partial x} + \frac{\partial \tau_{zy}}{\partial y} + \frac{\partial \tau_{zz}}{\partial z} \quad (4)$$

where  $P$  is the static pressure, and  $\tau$  is the stress tensor .

The conservation equation of energy is [15]:

$$\frac{\partial}{\partial x}[u(\rho E)] + \frac{\partial}{\partial y}[v(\rho E)] + \frac{\partial}{\partial z}[w(\rho E)] = \frac{\partial}{\partial x}\left(k \frac{\partial T}{\partial x}\right) + \frac{\partial}{\partial y}\left(k \frac{\partial T}{\partial y}\right) + \frac{\partial}{\partial z}\left(k \frac{\partial T}{\partial z}\right) \quad (5)$$

where  $k \frac{\partial T}{\partial x}$  represent the energy transfer due to conduction. The cases simulated in this paper contain only one species and no source terms are used. In Equation 5:

$$E = h - \frac{P}{\rho} + \frac{v^2}{2} \quad (6)$$

where  $h$  is the sensible enthalpy and can be expressed as:

$$h = \int_{T_{ref}}^T C_p dT \quad (7)$$

where  $T_{ref}$  is 298.73 K.

The governing equations for the realizable turbulent kinetic energy  $k$  and the dissipation rate  $\epsilon$  are [16]

$$\frac{\partial}{\partial x_j}(\rho k u_j) = \frac{\partial}{\partial x_j} \left[ \left( \mu + \frac{\mu_t}{\sigma_k} \right) \frac{\partial k}{\partial x_j} \right] + G_k + G_b - \rho \epsilon - Y_M + S_k \quad (8)$$

And

$$\frac{\partial}{\partial t}(\rho \epsilon) + \frac{\partial}{\partial x_j}(\rho \epsilon u_j) = \frac{\partial}{\partial x_j} \left[ \left( \mu + \frac{\mu_t}{\sigma_\epsilon} \right) \frac{\partial \epsilon}{\partial x_j} \right] + \rho C_1 S_\epsilon - \rho C_2 \frac{\epsilon^2}{k + \sqrt{\nu \epsilon}} + C_{1\epsilon} \frac{\epsilon}{k} C_{3\epsilon} G_b + S_\epsilon \quad (9)$$

In these equations,  $G_k$  represents the generation of turbulent kinetic energy due to the mean velocity gradients.  $G_b$  is the generation of turbulence kinetic energy due to buoyancy.  $Y_M$  represents the contribution of the fluctuating dilatation in compressible turbulence to

the overall dissipation rate.  $C_2$  and  $C_{1\epsilon}$  are constants. The quantities  $\sigma_k$  and  $\sigma_\epsilon$  are the turbulent Prandtl numbers for  $k$  and  $\epsilon$ , respectively.  $S_k$  and  $S_\epsilon$  are user define source terms.

### 2.3. Computational Domain and Boundary Conditions

The geometry of the plate fin and circular pin fin heat sink models and the boundary conditions are illustrated in Figures 2 and 3. Since the fin geometry is periodic in the spanwise direction, a single passage of the heat sink is selected to be the computational domain.

The velocity boundary condition and a constant temperature are set at the inlet. The velocity at the inlet increases from 2 m/s to 12 m/s and the inlet temperature is 294K. At the outlet of the computational domain, a pressure boundary condition is employed. The interface between the solid and the fluid is a no-slip wall with no thermal resistance. A constant heat flux thermal boundary condition is used on the base of heat sink, and the total heat applied on the fin base is 10 W. Adiabatic wall conditions are provided on all the other walls. Properties of the working fluid are the same as those of ambient air at 294 K, and the material of heat sinks is aluminium with thermal conductivity of 202 W/ (m.K).

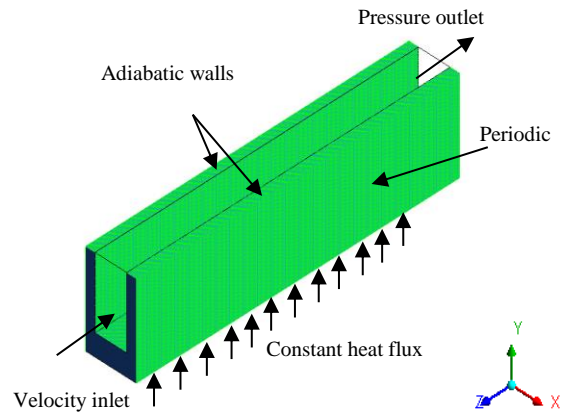


Figure 1. Computational domain and boundary conditions for plate fin heat sink

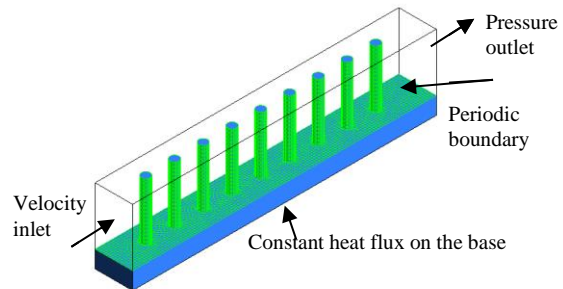


Figure 2. Computational domain and boundary conditions for circular pin fin heat sink

### 2.4. Grid Independence

Different mesh sizes were performed for plate heat sink and pin fin heat sink in order to guarantee the grid independence of the results. Figures 4 and 5 show the

thermal resistance for different grid sizes. According to these figures the results from 700,000 grid size for plate heat sink and 500,000 grid size for pin fin heat sink can be considered to be grid independence.

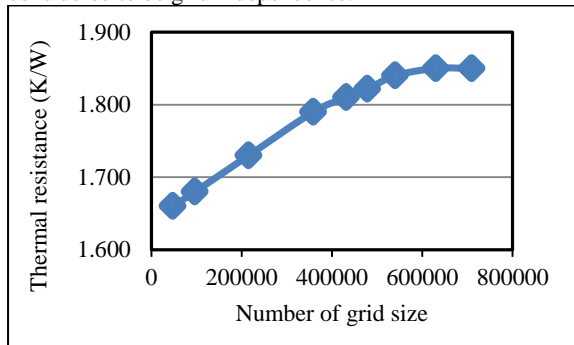


Figure 3. Thermal resistance at different grid sizes for plate fin heat sink

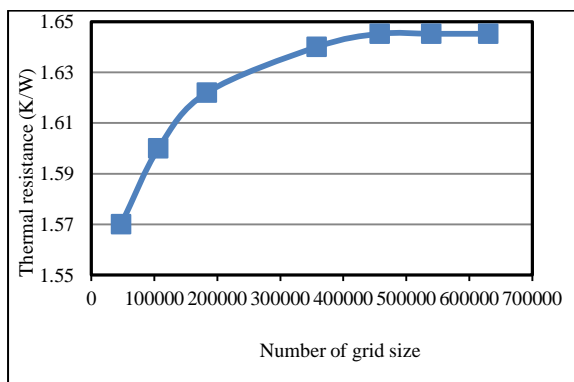


Figure 4. Thermal resistance at different grid sizes for pin fin heat sink

### 3. Results and Discussion

A Computational Fluid Dynamics (CFD) program FLUENT has been used to predict the heat transfer and fluid flow in the two types of heat sinks. In order to verify the present simulation, the thermal resistance and the pressure drop under the conditions  $V_{in} = 2 \text{ m/s}$  to  $12 \text{ m/s}$  and  $Q = 10 \text{ W}$  are compared with the available experimental results of literature [4]. Figures 6 to 9 show a comparison of the experimental data and numerical predictions for both the thermal resistance and the pressure drop of the plate fin and circular pin fin heat sinks.

The thermal resistance of the heat sink is calculated by:

$$R_{th} = \frac{\Delta T}{Q} \tag{10}$$

where  $\Delta T$  is the temperature difference between the temperature on the fin base and the ambient air temperature, and  $Q$  is heat dissipation power applied on the fin base.

The pressure drop ( $\Delta P$ ) from the inlet to the outlet of the flow passage, which reflects the hydraulic performance of the heat sink, is calculated by:

$$\Delta P = P_{in} - P_{out} \tag{11}$$

Figures 6 and 7 show the comparison between the numerical predictions and the experimental data of the plate fin heat sink. As can be seen in Figures 6 and 7, when the inlet velocity increases, larger pressure drop is acquired, while the thermal resistance of the heat sink decreases dramatically. It can also be seen that the predicted results are in excellent agreement with the experimental data.

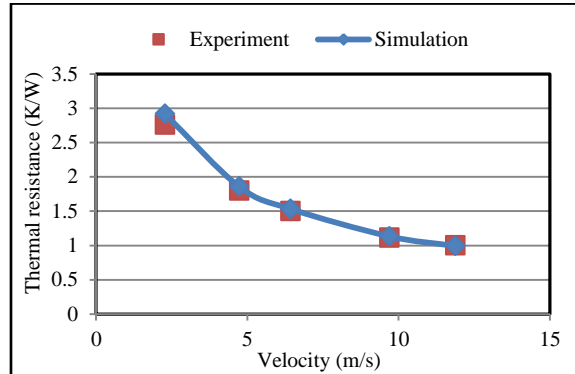


Figure 5. Thermal behavior of plate fin heat sink

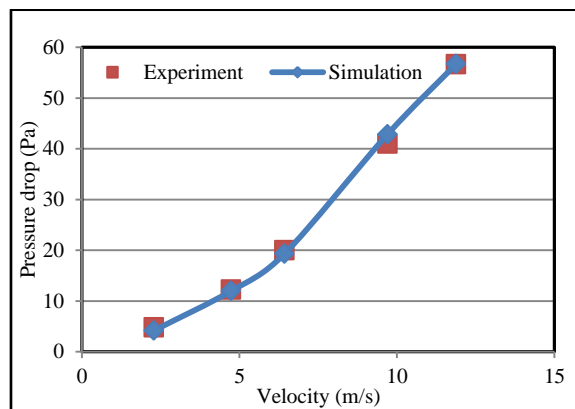


Figure 6. Hydraulic behavior of plate fin heat sink

Figures 8 and 9 provide a comparison between the simulation results and experimental data of the circular pin fin heat sink. The predictions of the simulation correspond well to the experimental results.

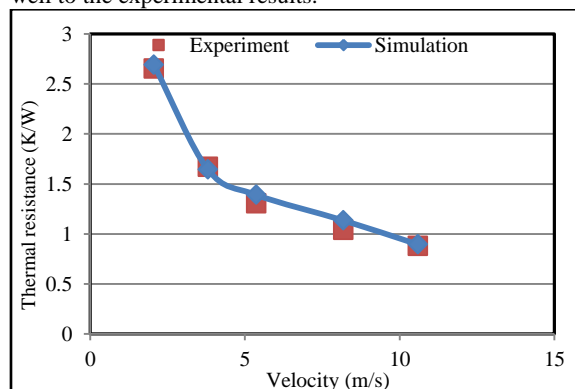


Figure 7. Thermal behavior of circular pin fin heat sink

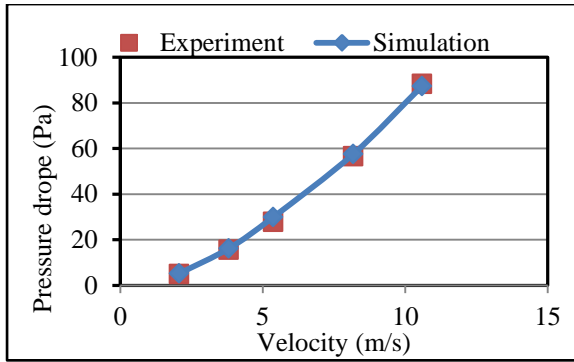


Figure 8. Hydraulic behavior of circular pin fin heat sink

Comparison between plate fin and circular pin fin heat sinks are plotted in Figures 10 and 11. From Figure 10, it is clear that the circular pin fin heat sink has a lower thermal resistance than the plate fin heat sink, which agrees with the experimental data of Jonsson and Moshfegh [4]. As a result, the circular pin fin displayed higher heat transfer rate compared to the plate fin. However, comparisons of pressure drop are presented in Figure 11 and it shows that the circular pin fin heat sink has higher pressure drop than the plate fin heat sink.

The temperature distributions on plate fin and circular pin fin heat sinks are shown in Figures 12 and 13. In these figures, heat transfer range is identified by colour changes on the plate and pin surfaces.

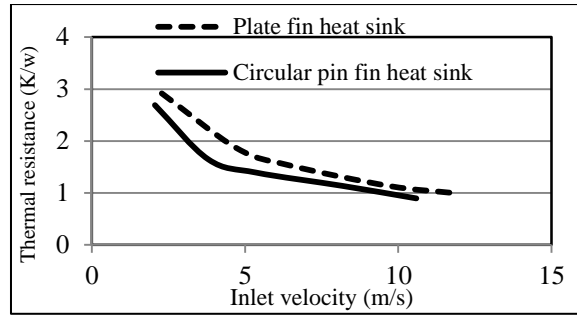


Figure 9. Comparison of thermal resistance between plate fin and circular pin fin heat sink

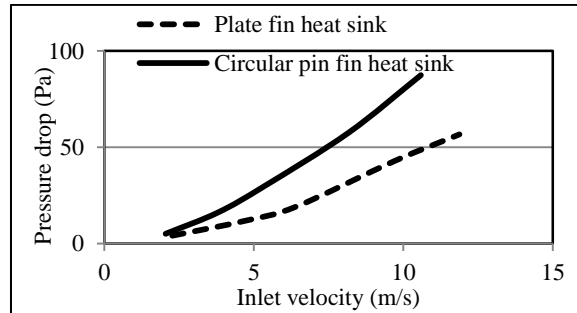


Figure 10. Comparison of pressure drop between plate fin and circular pin fin heat sink

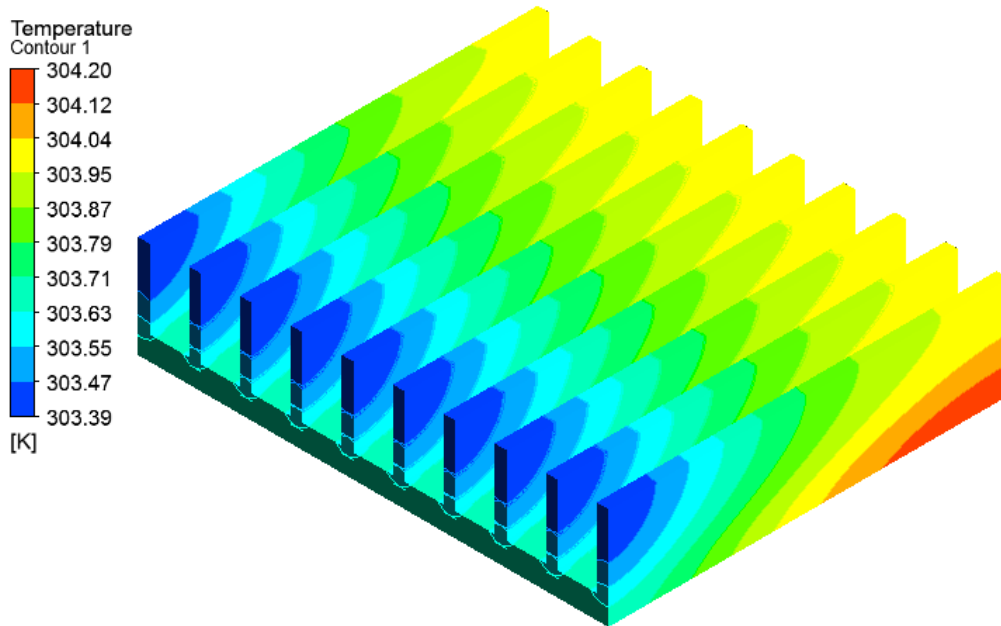


Figure 11. Temperature distributions on plate heat sink

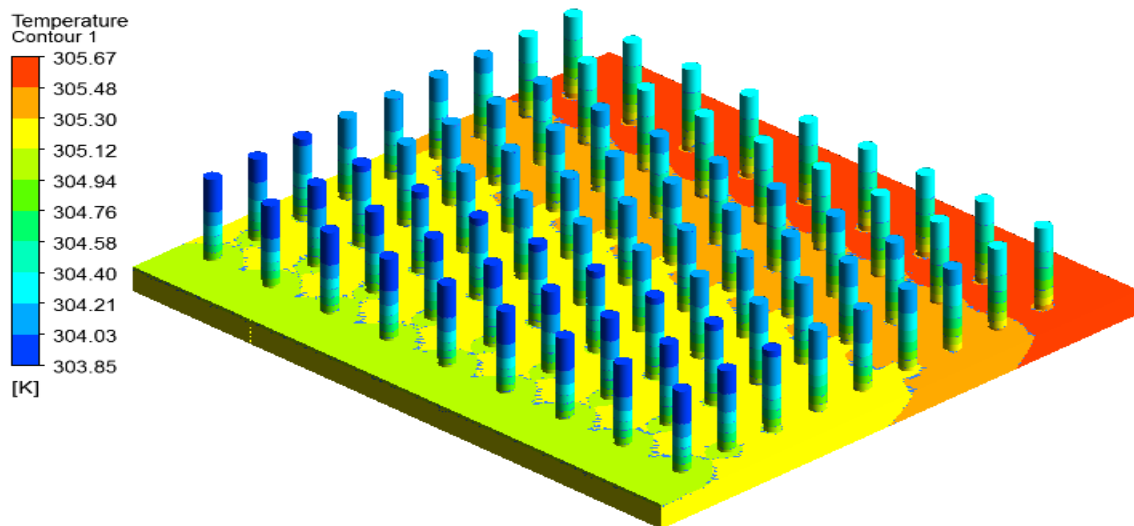


Figure 12. Temperature distribution on circular pin fin heat sink

#### 4. Conclusions

In the present study, the plate fin and circular pin fin heat sinks were simulated with inlet velocity varies from 2 m/s to 12 m/s. Three dimensional computations were implemented on a single flow passage with a periodic boundary condition. The thermal resistance and pressure drop of the heat sinks were predicted. The results show that increasing the flow velocity reduces the thermal resistance and increases the pressure drop simultaneously. The two models of the heat sink were compared with experimental data and excellent agreement was found. A comparison between the two heat sinks was made and it was found that pin fin heat sink has lower thermal resistances than plate fin heat sink. Therefore, circular pin fin heat sink displayed higher heat transfer rate than the plate fin heat sink. Future work has to consider different geometrical parameters to achieve efficient performance.

#### References

- [1] D. B. TUCKERMAN, R. F. W. PEASE, "High-performance heat sinking for VLSI". *Electron Device Letters, IEEE*, Vol. 2 (1981) No. 5, 126-129.
- [2] A. WEISBERG, H. H. BAU, J. N. ZEMEL, "Analysis of microchannels for integrated cooling". *International Journal of Heat and Mass Transfer*, Vol. 35 (1992) No. 10, 2465-2474.
- [3] P. TEERTSTRA, M. M. YOVANOVICH, J. R. CULHAM, "Analytical forced convection modeling of plate fin heat sinks". *Journal of Electronics Manufacturing*, Vol. 10 (2000) No. 4, 253-261.
- [4] H. JONSSON, B. MOSHFEGH, "Modeling of the thermal and hydraulic performance of plate fin, strip fin, and pin fin heat sinks-influence of flow bypass". *Components and Packaging Technologies, IEEE Transactions on*, Vol. 24 (2001) No. 2, 142-149.
- [5] Z. DUAN, Y. S. MUZYCHKA, "Experimental investigation of heat transfer in impingement air cooled plate fin heat sinks". *Journal of electronic packaging*, Vol. 128 (2006) No. 4, 412-418.
- [6] Y.-T. YANG, H.-S. PENG, "Investigation of planted pin fins for heat transfer enhancement in plate fin heat sink". *Microelectronics Reliability*, Vol. 49 (2009) No. 2, 163-169.
- [7] A. R. BETZ, D. ATTINGER, "Can segmented flow enhance heat transfer in microchannel heat sinks?". *International Journal of Heat and Mass Transfer*, Vol. 53 (2010) No. 19, 3683-3691.
- [8] H. A. MOHAMMED, P. GUNNASEGARAN, N. H. SHUAIB, "Influence of channel shape on the thermal and hydraulic performance of microchannel heat sink". *International Communications in Heat and Mass Transfer*, Vol. 38 (2011) No. 4, 474-480.
- [9] H. A. MOHAMMED, P. GUNNASEGARAN, N. H. SHUAIB, (2011) "Numerical simulation of heat transfer enhancement in wavy microchannel heat sink". *International Communications in Heat and Mass Transfer*, Vol. 38 (2011) No. 1, 63-68.
- [10] H.-T. CHEN, S.-T. LAI, L.-Y. HAUNG, "Investigation of heat transfer characteristics in plate-fin heat sink". *Applied Thermal Engineering*, Vol. 50 (2012) No. 1, 352-360.
- [11] Y.-T. YANG, S.-C. LIN, Y.-H. WANG, J.-C. HSU, "Numerical simulation and optimization of impingement cooling for rotating and stationary pin-fin heat sinks". *International Journal of Heat and Fluid Flow*, Vol. 44 (2013), 383-393.
- [12] M. HATAMI, D. D. GANJI, "Thermal and flow analysis of microchannel heat sink (MCHS) cooled by Cu-water nanofluid using porous media approach and least square method". *Energy Conversion and Management*, Vol. 78 (2014), 347-358.
- [13] T.-M. JENG, S.-C. TZENG, Q.-Y. HUANG, "Heat transfer performance of the pin-fin heat sink filled with packed brass beads under a vertical oncoming flow". *International Journal of Heat and Mass Transfer*, Vol. 86 (2014), 531-541.
- [14] Y. L. ZHAI, G. D. XIA, X. F. LIU, Y. F. LI, "Exergy analysis and performance evaluation of flow and heat transfer in different micro heat sinks with complex structure". *International Journal of Heat and Mass Transfer*, Vol. 84 (2015), 293-303.
- [15] BIRD, R. B., STEWART, W. E. LIGHTFOOT, E. N. *Transport phenomena*. 2nd ed. John Wiley & Sons, 2007.
- [16] *Ansys Fluent V14.0 Theory guide*, 2011.

# Three-Dimensional Investigations of Stress Intensity Factors in a Rotating Thick-Walled FGM Cylinder

Hadi Eskandari \*

Abadan Institute of Technology, Petroleum University of Technology, Abadan, Iran

Received 31 January 2015

Accepted 31 Desember 2015

## Abstract

The present study focuses on three-dimensional analyses of a thick walled functionally graded material cylinder, containing a longitudinal semielliptical internal surface flaw, and is subjected to an internal pressure and a rotational speed. The cylinder is assumed to be isotropic with exponentially varying elastic modulus through the thickness. The effect of wall thickness on the distribution of stress intensity factor is also studied. The results which are normalized for the advantage of non-dimensional analysis show that the material gradation, the crack geometry and wall thickness have a significant influence on the amount and distribution of stress intensity factors. Numerical results are given to assess the safety of the FGM and homogeneous cracked cylinder. The study is valuable to engineering applications.

© 2016 Jordan Journal of Mechanical and Industrial Engineering. All rights reserved

**Keywords:** Functionally graded materials; 3D finite element analysis; Stress intensity factor, rotating thick-walled cylinder.

## NOMENCLATURE

$a$	= depth of the deepest point on the crack front
$c$	= semi axis of the elliptical crack
$E$	= elastic modulus
$K_I, K_{II}, K_{III}$	= conventional SIFs, modes 1, 2 and 3
$K_{i,non}$	= non dimensional SIFs where $i=I,II,III$
$K_O$	= nominal stress intensity factor
$P_{in}$	= inner pressure of cylinder
$Q$	= shape factor
$R_{in}$	= inner radius of cylinder
$R_{out}$	= outer radius of cylinder
$\beta$	= constant of material non-homogeneity
$\delta$	= small distance
$\zeta$	= non-dimensional normalized coordinates
$\eta$	= relative depth of the crack
$\mu$	= shear modulus
$\nu$	= Poisson's ratio
$\xi$	= aspect ratio
$\sigma_{ij}$	= stress tensor
$\phi$	= parametric angle
$\varsigma, \chi, \psi$	= the local coordinate systems at the crack tip
$\omega$	= constant of thermal non-homogeneity
$\Delta u$	= the crack tip opening displacement
APDL	= ANSYS Parametric Design Language
COD	= Crack Opening Displacements
FGM	= Functionally Graded Material
ID	= Inner Diameter of the cylinder
OD	= Outer Diameter of the cylinder
SIF	= Stress Intensity Factor
TBC	= Thermal Barrier Coating

\* Corresponding author e-mail: eskandari @ put.ac.ir.

## 1. Introduction

Rotating thick-walled cylinders are common in industrial applications, such as shaft of machine, multi-barrel rotary guns in weapon, engine of aircraft and rotating pipeline of petrochemical equipment, etc. Cracks are easy to appear in the internal bore of the cylinder because of the flaw of production and usage [1]. The theory of thick tubes (Lame's theory) shows that the longitudinal cracks located on the internal face of the cylinder are most dangerous [2]. The stress intensity factor calculation on the crack face is of the most important for study of the crack propagation and fatigue life.

Parallel to new industrial developments, it seems that the use of conventional materials in rotating thick-walled cylinders is inadequate. Recent developments in the space, automobile and many modern industries have placed demands on Functionally Graded Material (FGM) cylinders suitable for unusual conditions of pressure, temperature and environment [3].

FGMs have attracted much interest primarily as an alternative to Thermal Barrier Coatings (TBCs), which are used in aerospace and high temperature applications. The possibility of tailoring the desired thermo-mechanical properties holds a wide range application potential for FGMs.

FGMs are multiphase materials in which the volume fractions of the constituents vary continuously as a function of position. Therefore, the mismatch of thermos-

mechanical properties near the bond line is minimized. Another application area of FGMs include their use as interfacial zone between two different layers, improves the bonding strength [4], and reduces the residual stresses, interfacial delamination [5] and stress concentration or stress intensity factors [6,7]. Because of their outstanding advantages over conventional composites and monolithic materials, these materials have received a special attention from engineers and researchers of various fields of interest. Kim and Paulino [8] addressed a wide variety of FGMs applications. Tutuncu [9] considered power series solution for the stresses and displacements in functionally-graded cylindrical vessels subjected to internal pressure alone using the infinitesimal theory of elasticity. Stress analysis of thick-walled tubes, due to the nature of functions, are chosen to describe the inhomogeneous properties of cylinder material, are studied by Fukui and Yamanaka [10].

So far, the effects of material distribution on the characteristics of these materials under various loading conditions and for various geometries have been investigated from different points of view.

Although FGM cylinders can be used in these unusual working conditions, generation of defects such as holes, cavity, and cracks in the material substructures during manufacturing or in-service conditions is inevitable. The fatigue failure of such components often develops from the propagation of surface defects. Therefore, the consideration of fracture mechanic criterion in the design process of this equipment is essential for reliable application in the above mentioned industries. Crack analysis of FGMs is an indispensable task in the optimization, reliable and durable design of functionally graded materials and structures in innovative engineering applications. For crack problems in FGMs with general geometrical and loading conditions, efficient and accurate numerical simulation tools are required due to the high mathematical complexity of the arising governing partial

differential equations. In this regards, there has been extensive research focusing on predicting response of FGM cylinders containing cracks. Afzar and Anisuzzaman [3] considered a thick walled FGM cylinder with two diametrically opposed edge cracks emanating from the inner surface and solved the problem of the Stress Intensity Factor (SIF) by numerical procedures. The FGM cylinder was radially divided into layers of infinitesimal thickness with constant material properties at each layer. Chen [11] determined the SIFs for an internal and an external fully circumferential crack in FGM cylinders subjected to a longitudinal tension. Nami and Eskandari [12] studied three-dimensional investigations of stress intensity factors in a thermo-mechanically loaded cracked FGM hollow cylinder. The cylinder was assumed to be isotropic with exponentially varying elastic modulus through the thickness. The effect of non-uniform coefficient of thermal expansion on the distribution of stress intensity factor was also studied. The problem of the stress intensity factor analysis for cracks located at an arbitrary position in rotating FGM disks is studied by Eskandari [13]. A semi-analytical solution for the purpose of thermo-elastic analysis of functionally graded rotating thick cylindrical pressure vessels with variable thickness subjected to the temperature gradient and internal non-uniform pressure has been performed by Jabbaria and Zamani Nejad [14] by using higher-order shear deformation theory and multi-layer method.

In the present paper, a longitudinal semielliptical internal surface flaw in a rotating thick walled FGM cylinder of thickness  $t$  and internal radius  $R_{in}$  subjected to internal pressure  $P_{in}$  is considered (Fig. 1). The effect of wall thickness of the cylinder on the distribution of stress intensity factor is also studied. The elliptical-arc defect is described by two dimensionless parameters,  $\xi = a/c$  and  $\eta = a/t$ , the so-called aspect ratio and relative depth of the crack, respectively.

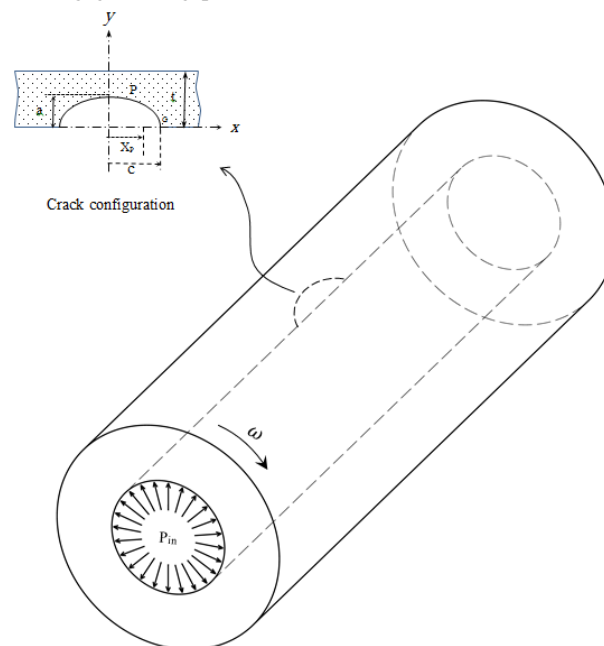


**Figure 1.** Longitudinal internal semi-elliptical surface crack in a rotating thick walled cylinder.

## 2. Stress Intensity Factor of the Functionally Graded Cylinder

### 2.1. Problem Definition

A problem which is encountered in three dimensional finite element analyses is the large number of elements and as a result, a remarkable and time consuming computation. Also, because of very rapid changes in the geometrical parameters around the crack front region, mesh generation of this region must be done with a great care. This may lead to increase the run time which makes it difficult to reach valid results and conclusion. The sub-modeling technique is an advanced numerical tool which solves the problem of analyzing the complex finite element models. This method is also named as the cut-boundary displacement method or the specified boundary displacement method [15]. If the boundary of the sub-model is reasonably selected, and a fine mesh is used in it, the high accuracy results can be achieved [15]. Very rapid changes in the geometrical parameters cause to employ a higher mesh density in the vicinity of the crack front. For such a case, a sub-model technique is employed to overcome the problem. In this technique, a coarse mesh is generated at the first step, and then the region around the geometrical discontinuity, i.e., crack region, is cut. Then the boundary conditions on this cut boundary are extracted from the coarse model and transferred to the cut boundary or 'sub-model'. Finally this sub-model can be analyzed using higher mesh density and accuracy [15].

The present paper studies the stress intensity factor in a rotating thick walled FGM cylinder subjected to the internal pressure. Also, the effects of diameter ratio of cylinder on the SIF's are studied. The results obtained by the 3-D finite element analysis. The special effort is made to condense the SIF data into a compact dimensionless form and to study the effect of material gradation, Diameter Ratio (RD) and the crack depth on the stress intensity factor for points on the crack front. A cylinder of the inside diameter of 45 mm and a total length of 700 mm with different diameter ratios, i.e.,  $\frac{D_{out}}{D_{in}} = \frac{R_{out}}{R_{in}} = 1.5, 2, 2.5, 3$  is considered. The problem has also been examined through the commercial software, ANSYS, which has been used as a finite element solver. The

location of a semi-elliptical surface crack is shown in Fig. 1. The geometry of crack is identified by two dimensionless parameters,  $a/c$  and  $a/t$  which called aspect ratio and relative depth of crack, respectively. Any arbitrary point on the crack front defined by a non-dimensional normalized coordinates as follow;  $\zeta = X_P/X_G$  where  $X_P$  and  $X_G$  are the x-coordinate of the arbitrary point P which generally located on the crack front and the corner point G, respectively (Fig. 1).

### 2.2. Finite Element Modeling

The finite element modeling of cylinder is shown in Figs. (2a-2b). The higher order 3-D 20-node isoparametric brick elements are used everywhere except near the crack front and the singularity elements are applied around the crack front (Fig. (2b)). The singularity elements have square-root terms in their assumed displacement distribution and, therefore, produce a singular stress field at the crack front. The mesh around the crack front is refined enough (i.e., 0.4 mm) to achieve the stress and strain distribution accurately.

The crack front region has been constructed by sweeping an auxiliary area around the crack front line. The auxiliary area is meshed using singular elements around the crack front node and non-singular elements in the remaining part of the area. After this, the half of sub-model is constructed. Then, the next half of sub-model is generated by reflecting the model about the crack plane. By merging the nodes, except those on the crack faces, it becomes possible to model the crack in the cylinder. The whole finite element model has nearly 60,000 elements for the FGM cylinder.

A finite element code can be used to account for spatial variation in material property of FGM cylinder. There are different ways of incorporating changes in material properties into a finite element program. Walter et al. [16] describe two commonly-used methods. An element base method where the desired spatial material property of each element based on its location is achieved through a finite element code. Another way is to compute the material property at each integration point for element stiffness matrix via the spatially varying in material property function.

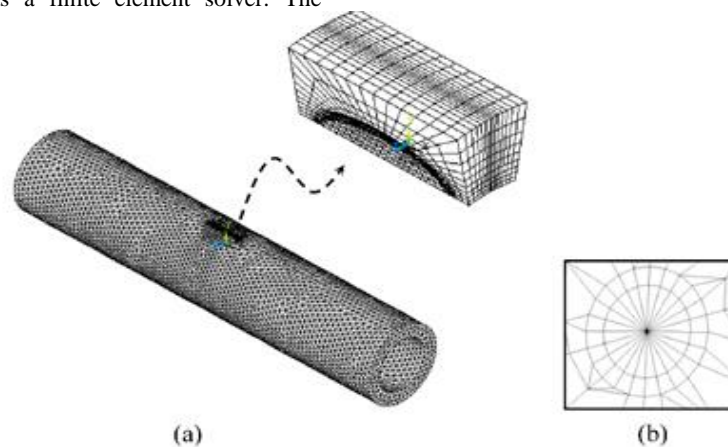


**Figure 2.** Finite element model of cylinder: (a) the whole model and the corresponding sub-model, (b) the singular elements near the crack front

### 2.3. Functionally Graded Cylinder

In the present study, a finite element code using the ANSYS Parametric Design Language (APDL) is used to account the material property changes for each element via its location. This section describes the details of the finite element formulation for stress and fracture analyses of rotating thick walled FGM cylinder. The material is assumed to be isotropic with exponentially varying elastic modulus through the thickness is as follow:

$$E(r) = E_1 e^{\beta(r-r_i)} \quad (1)$$

where,  $r_i$  is the inner radius of cylinder and  $\beta$  is the constant of material non-homogeneity which is defined as:

$$\beta = \frac{1}{w} \ln\left(\frac{E_2}{E_1}\right) \quad (2)$$

where,  $w$  denotes the thickness of cylinder,  $E_1$  and  $E_2$  are the values of elastic modulus at the inner and outer radius of cylinder, respectively. For a simple traceable solution, the dependency on the Poisson's ratio is neglected and it is assumed constant throughout the cylinder.

### 2.4. Crack Tip Fields in FGMs

Material non-homogeneity has a significant influence on SIFs. Eischen [17] established the general form of the stress and displacement fields near a crack tip in a nonhomogeneous material with a spatially varying material property. He solved the problem for materials with continuous, bounded, and differentiable property variations and showed that the asymptotic fields for a crack in a FGM with continuous mechanical properties are same as those of a crack embedded in a homogeneous material. In addition, the asymptotic displacement expressions for the homogeneous materials can be used for FGMs on condition that the material properties are calculated at the crack-front location.

Since the nature of the stress singularity for continuously non-homogenous, isotropic and linear elastic solid is precisely the same as the well-known form applicable to homogeneous materials, irrespective of the particular form of the Young's modulus variation [17], the stress intensity factors can be obtained from Crack-Opening-Displacements (CODs) as [18]:

$$\begin{Bmatrix} K_I \\ K_{II} \\ K_{III} \end{Bmatrix} = \frac{\mu_{tip} \sqrt{2\pi}}{4(1-\nu)} \lim_{\delta \rightarrow 0} \frac{1}{\sqrt{\delta}} \begin{Bmatrix} \Delta u_\zeta(\delta) \\ \Delta u_\chi(\delta) \\ (1-\nu)\Delta u_\psi(\delta) \end{Bmatrix}$$

where  $K_I$ ,  $K_{II}$  and  $K_{III}$  are opening, sliding and tearing modes of SIFs,  $\mu_{tip}$  is the shear modulus at the crack front,  $\delta$  which approaches zero is a small distance between specified node at crack-surface and a node at crack-front, and  $\Delta u_I(X) = [u_I(X \in \text{upper crack surface}) - u_I(X \in \text{lower crack surface})]$  in which  $I = \zeta, \chi$  and  $\psi$  are the CODs in the local coordinate systems.

The stress intensity factor for cylinder is considered in the non-dimensional form and is defined as:

$$K_{I,non} = \frac{K_I}{K_0} \quad (3)$$

In which  $K_I$  is the calculated values of the stress intensity factors and  $K_0$  is the nominal stress intensity factor. The nominal stress intensity factor for FGM cylinders are used as:

$$K_0 = \frac{2 P_{in} (R_{out})^2}{(R_{out})^2 - (R_{in})^2} \sqrt{\frac{\pi a}{Q}} \quad \text{for plane stress} \quad (4)$$

where the shape factor,  $Q$ , is approximated by

$$Q = 1 + 1.464 \left(\frac{a}{c}\right)^{1.65} \quad (5)$$

It should be noted that the nodes near the surface of the plate are in the plane stress conditions. Through thickness nodes, far from the plate surface are in plane strain situations. Plan strain stress intensity factor differs by the coefficient of  $\frac{1}{1-\nu}$  from the plane stress ones.

## 3. Numerical Results

### 3.1. The Validation of the Method

To justify the reliability of the method, a semi-elliptical surface crack in a FGM plate under tension is considered. Figure 3 shows the configuration and location of the crack in the plate. It is assumed that the material gradient is in the  $y$ -direction, i.e.  $E(y) = E_1 e^{\beta(y)}$ . The crack parameters are supposed as  $\xi = \frac{1}{3}$  and  $\eta = 0.8$  and the ratio of Young modulus in FGM plate is considered as  $E(y=t)/E(0) = 0.2$ . The constant value of 0.3 is used for Poisson's ratio throughout the material. The corresponding homogenous case is also considered and compared to the FGM solution.

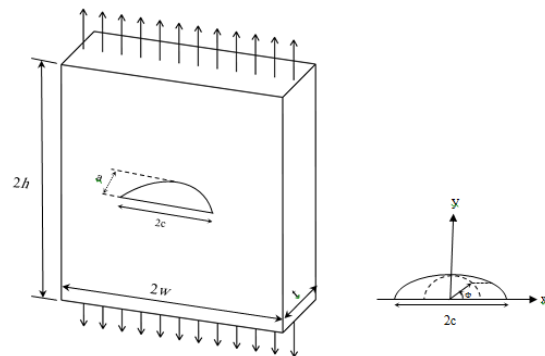


**Figure 3.** Semi-elliptical surface crack in a FGM plate under tension

The distribution of normalized stress intensity factor through the semi-elliptical surface crack with  $a/c = 0.33$  and  $a/t = 0.8$  as a function of the parametric angle for both the FGM and homogenous plates under uniform tension loading is shown in Figure 4. In this case, it is assumed that the FGM plate has the material gradation equal to 0.2. The results are compared with those reported by Yildirim *et al.* [19] showing to be in a good agreement for both cases. It is noteworthy that, for symmetry, only one-half of crack front is considered.

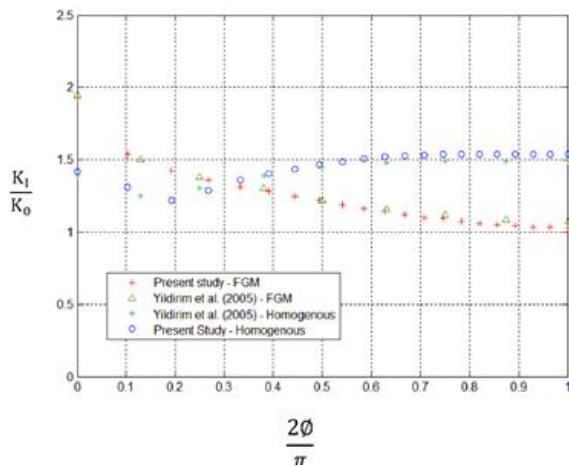


**Figure 4.** Variation of the normalized mode-I stress intensity factor on the crack front in a FGM plate with  $\xi = \frac{1}{3}$ ,  $\eta = 0.8$ ,  $\nu = 0.25$ ,  $E(r_o)/E(r_i) = 0.2$  and homogeneous material.

### 3.2. Results and Discussion

#### 3.2.1. Pressurized Rotating Thick Walled FGM Cylinder

In the present study, we considered a semi-elliptical surface crack in a rotating thick-walled FGM cylinder subjected to the internal pressure of 5 MPa. The constant value of 0.30 is used for Poisson's ratio throughout the material. The rotation speed of cylinder with inner diameter of 90 mm and different wall thicknesses is considered as 1300 rad/s.

The distributions of mode I stress intensity factors along the crack front as a function of the normalized coordinate ( $\zeta$ ), for a FGM and corresponding homogeneous rotating cylinder are compared in Figs. (5a-5e). Each curve is plotted for a certain values of relative crack depth ( $\eta$ ), material gradation ( $RE = E_2/E_1$ ), i.e., 0.2, 2, 5, 10 and for different values of aspect ratio ( $\xi$ ). The results are compared for corresponding homogeneous material ( $E_2/E_1 = 1$ ) in Fig. (5d).

It can be observed from Fig. 5a that for  $\eta = 0.1$  and  $RE = 0.2$ , the higher values of aspect ratios ( $\xi$ ), the smaller values of  $K_I$  in midpoints of the crack fronts. In other words, for corner points of the crack fronts, the higher values of aspect ratios, the higher values of  $K_I$ . The effects of material gradation on variation of first mode of the stress intensity are studied in Fig. 6. The following results can be seen from the figures:

- It can be seen that the distribution of the  $K_I$  along the crack front is symmetric on both sides of the deepest point, and the stress intensity factors at the corner points are the same. It may be concluded that, regarding the probable crack growth, the corner points start to propagate simultaneously. Moreover, the same crack growth rates are expected to be seen at both sides of the crack.
- The distribution of the SIF on the crack front tends to a parabola like shape and the critical point on the crack front in rotating FGM cylinders with low material gradation ( $RE = E_2/E_1 < 1$ ) depends on the value of aspect ratio.
- For rotating FGM cylinders with small values of material gradation ( $RE = E_2/E_1 < 1$ ), as the aspect ratio

increases, the deepest point of the crack front tends to be safer than corners in probable crack growth. In other words, in cracks with small aspect ratios the deepest point will propagate sooner than corners. Cracks with large values of aspect ratio apt to grow in corners sooner than others.

- For large values of material gradation ( $RE \gg 1$ ), as the aspect ratio decreases, the critical point happens at the deepest points and the corner points experiences minimum value of the stress intensity factor.
- The points on the crack fronts in rotating cylinders with high material gradation and large values of aspect ratio grow simultaneously in same manner.
- For homogeneous rotating cylinder, the critical point of the stress intensity factor depends on the aspect ratio of the crack. For small values of the aspect ratio, the critical point is always one between the two corner points. The maximum stress-intensity factor occurs at the deepest point.
- In a certain value of material gradation, higher the aspect ratio, higher the  $K_I$  at corners. For large values of the aspect ratio,  $K_I$  increases dramatically in corners.
- The points far from corners on the crack front in a homogenous rotating cylinder have the same values of SIF and the distribution of  $K_I$  on the crack front is nearly linear. The gradation in material cause to change it to a parabola like shape.
- Higher the material gradation, smaller the stress intensity factor in corners. In other words, increasing the material gradation will decrease the risk of crack propagation on the deepest point.

The effect of Diameter Ratio (RD) on the distribution of the  $K_I$  along a crack front with constant aspect ratio and relative crack depth ( $\eta = \xi = 0.4$ ) for different gradation of materials, i.e. 0.2, 1, 2, 5 and 10 are studied in Fig. (7a-7e). The effects of internal pressure and rotational speed of the cylinder on the distribution of the mode-I stress intensity factor along the crack front are depicted in Figs. 8-9. A general investigation of graphs demonstrates that the wall thickness variation causes the following results:

- Higher the diameter ratio, higher the  $K_I$  along the crack front. In other words, in probable crack growth, cylinders with smaller diameter ratios are more reliable than others.
- In a certain value of wall thickness, higher the material gradation, smaller the  $K_I$  at corners. In other words, for large gradation of materials ( $RE > 1$ ) with constant diameter ratio, smaller the material gradation, smaller the  $K_I$  at the deepest point.
- Smaller the material gradation, higher the effects of diameter ratio on the values of stress intensity factor on the crack fronts. It means that in a constant value of diameter ratio, the maximum SIF occurs on cylinders with smaller gradation of materials.
- Higher the internal pressure, higher the values of the SIFs along the crack front.
- The rotational speed of the cylinder significantly affects on the values of the stress intensity factors along the crack fronts. As seen, with increasing the rotational speed of the cylinder the stress intensity is increased.

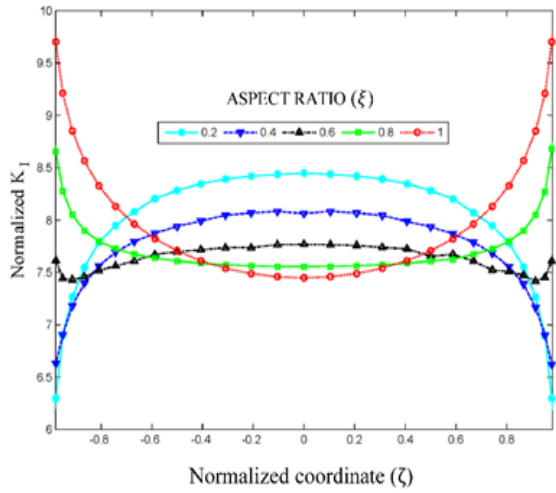


Fig. 5a

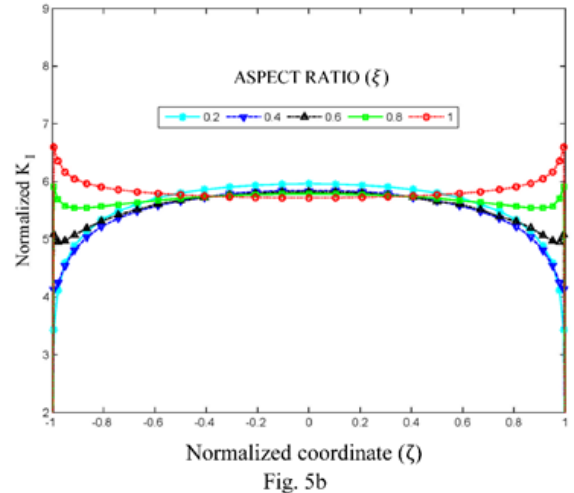


Fig. 5b

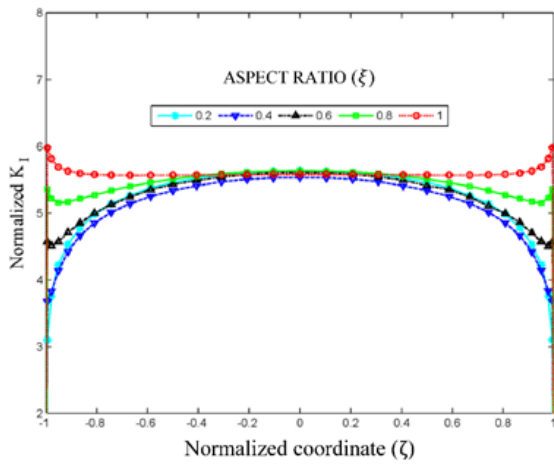


Fig. 5c

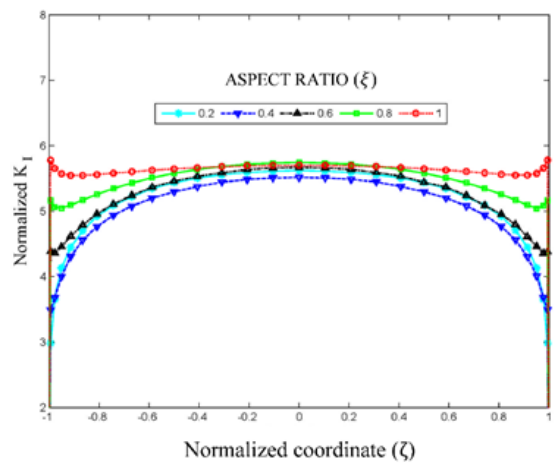


Fig. 5d

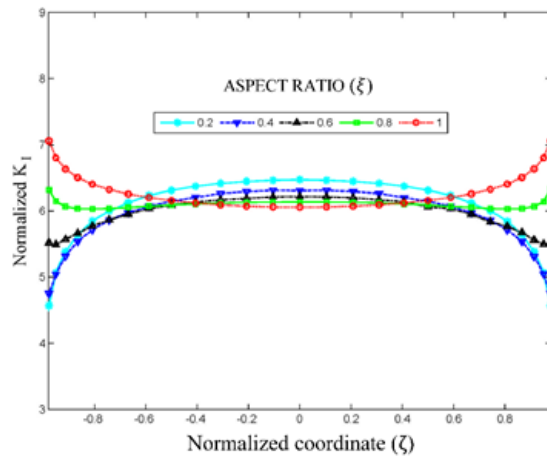
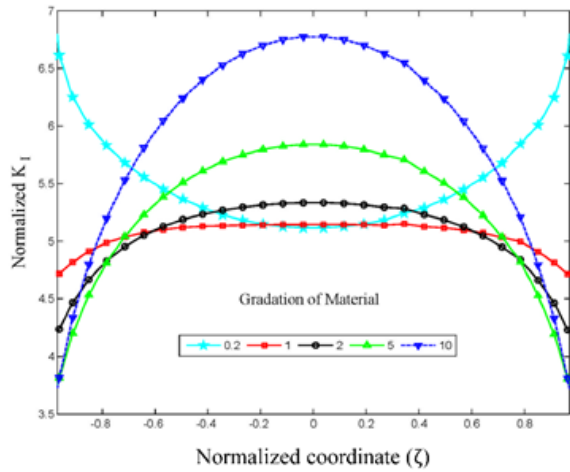
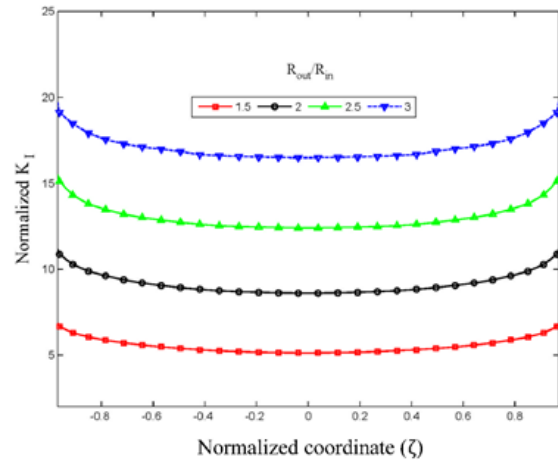


Fig. 5e

**Figure 5.** Distribution of the first mode stress intensity factor along the crack front in a rotating FGM and homogeneous cylinder with  $\eta = 0.1$ ,  $\nu = 0.3$ , diameter ratio (RD) = 1.5 and for different values of aspect ratios ( $\xi$ ) with material gradation of: a) RE=0.2; b) RE=2; c) RE=5; d) RE=10 e) RE=1(homogeneous material).



**Figure 6.** Distribution of the normalized  $K_I$  along the crack front in a rotating FGM cylinder with different values of material gradation for constant  $\eta = \xi = 0.4$ ,  $\nu = 0.30$  and diameter ratio (RD) of 1.5



**Fig. 7a**

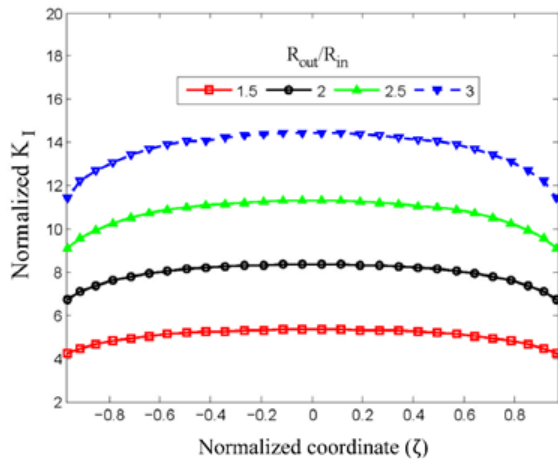


**Fig. 7b**

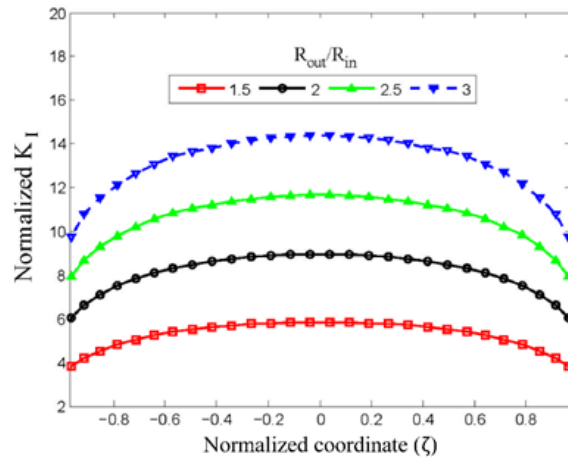


**Fig. 7c**

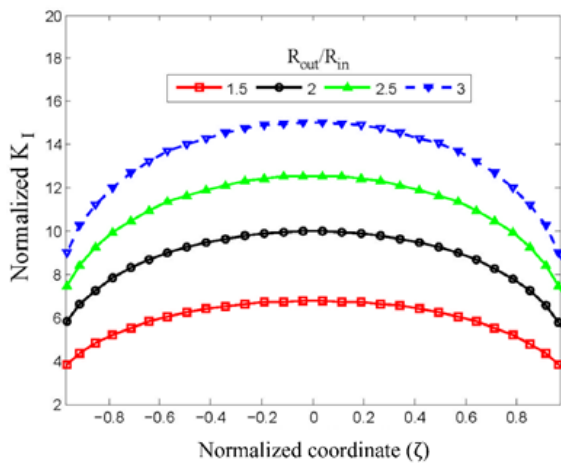


**Fig. 7d**

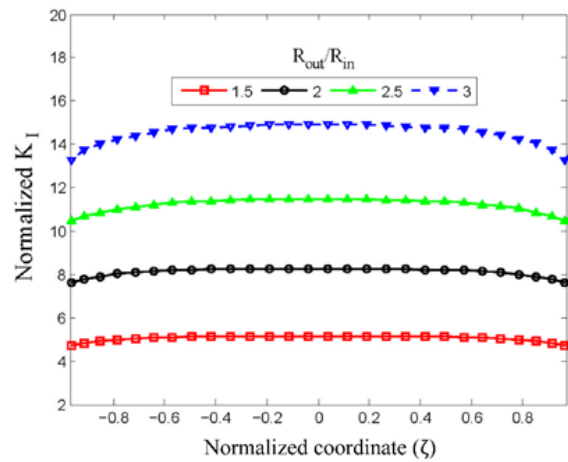


**Fig. 7e**

**Figure 7.** Distribution of the normalized  $K_I$  along the crack front in a rotating FGM and homogeneous cylinder for different values of diameter ratios (RD) with  $\eta = \xi = 0.4$ ,  $\nu = 0.3$  and different gradation of materials; a) RE=0.2; b) RE=2; c) RE=5; d) RE=10 e) RE=1(homogeneous material).

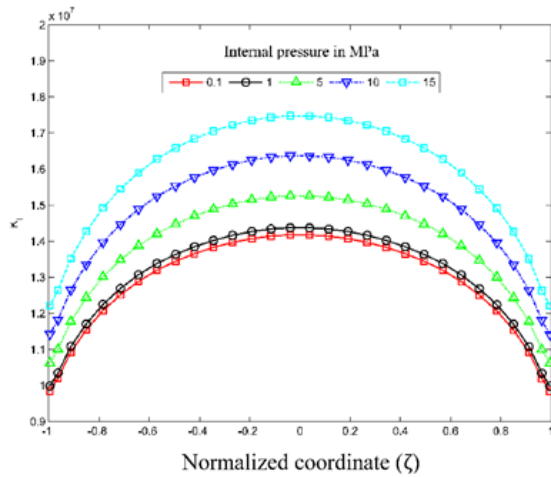


**Figure 8.** Variation of the  $K_I$  along the crack front for different internal pressure in a rotating FGM cylinder with  $\eta = \xi = 0.4$ ,  $RE=2$ ,  $RD=2$ .

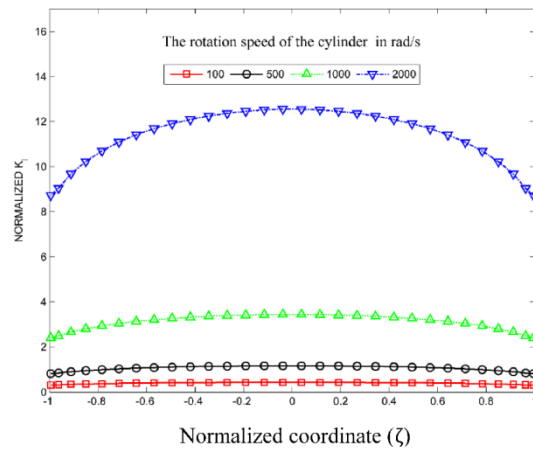


**Figure 9.** Variation of the normalized  $K_I$  along the crack front in a rotating FGM cylinder for different rotational speed with  $\eta = \xi = 0.4$ ,  $RE=2$ ,  $RD=2$ .

#### 4. Summary and Conclusions

In this study, three dimensional finite element analyses of a rotating FGM and homogeneous cylinder containing a semi longitudinal elliptical surface crack under internal pressure is carried out. At first, only the effect of exponentially varying elastic modulus through the thickness is studied. Then the effect of diameter ratio on  $K_I$  is also considered.

In both cases, the distribution of SIF's along the crack front is studied and the effect of aspect ratio of crack ( $a/c$ ) is investigated. It can be seen that the distribution of the  $K_I$  along the crack front is symmetric on both sides of the deepest point, and the stress intensity factors at the corner points are the same.

Depends on the material gradation, diameter ratio and the crack geometry, the values of the SIF at the corners or the deepest point are the critical ones.

#### 5. Acknowledgments

The author gratefully acknowledges the supports of Abadan Institute of Technology, Petroleum University of Technology, Abadan, Iran.

#### References

- [1] A. Chen, W. Zeng, "Weight function for stress intensity factors in rotating thick-walled cylinder". *Applied Mathematics and Mechanics*, Vol. 27 (2006) No.1, 29-35.
- [2] B. El Khalil Hachi, S. Rechak, Y. Belkacemi, G. Maurice, "Modeling of elliptical cracks in an infinite body and in a pressurized cylinder by a hybrid weight function approach". *International Journal of Pressure Vessels and Piping*, Vol. 82 (2005), 917-924.
- [3] A.M. Afsar, M. Anisuzzaman, "Stress intensity factors of two diametrically opposed edge cracks in a thick-walled functionally graded material cylinder". *Engineering Fracture Mechanics*, Vol. 74 (2007), 1617-1636.
- [4] K. Kurihara, K. Sasaki, M. Kawarada, "Adhesion improvement of diamond films". In M. Yamanouchi, M. Koizumi, T. Hirai and I. Shiota (eds.) *Proceedings of the First*

International Symposium on Functionally Graded Materials, Tokyo, Japan, 1990, 65-69.

- [5] Y.-D. Lee, F. Erdogan, "Residual/thermal stresses in FGM and laminated thermal barrier coatings". *International Journal of Fracture*, Vol. 69 (1995) No. 2, 145-165.
- [6] F. Erdogan, "Fracture mechanics of functionally graded materials". *Composites Engineering*, Vol. 5 (1995) No. 7, 753-770.
- [7] J.-H. Kim, G.H. Paulino, "Isoparametric graded finite elements for nonhomogeneous isotropic and orthotropic materials". *Journal of Applied Mechanics*, Vol. 69 (2002a) No. 4, 502-514.
- [8] J.-H. Kim, G.H. Paulino, "Finite element evaluation of mixed mode stress intensity factors in functionally graded materials". *International Journal for Numerical Methods in Engineering*, Vol. 53 (2002b), 1903-1935.
- [9] N. Tutuncu, "Stresses in thick-walled FGM cylinders with exponentially-varying properties". *Engineering Structures*, Vol. 29 (2007), 2032-2035.
- [10] Y. Fukui, N. Yamanaka, "Elastic analysis for thick-walled tubes of functionally graded material". *Japan Society of Mechanical Engineering International Journal Ser I: Solid Mechanics Strength of Materials*, Vol. 35 (1992) No. 4, 379-85.
- [11] Y.Z. Chen, "Stress intensity factors in a finite cracked cylinder made of functionally graded materials". *International Journal of Pressure Vessels and Piping*, Vol. 81(2004), 941-947.
- [12] M.R. Nami, H. Eskandari, "Three-dimensional investigations of stress intensity factors in a thermo-mechanically loaded cracked FGM hollow cylinder". *International Journal of Pressure Vessels and Piping*, Vol. 89 (2012), 222-229.
- [13] H. Eskandari, "Stress intensity factors for crack located at an arbitrary position in rotating FGM disks". *Jordan Journal of Mechanical and Industrial Engineering*, Vol. 8 (2014) No. 1, 27-34.
- [14] M. Jabbaria, M. Zamani Nejad, "Thermo-elastic analysis of axially functionally graded rotating thick cylindrical pressure vessels with variable thickness under mechanical loading". *International Journal of Engineering Science*, Vol. 96 (2015), 1-18.
- [15] Q.Z. Wang, X.M. Jia, "More accurate stress intensity factor derived by finite element analysis for the ISMR suggested rock fracture toughness specimen-CCNBD". *International Journal of Rock Mechanics and Mining Science*, Vol. 40 (2003), 233-241.

- [17] M.C. Walters, G.H. Paulino, R.H. Dodds, "Stress-intensity factors for surface cracks in functionally graded materials under mode-I thermomechanical loading". *International Journal of Solids and Structures*, Vol. 41 (2004), 1081–1118.
- [18] J.W. Eischen, "Fracture of non-homogeneous materials". *International Journal of Fracture*, Vol. 34 (1987), 3–22.
- [19] Ch. Zhang, M. Cui, J. Wang, X.W. Gao, J. Sladek, V. Sladek, "3D crack analysis in functionally graded materials". *Engineering Fracture Mechanics*, Vol. 78 (2011), 585-604.
- [20] B. Yildirim, S. Dag, F. Erdogan, "Three dimensional fracture analysis of FGM coatings under thermomechanical loading". *International Journal of Fracture*, Vol. 132 (2005), 369–395.



# Optimization of Resistance Spot Welding Process Parameters on Shear Tensile Strength of SAE 1010 steel sheets Joint using Box-Behnken Design

Shashi Dwivedi<sup>a,b,\*</sup>, Satpal Sharma<sup>a</sup>

<sup>a</sup>School of Engineering, Gautam Buddha University, Greater Noida, Gautam Buddha Nagar, U.P. 201310, India

<sup>b</sup>Noida Institute of Engineering Technology, Greater Noida, Gautam buddha Nagar, U.P. 201310, India

Received 5 January 2014

Accepted 7 March 2016

## Abstract

In the present investigation, SAE 1010 steel sheets are welded by resistance spot welding. The welding current, welding cycle and electrode force are the principal variables that are controlled in order to provide the necessary combination of heat and pressure to form the weld. Response surface methodology (Box-Behnken Design) is chosen to design the experiments. In the range of process parameters, the result shows that as welding current increases shear tensile strength decreases, whereas welding time (cycle) and electrode force increase shear tensile strength increase. From the ANOVA table it can be concluded that electrode force is contributing more and it is followed by welding time and welding current. Optimum values of welding current (6 kA), welding time (25 cycle) and electrode force (4.5 kN) during welding of SAE 1010 steel sheets joint to maximize the shear tensile strength (Predicted 8.214 kN) have been find out. There was approximately 6.12 % error was found between experimental and modeled result.

© 2016 Jordan Journal of Mechanical and Industrial Engineering. All rights reserved

**Keywords:** Resistance spot welding, Box Behnken Design, SAE 1010 steel, Welding current, Shear Tensile strength.

## 1. Introduction

Resistance spot welding (RSW) has an important place in manufacturing and it is the simplest and most widely used form of the electric resistance welding processes in which faying surfaces are joined in one or more spots [1]. Spot welds are the dominant joining method in the automotive assembly process. As the automated assembly process is not perfect, some spot welds may be absent when the vehicle leaves the assembly line [2, 3].

Resistance Spot welding is a process in which contacting metal surfaces are joined by the heat obtained from resistance to electric current flow. Work-pieces are held together under pressure exerted by electrodes. Typically the sheets are in the 0.5 to 3 mm thickness range. The process uses two shaped copper alloy electrodes to concentrate welding current into a small "spot" and to simultaneously clamp the sheets together. The amount of heat (energy) delivered to the spot is determined by the resistance between the electrodes and the amperage and duration of the current. The amount of energy is chosen to match the sheet's material properties, its thickness, and type of electrodes. Applying too little energy won't melt the metal or will make a poor weld [4].

Applying too much energy will melt too much metal, eject molten material, and make a hole rather than a weld. Another attractive feature of spot welding is the energy delivered to the spot can be controlled to produce reliable welds [5,6].

M. Pouranvari [7] *et al.* in 2011 investigated the effect of the welding parameters (welding time, welding current and electrode force) on the overload failure mode and mechanical performance of dissimilar resistance spot welds between drawing quality special killed AISI 1008 low carbon steel and DP600 dual phase steel. Mechanical properties of spot welds are described in terms of failure mode, peak load and energy absorption during the quasi-static tensile-shear test. Three distinct failure modes were observed during the tensile-shear test: interfacial, pullout and partial thickness-partial pullout failure modes. Correlations among failure mode, welding parameters, weld physical attributes and weld mechanical performance are analyzed. Effect of expulsion on mechanical performance of welds is also investigated.

In Sung Hwang [8] *et al.* in 2011 studied on expulsion reduction in resistance spot welding by controlling of welding current waveform and discussed on welding problem such as expulsion in resistance spot welding of high strength steel.

\* Corresponding author e-mail: shashi\_gla47@rediffmail.com.

R.S. Florea [9] *et al.* in 2012 welded 6061-T6 aluminum by resistance spot welding and for characterization. Electron Back Scatter Diffraction (EBSD) scanning, tensile testing, Laser Beam Profilometry (LBP) measurements along with optical microscopy (OM) images, failure loads and deformation of 6061-T6 aluminum alloy were experimentally investigated of resistance spot welding.

Hessamoddin Moshayedi [10] *et al.* in 2012 studied on nugget size growth in resistance spot welding of austenitic stainless steels and developed A 2D axisymmetric electro-thermo-mechanical Finite Element (FE) model is to study the effect of welding time and current intensity on nugget size in resistance spot welding process of AISI type 304L austenitic stainless steel sheets using ANSYS commercial software package.

Shear tensile strength plays a key role in determining the welding strength of the weld plates SAE1010 steel sheets. Shear strength is the strength of a material or component against the type of yield or structural failure where the material or component fails in shear. A shear load is a force that tends to produce a sliding failure on a material along a plane that is parallel to the direction of the force. Welding of sheets by resistance spot welding is dependent on many factors, it is more influenced by parameters like welding current, welding time and electrode force. In the present investigation, response surface methodology (Box-Behnken Design) used to determine the welding process parameters with the optimal shear tensile strength are investigated [11].

## 2. Materials and Methods

### 2.1. Workpiece Material

The present work was planned to optimize the resistance spot welding parameters of SAE 1010 steel sheets with constant thicknesses. The specimens were prepared by cutting the workpiece material into the

suitable dimensions and then cleaned and abraded to prevent high contact resistance which is created due to an oxide layer. The tensile shear test experiments were performed on the specimens according to welding standards of the Resistance Welders Manufacturer Association (RWMA). SAE 1010 steel is used for applications such as cold headed fasteners and bolts, Tubular Products, Bar Products, Wire Products, Fasteners, and Piping Components. The chemical composition (percent by weight), and the mechanical properties of the SAE 1010 steel sheet are given in Table 1 and Table 2, respectively. The dimensions of the specimens used throughout the experiment are also given in Table 3 [12].

**Table 1.** Chemical composition of SAE 1010 steel sheet[13]

Percent Composition	C	Mn	Si	P	S
	0.082	0.62	0.18	0.013	0.016

**Table 2.** Mechanical properties of SAE 1010 steel sheet[13]

Mechanical Properties	Yield Strength	Tensile Strength	% Elongation	Hardness (HB)
	327	418	33.5	78

**Table 3.** Dimensions of the workpieces

Thickness (t) (mm)	Width (W) (mm)	Length (L) (mm)	Contact Overlap (mm)
2	25.4	101.6	25.4

### 2.2. Electrode Material

Copper was used as an electrode material and it was reserved constant during all the seventeen experiments. The electrode was changed with a non-used one for each experiment run to prevent the effect of electrode damage on the nugget formed. Copper electrode dimension, electrode before using and after using are shown in Figure 1 (a), (b) and (c), respectively.

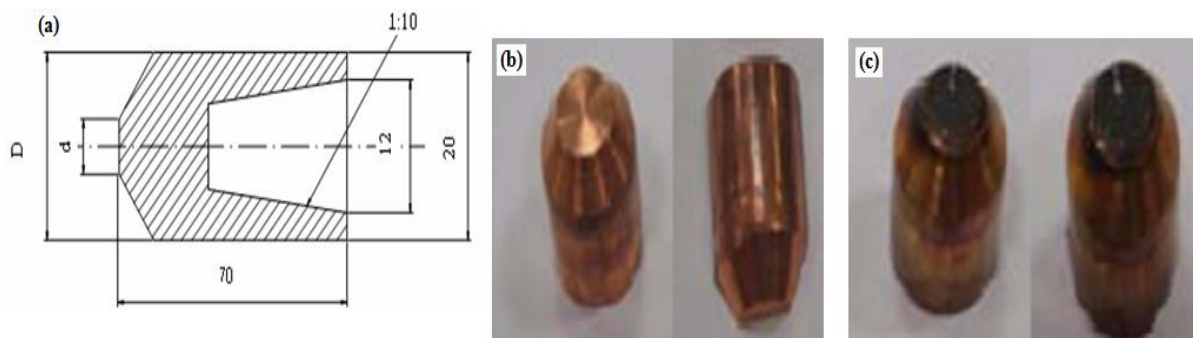


**Figure 1.** Electrode material (a) Copper electrode dimension (b) electrode before using (c) electrode after using

2.3. Experimental Procedure

A Resistance spot welding machine was used for resistance spot welding of SAE 1010 steel sheets with constant thickness 2 mm. The required sensors are placed in relevant positions for most effective detection as shown in Figure 2. The current sensor (not visible) is a Rogowski (air cored) coil. This sensor gives a voltage output proportional to the current induced through the arms of the spot weld machine. The voltage sensor consists of two leads connected to each copper electrode.

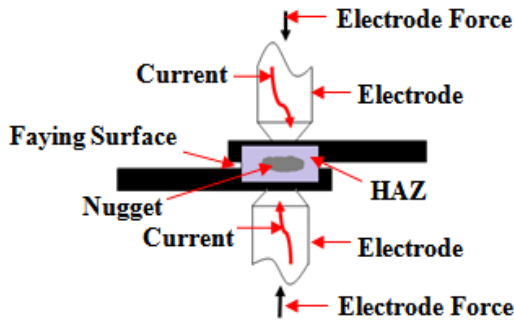


Figure 2. Resistance spot welding process

There are various process parameters of resistance spot welding machine affecting the resistance spot welding characteristics. On the basis of pilot investigations, the following process parameters have been selected for study. Their ranges are given in Table 4.

Table 4. Resistance spot welding process parameters with their ranges

S.No.	Input parameters	Ranges
1	Current (kA)	6 -10
2	Welding time (Cycle)	15 -25
3	Electrode force (KN)	1.5-4.5

Welding of SAE 1010 steel sheet was carried out by resistance spot welding as per the plan of experiments tabulated in Table 5 and measured shear tensile strength measured on tensometer tensile testing machine are also given in Table 5.

2.4. Response Surface Methodology

The response surface methodology is used to design the experiment for the given problem. In this study, three parameters are used as levels that maximize the yield (y) of a process [14]. The process yield is a function of the different constituents, say

$$y = f(x_1, x_2, x_3) + \epsilon \tag{1}$$

where  $\epsilon$  represents the noise or error observed in the response y. if we denote the expected response (tensile strength) by  $E(y) = f(x_1, x_2, x_3, x_4, x_5) = \eta$ , then the response represented [15] by

$$\eta = f(x_1, x_2, x_3) \tag{2}$$

is called a response [16].

Box-Behnken design is used to further study the quadratic effect of factors after identifying the significant factors using screening factorial experiments [17-19].

Table 5. Design matrix and experimental results

Standard Order	Current (kA)	Welding Time (Cycle)	Electrode Force (kN)	Shear Tensile Strength (MPa)
1	10	20	1.5	7.3
2	8	15	4.5	8.1
3	8	25	1.5	7.5
4	8	15	1.5	7.2
5	8	25	4.5	9.4
6	8	20	3	8.2
7	10	15	3	7.7
8	8	20	3	8.15
9	8	20	3	8.2
10	6	15	3	8.7
11	6	25	3	9.4
12	10	20	4.5	8.3
13	10	25	3	8.8
14	6	20	1.5	8
15	8	20	3	8.27
16	8	20	3	8.25
17	6	20	4.5	9.4

3. Results and Discussion

3.1. Macrographic View of SAE 1010 Steel Sheet Joint

Figure 3 shows several macrographic views of the nugget of SAE 1010 steel sheet joint, welded by resistance spot welding in the range of process parameters. The macrographic examinations are carried out to find out the shape of the nuggets. Unbalance heat (beyond the range of process parameters) causes irregular nugget formation (Figure 3 (g)). The weld nugget loses its symmetric form because of the uneven heat ensuing from different physical properties of the steel sheets (SAE 1010 steel sheets). The nugget formation is more active in stainless steel sheet, since stainless steel has a higher electrical resistance. Each macrographic view shows that SAE 1010 steel sheets are fully melted, but sometimes undesired effect is occurred when welding is done at high current as shown in Figure 3(g).

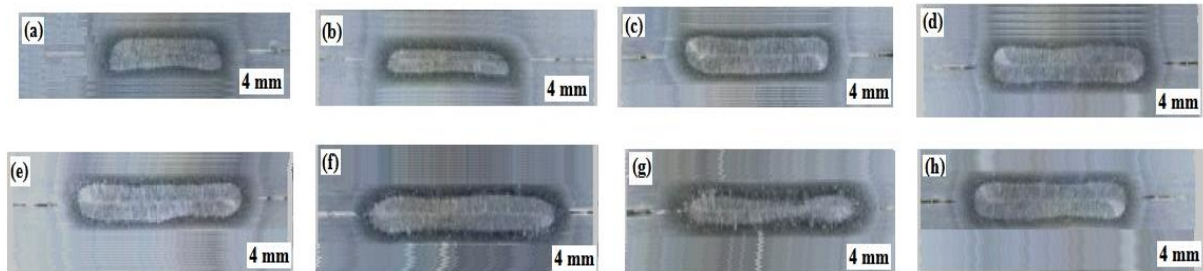


Figure 3: Macrographic views of resistance spot welded joint of SAE 1010 steel sheet at welding current of 6 kA, welding time of 25 cycles and electrode force of 4.5 kN

### 3.2. Micrographic View of SAE 1010 Steel Sheet Joint

Figure 4 presents the micrographic views of the welded specimens joined at various welding current, welding time and electrode forces (in the range of process parameters). It can be seen from Figure 4 that difference in terms of color is identified among the grains due to intergranular direction. Crack and porosity were also not observed around the weld region.

### 3.3. Microstructure Analysis of Welded Joint and HAZ

To examine the microstructure of the weld SAE 1010 steel sheet and heat affected zones, the microstructure analysis was carried out. Figure 5 displays the microstructures of the SAE 1010 steel sheet, weld joint and heat affected zones. Development of grain was observed in SAE 1010 steel sheet and welded joint. Columnar structures were identified in weld nugget zone.

### 3.4. Analysis of Shear Tensile Strength

The preferred experimental design is box behnken design and the design matrix is exposed in Table 5. The analysis of response was done via design expert software. Analysis of variance for tensile strength is given in Table 6. Values of "Prob>F" are less than 0.0500 point out that model terms are significant. From the Table 6, linear terms welding current, welding time, electrode force, square terms of welding current, welding time, electrode force and interaction terms between parameters are significant model terms. Values greater than 0.10 show that model terms are not significant. The final empirical relationship was constructed using only these coefficients, and the developed final empirical relationship is given below:

$$\begin{aligned} \text{Tensile Shear Strength} = & +15.56200 - 1.58450 * \\ & \text{Current} - 0.28380 * \text{Welding Time} + 0.78533 * \\ & \text{Electrode Force} + 1.00000\text{E-}002 * \text{Current} * \\ & \text{Welding Time} - 0.033333 * \text{Current} * \\ & \text{Electrode Force} + 0.033333 * \text{Welding Time} * \\ & \text{Electrode Force} + 0.079500 * \text{Current}^2 + \\ & 4.72000\text{E-}003 * \text{Welding Time}^2 - 0.12533 * \\ & \text{Electrode Force}^2 \end{aligned} \quad (3)$$

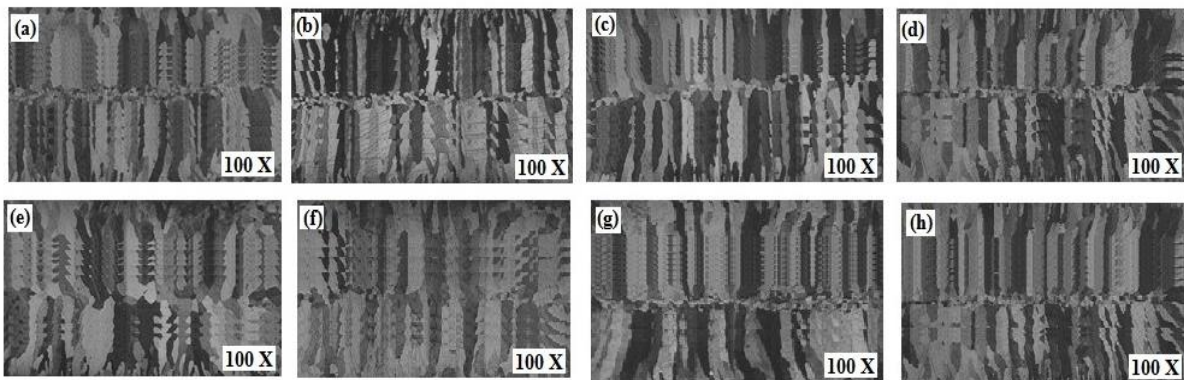


**Figure 4:** Micrographic views of resistance spot welded joint of SAE 1010 steel sheet at welding current of 6 kA, welding time of 25 cycles and electrode force of 4.5 kN

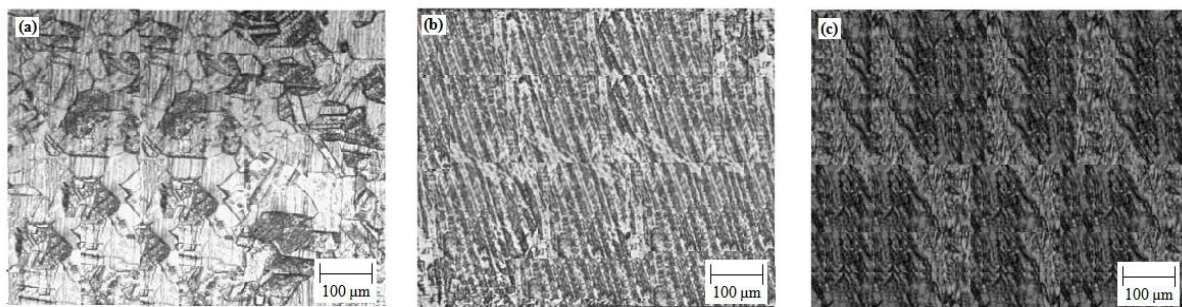


**Figure 5:** Microstructure of (a) SAE 1010 steel sheet, (b) welded joint, (c) HAZ

**Table 6:** Analysis of variance (ANOVA) for shear tensile strength

Source	Sum of Square	DF	Mean Square	F value	Prob.>F	
Model	7.38	9	0.82	147.56	< 0.0001	Significant
A	1.44	1	1.44	259.89	< 0.0001	
B	1.45	1	1.45	259.89	< 0.0001	
C	3.38	1	3.38	607.91	< 0.0001	
AB	0.04	1	0.04	7.19	0.0314	
AC	0.04	1	0.04	7.19	0.0314	
BC	0.25	1	0.25	44.96	0.0003	
A <sup>2</sup>	0.43	1	0.43	76.58	< 0.0001	
B <sup>2</sup>	0.059	1	0.059	10.54	0.0141	
C <sup>2</sup>	0.33	1	0.33	60.22	0.0001	
Residual	0.039	7	5.560E-003			Not Significant
Lack of Fit	0.030	3	0.010	4.48	0.0906	
Pure Error	8.92E-003	4	2.23E-003			
Cor Total	7.42	16				
Std. Dev.		0.075		R-Squared		0.9948
Mean		8.29		Adj R-Squared		0.9880
C.V. %		0.90		Pred R-Squared		0.9335
PRESS		0.49		Adeq Precision		38.469

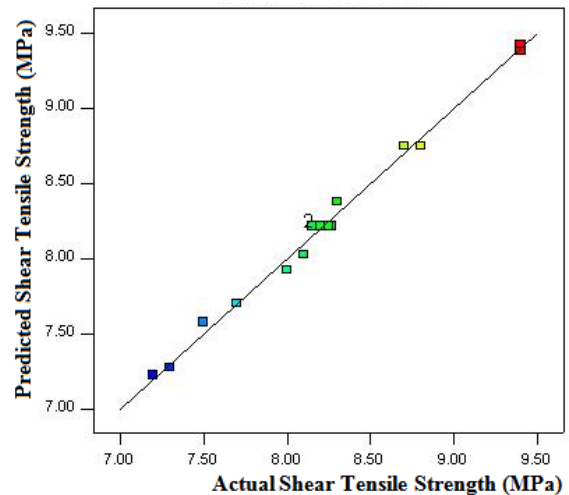
Analysis of variance (ANOVA) method was used to check the adequacy of the developed empirical correlation. In the present work, the preferred level of confidence was measured to be 95%. The model F value of 147.56 reveals that the model is significant. There is only a 0.01% possibility that a model F value this large could take place due to noise. The lack of fit F value of 4.48 indicates that the lack of fit is insignificant. There is only a 9.06% possibility that a lack of fit F value this large could occur due to noise.

The rightness of fit of the model was checked by the determination coefficient ( $R^2$ ). The coefficient of determination ( $R^2$ ) was calculated to be 0.9948 for response (shear tensile strength). This indicates that 99.48% of experimental data confirms the compatibility with the data predicted by the model. The  $R^2$  value is always between 0 and 1, and its value indicates exactness of the model. For a good statistical model,  $R^2$  value should be close to 1.0. The adjusted  $R^2$  value reconstructs the appearance with the significant terms.

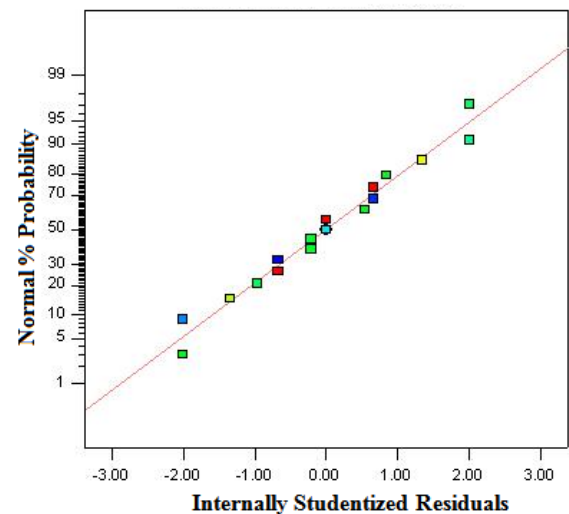
Figure 6 displays the relationship between the predicted and experimental values for shear tensile strength. After the regression model of shear tensile strength was developed, the model adequacy examination was performed in order to validate that the essential assumption of regression analysis is not violated.

Figure 7 shows the normal probability plot of the residual which shows no sign of the violation since each point in the plot follows a straight line pattern. The normal probability plot is used to validate the normality assumption. The data are spread approximately along the straight line. Hence, it is concluded that the data are normally distributed.

The influence of resistance spot welding process parameters like welding current, welding time, electrode force, were evaluated against shear tensile strength of welded shear tensile pieces SAE1010. Figures 8 to 10 show the interaction effect of welding current, welding time and electrode force on shear tensile strength.



**Figure 6:** Correlation between the predicted and actual values of tensile strength in MPa



**Figure 7:** The normal probability of residuals

3.4.1. The Effect of Welding Current on Shear Tensile Strength

Figures 8 and 9 show the effect of welding current on the shear tensile strength of welds indicating that generally increasing welding current, decreases the shear tensile strength. When the current is passed through the electrodes to the sheets, heat is generated, resulting in a

higher electrical resistance produced at the surface contact of SAE 1010 steel sheets. Electrical resistance of the material produces heat between the work pieces and the copper electrodes, the rising heat causes a rising temperature, and results in a molten pool contained most of the time between the electrodes.

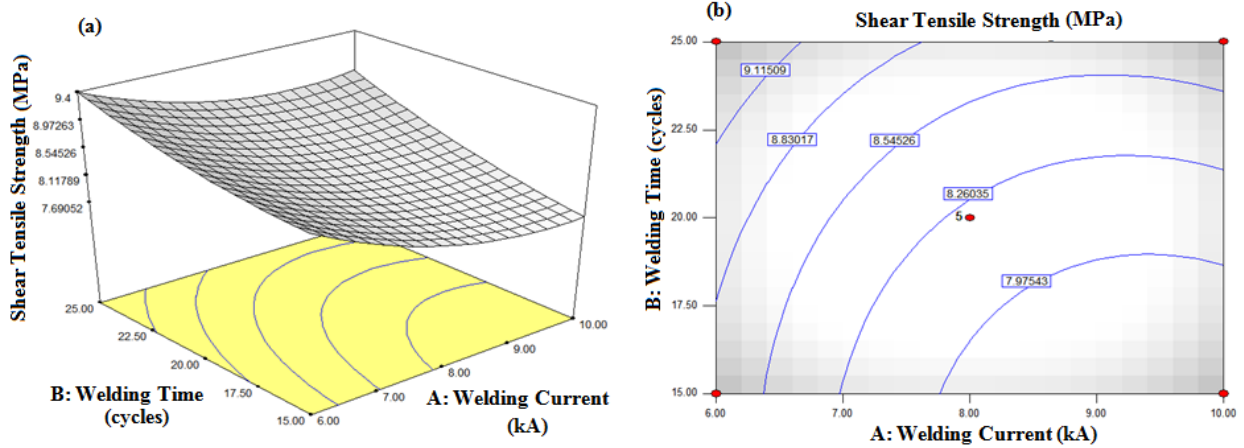


Figure 8: Interaction effect of welding current and welding time on shear tensile strength. (a) 3D interaction (b) the contour plot.

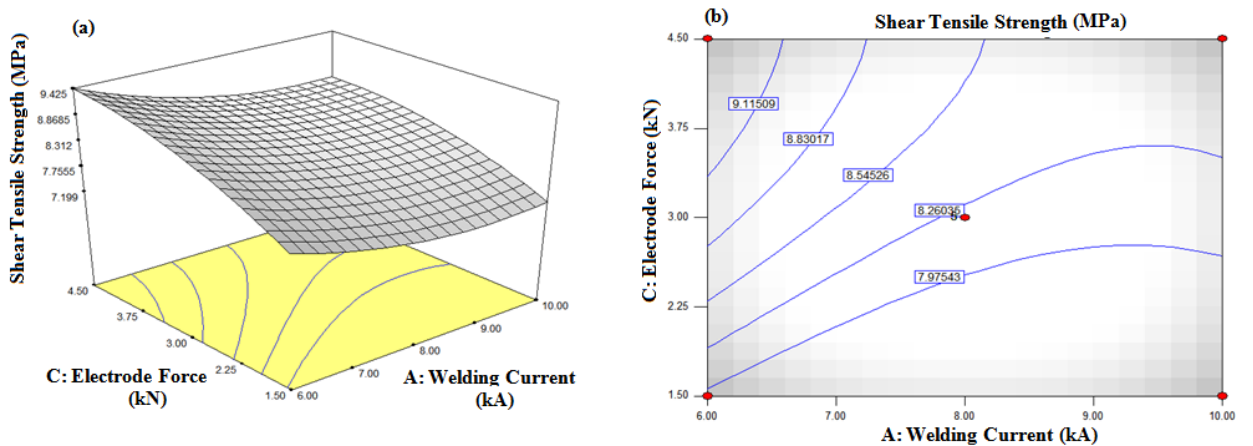


Figure 9: Interaction effect of welding current and electrode force on shear tensile strength. (a) 3D interaction (b) the contour plot

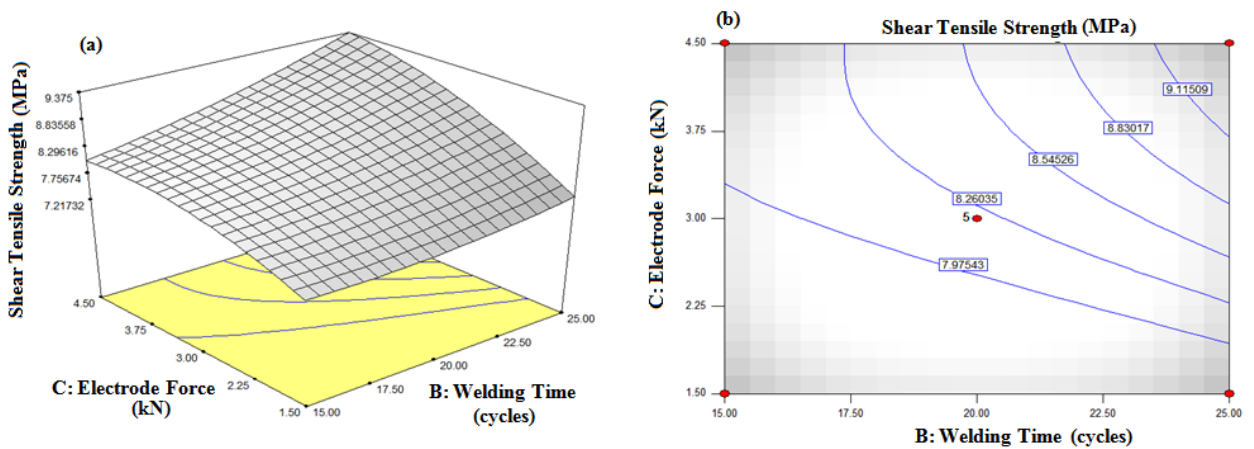


Figure 10: Interaction effect of welding time and electrode force on shear tensile strength. (a) 3D interaction (b) the contour plot

### 3.4.2. The Effect of Welding Time on Shear Tensile Strength

As seen in Figures 8 and 10, welding time (cycle) increases from minimum to maximum limit, the shear tensile strength also increases. When the heat dissipates throughout the workpiece in less time (resistance welding time is generally programmed as cycles), the molten or plastic state grows to meet the welding tips. When the current is stopped, the copper tips cool the spot weld, resulting the metal solidified under pressure.

### 3.4.3. The Effect of Electrode Force on Shear Tensile Strength

In experimental studies shown in Figures 9 and 10, tensile strength increased while electrode force increased because if the electrode force between the base materials is low, then the molten area may extend to the exterior of the work pieces, escaping the containment force of the electrodes. This burst of molten metal is called expulsion, and when this occurs the metal will be thinner and have less shear strength.

### 3.5. Confirmation Experiment

The optimum parameters that give up the maximum shear tensile strength are welding current of 6 kA, welding time of 25 cycles and electrode force 4.5 kN. Importance of process parameters can be ranked from their F ratio which is mentioned in Table 6. . It can be concluded that electrode force is contributing more and it is followed by welding time and welding current. At the 95% PI low value was found 8.020 MPa, while at 95% PI high value was found 8.4071 kN. The average achievable predicted shear tensile strength is found to be 8.214 MPa. The experimental shear tensile strength (average of three test samples) corresponding to these parameters (welding current of 6 kA, welding time of 25 cycles and electrode force 4.5 kN) was found to be 8.75 MPa. This shows that there is approximately 6.12 % error in the experimental and modeled results. Hence, the developed model can be effectively used in the process parameter range to predict the shear tensile strength of resistance spot welded joint.

## 4. Conclusions

The following conclusions can be drawn from analysis:

1. The resistance spot welding process was found to be successful to weld SAE 1010 steel sheets. In the range of resistance spot welding process parameters, macrographic view, micrographic view and microstructure of the welded joint showed proper fusion of base materials (SAE 1010 steel sheets) and very less amount of crack and porosity was observed.
2. Based on analysis of variance (ANOVA), welding current, welding time (cycle), and electrode force were found to be significant factors. Interactions of parameters were also found significant interactions. The response surface methodology was used effectively to model the shear tensile strength of resistance spot welded joint. Within the resistance spot welding process parameters range, the shear tensile strength of SAE 1010 steel sheets joint decreases with the increase

in welding current while shear tensile strength increases with the increase in welding time (cycle) and electrode force from minimum to maximum limit.

3. Within the resistance spot welding process parameters the optimum parameters for shear tensile strength was found to be lower welding current (6 kA), higher welding time (25 cycles), and higher electrode force (4.5 kN). The predicted value of shear tensile strength was found 8.214 MPa at 95% confidence interval. There is approximately 6.12 % error in the experimental and modeled results.

## References

- [1] B.H. Chang, Y. Zhou, "Numerical study on the effect of electrode force in small-scale resistance spot welding". *Journal of Materials Processing Technology*, Vol. 139, No. 3, 2003, 635-641.
- [2] Jiang Xu Jianhui, Zeng, Qiang Xiuping, "Optimization of resistance spot welding on the assembly of refractory alloy 50Mo-50Re thin sheet". *Journal of Nuclear Materials*, Vol. 366, No. 3, 2007, 417-425.
- [3] Zhao Zou Jiasheng, Zheng Chen Qizhang, "Surface modified long-life electrode for resistancespotwelding of Zn-coated steel". *Journal of Materials Processing Technology*, Vol. 8, 2009, 4141-4146.
- [4] Hongxin Shi, Ranfeng Qiu, Jinhong Zhu, "Effects of welding parameters on the characteristics of magnesium alloy joint welded by resistance spot welding with cover plates". *Materials & Design*, Vol. 31, No. 10, 2010, 4853-4857.
- [5] Ramin Hashemi, Hamed Pashazadeh, Mohsen Hamed, "An Incrementally Coupled Thermo-Electro-Mechanical Model for Resistance Spot Welding". *Materials and Manufacturing Processes*, Vol. 27, No. 12, 2012, 1442-1449.
- [6] Ranfeng Qiu, Hongxin Shi, Hua Yu, Keke Zhang, Yimin Tu, S Satonaka, "Effects of Electrode Force on the Characteristic of Magnesium Alloy Joint Welded by Resistance Spot Welding with Cover Plates". *Materials and Manufacturing Processes*, Vol. 25, No. 11, 2010, 1304-1308.
- [7] M. Pouranvari, S.M. Mousavizadeh, S.P.H. Marashi, "Influence of fusion zone size and failure mode on mechanical performance of dissimilar resistance spot welds of AISI 1008 low carbon steel and DP600 advanced high strength steel". *Materials & Design*, Vol. 32, No. 3, 2011, 1390-1398.
- [8] In Sung Hwang, Mun Jin Kang, Dong Cheol Kim, "Expulsion Reduction in Resistance Spot Welding by Controlling of welding Current Waveform". *Procedia Engineering*, Vol. 10, 2011, 2775- 2781.
- [9] R.S. Florea, K.N. Solanki, "Resistance spot welding of 6061-T6 aluminum: Failure loads and deformation". *Materials & Design*, Vol. 34, 2012, 624-630.
- [10] Hessamoddin Moshayedi, Iradj Sattari-Far, "Numerical and experimental study of nugget size growth in resistance spot welding of austenitic stainless steels". *Journal of Materials Processing Technology*, Vol. 212, No. 2, 2012, 347-354.
- [11] S. M. Darwish, S. D. Al-Dekhial, "The Response Surface Approach to Spot Welding Commercial Aluminum Sheets". *Materials and Manufacturing Processes*, Vol. 13, No. 2, 1998, 189-202.
- [12] G. Biilir Omer, "The relationship between the parameters C and n of Paris' law for fatigue crack growth in SAE 1010 steel". *Engineering Fracture Mechanics*, Vol. 36, No.2, 1990, 361-364.
- [13] M.T. Yu, D.L. Du Quesnay, T.H. Topper, "Deformation and fatigue behaviour of cold-rolled SAE 1010 steel". *International Journal of Fatigue*, Vol. 12, No. 5, 1990, 433-439.

- [14] Montgomery Douglas C, "Design and Analysis of Experiments". Wiley-India, 2007, 5<sup>th</sup> edition: 427.
- [15] V. Balasubramanian, A. K. Lakshminarayanan, R. Varahamoorthy, S. Babu, "Understanding the Parameters Controlling Plasma Transferred Arc Hardfacing Using Response Surface Methodology". *Materials and Manufacturing Processes*, Vol. 23, No. 7, 2008, 674-682.
- [16] T. Kim, H. Park, S Rhee, "Optimization of welding parameters for resistance spot welding of TRIP steel with response surface methodology". *International Journal of Production Research*, Vol. 43, No. 21, 2005, 4643-4657.
- [17] Dipayan Das, B. S. Butola, S. Renuka, "Optimization of Fiber-Water Dispersion Process Using Box-Behnken Design of Experiments Coupled with Response Surface Methodology of Analysis". *Journal of Dispersion Science and Technology*, Vol. 33, No. 8, 2012, 1116-1120.
- [18] S. P. Dwivedi, "Effect of process parameters on tensile strength of friction stir welding A356/C355 aluminium alloys joint". *Journal of Mechanical Science and Technology*, Vol. 28, No. 1, 2014, 285-291.
- [19] S. P. Dwivedi, S. Sharma, "Effect of Process Parameters on Tensile Strength of 1018 Mild Steel Joints Fabricated by Microwave Welding". *Metallogr. Microstruct. Anal.*, Vol. 3, 2014, 58-69.
- [20] S. P. Dwivedi, S. Sharma and R. K. Mishra, "Microstructure and mechanical behavior of A356/SiC/Fly-ash hybrid composites produced by electromagnetic stir casting" *J Braz. Soc. Mech. Sci. Eng.*, Vol. 37, 2015, 57-67.

# Estimation Bending Deflection in an Ionic Polymer Metal Composite (IPMC) Material using an Artificial Neural Network Model

Bahaa Kazem<sup>a\*</sup>, Jasim Khawwaf<sup>b</sup>

<sup>a</sup> *Mechatronics Engineering Dept., Baghdad University, IRAQ, Visiting Prof., UM-Columbia -USA.*

<sup>b</sup> *Mechatronics Engineering Dept., University of Kufa-IRAQ*

Received 30 April 2015

Accepted 15 April 2016

## Abstract

The IPMC bending characteristic depends on the accuracy of the manufacturing process for an IPMC specimen and the working conditions such as humidity, temperature, and applied electrical field. So, IPMC behavior is significantly nonlinear and uncertain.

In the present paper, we propose an accurate nonlinear neural Network Black-Box Model (NBBM) to predict the bending motion of IPMC taking into consideration the applied electrical voltage characteristics and the working conditions (specimen dimensions, temperature and humidity of working environment).

An experimental setup and testing program is used to test several IPMC specimens and measure the bending motion at different working conditions and applying electrical voltage signals. The NBBM for the IPMC is designed with suitable input and output parameters to estimate the IPMC specimen tip deflection. The Optimal Brain Surgeon (OBS) pruning algorithm is used to capture the optimal network size and to solve the overfitting problem among the training patterns.

Modeling results show that the optimized NBBM model can best describe the bending behavior of the IPMC specimen according to the applied electrical power signal and the working environment without using any measuring sensor and the proposed model can be used for modeling and controlling the IPMC bending motion in a single segment form.

© 2016 Jordan Journal of Mechanical and Industrial Engineering. All rights reserved

**Keywords:** IPMC, ANN and Bending.

## 1. Introduction

In the interest of finding advanced material for modern life, ionic polymer metal composite is an electro-active polymer that is gaining great importance as both a sensor and actuator. A typical Ionic Polymer Metal Composite (IPMC) sheet is a thin ionic polymer membrane (Nafion or Flemion) covered on both sides by two metallic layers (typically gold or platinum) to form two electrodes. When a low electrical field is applied, the transport of hydration cations within the IPMC and the associated electrostatic interactions lead to bending motions of the IPMC sheet toward the anode (+). The cations are initially bound to the anionic groups in the neutral state, forming clusters with the solvent molecules that can easily be exchanged with other cation forms [1].

IPMC has been receiving more and more attention, especially for micro-application. Because of the low driven voltage, flexible operation, large bending, and low weight, IPMC material has been widely applied in many micro-

applications such as snake robots, fish robots, walking robots, and micropumps [1-2].

The IPMC actuation systems exhibit significant nonlinearities and uncertainties. The nonlinearities are mainly caused by the IPMC characteristics during operation. The uncertainties can originate from the external working environment including perturbations and frequency dependent upon the complex elastic modulus  $E^*$  [3]. These problems cause challenges for modeling the IPMC actuators.

The IPMC characteristic variants depend largely on the working conditions which can lead to oscillations and instabilities in IPMC system performances, especially in applications that require high precision [4-5]. Therefore, it is very useful to investigate the IPMC behaviors for building and simulating an IPMC actuator before applying to practice [6-7].

There are several models available to describe tip displacement of an IPMC. For instance, Newbury and Leo [8] proposed a linear model with mechanical terms, mechanical impedance and inertia, and two electric terms, DC resistance and charge storage. The model was based on

\* Corresponding author e-mail: kazemb@missouri.edu.

an equivalent circuit representation that was related to the mechanical, electrical and electromechanical properties of the material. Expressions for the quasi-static and dynamic mechanical impedance were derived from beam theory. The electrical impedance was modeled as a series combination of resistive and capacitive elements. The resulting linear electromechanical model is based on the measurement of the effective permittivity, elastic modulus, and effective strain coefficient. All input-output relationships related to sensing and actuation can be derived using these three material parameters and the transducer geometry.

There are more lumped models available. In those models input parameters such as voltage or current are converted to the output parameters - tip displacement, force, and etc. For instance, Jung and Choi modeled an IPMC as a high pass filter, using series of resistors and capacitors in their calculations [9]. The model was an equivalent electrical circuit model for the IPMC actuator using experimental data.

Punning proposed a non-linear transmission line model, where all the elements of a transmission line had a physical meaning [10]. He showed that the IPMC model works as a delay line with changing resistors and the curvature of the IPMC sample at a given point depends on the surface resistance.

There are few Finite Element models for an IPMC available. Some authors, like Nasser *et al.* [11] and Wallmersperger *et al.* [12], have already simulated mass transfer and electrostatic effects, a similar approach is used in this work. Toi and Kang [13] proposed a Finite Element model, where viscosity terms in transportation processes were included explicitly. However, the basis of the described model was a rectangular beam with 2 pairs of electrodes. Instead of using continuum mechanical equations for simulating mechanical bending, analytical Euler beam theory is more commonly used by authors like Lee [14] and Wallmersperger [15].

Linear and nonlinear black-box models have been identified from experimental data for Ionic Polymer-Polymer Composite (IP2C) actuators had been developed by Graziani [16]. The models take into account the dependence of IP2C actuators behavior on environmental temperature and humidity as relevant modifying inputs.

In order to avoid difficult problems in control, a controller based Adaptive Neuro-Fuzzy Inference System (ANFIS) had been proposed by Thinh *et al.* [17]; it combines the merits of fuzzy logic and neural network, is used for tracking position of IPMC actuator. The results showed that ANFIS algorithm is reliable in controlling IPMC actuator. In addition, experimental results show that the ANFIS performed better than the Pure Fuzzy Controller (PFC). The results show that the proposed adaptive neuro-fuzzy controller can be successfully applied to the real-time control of the ionic polymer metal composite actuator for which the performance degrades under long-term actuation.

Nam & Ahn [18] developed a Nonlinear Black-Box Model (NBBM) for IPMC actuators based on a novel Preisach type fuzzy Nonlinear Auto Regressive Exogenous (NARX) model and modified Particle Swarm Optimization

(PSO). Firstly, an IPMC actuator is investigated. The open-loop input voltage signals are applied to the IPMC in order to investigate the IPMC characteristics. Secondly, a proper Preisach type fuzzy NARX model is developed with one input and one output to estimate the IPMC tip displacement. Modeling results proved the ability of proposed scheme to estimate the bending behaviors of IPMC actuators.

An accurate Nonlinear Black-Box Model (NBBM) for estimating the bending behavior of IPMC actuators had been proposed by Truong and Ahn [19]. The model is constructed via a General Multilayer Perceptron Neural Network (GMLPNN) integrated with a Smart Learning Mechanism (SLM) that is based on an extended Kalman filter with self-decoupling ability (SDEKF). Here the GMLPNN is built with an ability to auto-adjust its structure based on its characteristic vector. Furthermore, by using the SLM based on the SDEKF, the GMLPNN parameters are optimized with small computational effort, and the modeling accuracy is improved. The advanced NBBM model for the IPMC system is created with the proper inputs to estimate IPMC tip displacement. Then the model is optimized using the SLM mechanism with the training data.

A Nonlinear Black-Box Model (NBBM) for IPMC actuators with self-sensing behavior based on a Recurrent Multi-Layer Perceptron Neural Network (RMLPNN) and a Self-Adjustable Learning Mechanism (SALM) had been proposed by Truing *et al.* [20].

Firstly, an IPMC actuator is investigated. Driving voltage signals are applied to the IPMC in order to identify the IPMC characteristics. Secondly, the advanced NBBM for the IPMC is built with suitable inputs and output to estimate the IPMC tip displacement. Finally, the model parameters are optimized by the collected input/output training data.

Modeling results show that the proposed self-sensing methodology based on the optimized NBBM model can well describe the bending behavior of the IPMC actuator corresponding to its applied power without using any measuring sensor.

According to previous researches, understanding IPMC (and smart material in general) characterizations and solving relevant problems are quite difficult tasks because of their complex behavior, which sometimes cannot be identified without intelligent, numerical, and analytical approaches. Because of that, some prediction technique, like Artificial Neural Networks (ANN) can be utilized to solve these problems.

Also, the change in working conditions affects the IPMC characteristics, because it changes the Young modulus and ions density, hence, their mechanical response.

In this work we developed a Nonlinear Black-Box Model (NBBM) based on a Multi-Layer Perceptron Neural Network (MLPNN) to estimate the IPMC tip bending deflection, corresponding to input parameters (electrical voltage amplitude and frequency, temperature and humidity of environment, and dimensions of IPMC (length, and width)) without any measuring sensor.



**Table 2.** Data sets generated from IPMC specimen No. one

Pattern No.	Input Voltage (mv)	Frequency of Input(Hz)	Humidity of environment	Temperature of environment (C)	Length of IPMC (mm)	Width of IPMC (mm)	Deflection of IPMC (mm) (Tip displacement)
1	100	0.07	42	22	40	10	4.865
2	100	0.1	42	22	40	10	2.354
3	100	0.15	42	22	40	10	1.4705
4	100	0.25	42	22	40	10	1.4565
5	120	0.07	41	20	40	10	5.4411
6	120	0.1	41	20	40	10	3.088
7	120	0.15	41	20	40	10	1.9115
8	120	0.25	41	20	40	10	1.764
9	155	0.07	32	21	40	10	6.4705
10	155	0.1	32	21	40	10	3.821
11	155	0.15	32	21	40	10	2.352
12	155	0.25	32	21	40	10	2.2058
13	200	0.07	39	22	40	10	7.588
14	200	0.1	39	22	40	10	5.578
15	200	0.15	39	22	40	10	3.382
16	200	0.25	39	22	40	10	2.941
17	250	0.07	40	21	40	10	10.882
18	250	0.1	40	21	40	10	7.351
19	250	0.15	40	21	40	10	5.589
20	250	0.25	40	21	40	10	4.558

**Table 3.** Data sets generated from IPMC specimen No. two

Pattern No.	Input Voltage (mv)	Frequency of Input(Hz)	Humidity of environment	Temperature of environment (C)	Length of IPMC (mm)	Width of IPMC (mm)	Deflection of IPMC (mm) (Tip displacement)
1	100	0.07	38	22	30	5	2.94
2	100	0.1	38	22	30	5	1.465
3	100	0.15	38	22	30	5	.5605
4	100	0.25	38	22	30	5	.294
5	120	0.07	40	22	30	5	3.167
6	120	0.1	40	22	30	5	1.473
7	120	0.15	40	22	30	5	.9725
8	120	0.25	40	22	30	5	.441
9	155	0.07	36	21	30	5	3.821
10	155	0.1	36	21	30	5	2.2058
11	155	0.15	36	21	30	5	1.3945
12	155	0.25	36	21	30	5	.458
13	200	0.07	40	23	30	5	4.85
14	200	0.1	40	23	30	5	2.647
15	200	0.15	40	23	30	5	1.4708
16	200	0.25	40	23	30	5	.538
17	250	0.07	40	21	30	5	6.175
18	250	0.1	40	21	30	5	3.088
19	250	0.15	40	21	30	5	1.5961
20	250	0.25	40	21	30	5	1.029

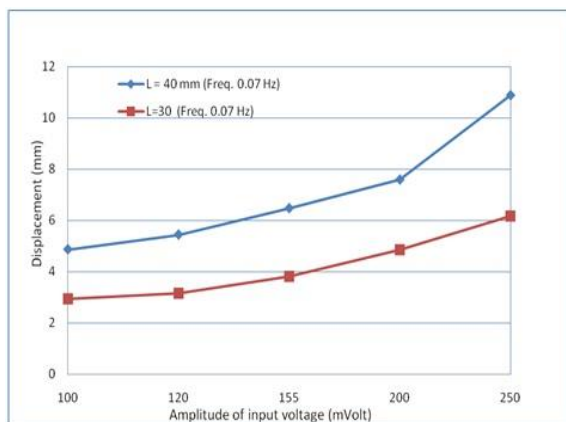


**Figure 3.** Maximum IPMC bending deflection with respect to the input voltage

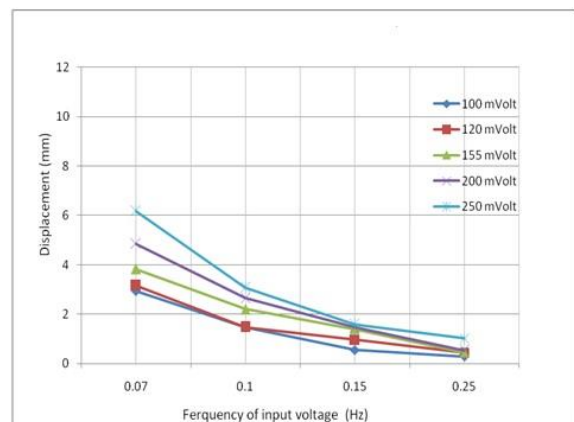


**Figure 4.** Maximum IPMC Tip Deflection change according to the change in applied Electrical Voltage Amplitude and Frequency for specimen of length 30 mm

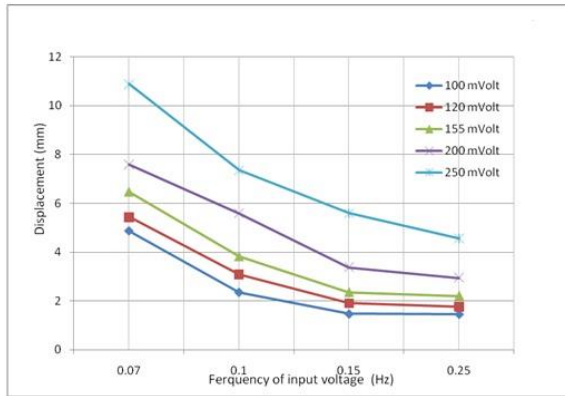


**Figure 5.** Maximum Tip Deflection change according to the change in applied Electrical Voltage Amplitude and Frequency for specimen of length 40 mm

#### 4. A Nonlinear Black-Box Model for IPMC Actuator (NBBM)

A neural network can be defined as a model of reasoning based on the human brain. The brain consists of a densely interconnected set of nerve cells, or basic information processing units, called neurons [23].

Neural networks are composed of simple elements operating in parallel. As in nature, the network function is determined largely by the connections between elements. You can train a neural network to perform a particular function by adjusting the values of the connections (weights) between elements. Commonly neural networks are adjusted, or trained, so that a particular input leads to a specific target output. Such a situation can be shown as follows: there, the network is adjusted, based on a comparison of the output and the target, until the network output matches the target. Typically many such input/target pairs are needed to train a network [24], [25].

One of the advantages of neural networks is its ability to model nonlinear problems those are hard to solve mathematically. Neural network can deal with any problems that can be represented as patterns.

Therefore, to solve the difficulty of IPMC modeling, we will use a nonlinear black-box model, which contain Multi-Layer Perceptron Neural Network (MLPNN) as a nonlinear model, is designed to model highly nonlinear systems in general and the IPMC actuator in particular.

A feed forward neural network distinguishes itself by the presence of one or more hidden layers, whose computation nodes are correspondingly called hidden neurons or hidden units, Figure 6. The function of hidden neurons is to intervene between the external input and the network output in some useful manner. By adding one or more hidden layers, the network is enabling to extract higher order statistics.

Multi-layer feed forward networks commonly referred as (MLP) are an important class of neural networks. MLPs have been applied successfully to solve some difficult and diverse problems in many disciplines of science and technology. The main method of training MLPs is the error back propagation, which was recognized several groups of scientists [26]–[30]

MLP is supervised network so it requires a desired response to be trained. With one or more hidden layers,

they can approximate virtually any input-output map. Figure 6 shows a typical network structure [20] which contains an input layer (on the left) with  $n$  neurons,  $k$  hidden layers (in the middle) of which the  $j^{\text{th}}$  layer contains  $q_j$  neurons, and an output layer (on the right) with  $m$  neurons. The input layer is represented by a vector of input variables  $(u_1, \dots, u_n)$ . The input layer distributes these values to each of the neurons in the first hidden layer. At each neuron in a hidden layer, the output values from its previous layer are multiplied by weights ( $w$ ), and the resulting weight values are added together, producing a combined value ( $sh_j$ ) as given at Equation 1:

$$sh_j = \sum_{i=1}^n w_{ij} u_i, \quad j = 1, \dots, q_1 \quad (1)$$

for each node in the 1st hidden layer

$$sh_l = \sum_{i=1}^{q_{l-1}} w_{ij} oh_i + w_{jo} oh_{l-1}, \quad j = 1, \dots, q_l$$

for each node in the  $l$ th hidden layer

where  $sh$  is the weighted sum, also there are a series of constants from  $b_0$  to  $b_k$ , which are called ‘bias’ factors, that are fed to the input layer and each of the hidden layers. The weighted sum ( $sh$ ) is then fed into a transfer function,  $F$ , to obtain the outputs a value of neuron  $j$ th ( $oh$ ). The outputs from the final hidden layer are distributed to the output layer.

At neuron,  $p^{\text{th}}$  in the output layer, output values from the final hidden layer neurons are multiplied by weights ( $W$ ) and added together to produce a combined value ( $sh$ ). This sum is fed into a transfer function,  $F$ , to compute the outputs value of neuron  $p^{\text{th}}$  ( $oh$ ). This value is then gained with a suitable factor to a corresponding output ( $y$ ). The values  $y$  are the outputs of the network.

For hidden as well as output units, sigmoid activation functions are usually preferable to threshold activation functions. Networks with threshold units are difficult to train because the error function is stepwise constant. In this work, we used the Levenberg-Marquardt training algorithm in addition to Gradient Descent with Momentum algorithm and Conjugate Gradient Descent algorithm. For sigmoid units, a small change in the weights usually produces a change in the outputs, which makes it possible to tell whether that change in the weights is good or bad. The designed MLPNN structure in this research is built with sigmoid activation functions given in equation 2.

Hence, the output of each hidden node can be computed using Equation 2:

$$oh_j = F(sh_j) = \frac{1}{1 + e^{-sh_j}} \quad (2)$$

From Equation 2, it is clear that the output  $oh$  closes to the boundaries 0 and 1. In the present study, we normalize the inputs in the range  $[-1, +1]$ . Each of the outputs in the output layer can be obtained as Equation 3:

$$\hat{y} = k_p \times oh_p \quad (3)$$

where  $k_p$  is a scaling gain corresponding to output  $p$ th selected from the output range.

$$\begin{cases} oh_p = F(sh_p) = \frac{1}{1 + e^{-sh_p}} & (4) \\ sh_p = \left( \sum_{j=1}^{qk} W_j oh_j + W_o b_k \right) \quad p = 1, \dots, m & (5) \end{cases}$$

The NBBM model possessed both the powerful universal approximating features from the MLPNN structure. Different structures of MLPNN related to training algorithm and hidden layers have been investigated in order to obtain the optimized neural network model for estimate the IPMC tip deflection.

It is well known that the model structure as well as the training algorithm is very important in the selection model of a neural network. Since there is a large number of training algorithms for feed forward neural network, one cannot easily decide which performs better for a specific application. Thus the neural network model was trained using three different training algorithms:

1. Gradient Descent with Momentum algorithm
2. Levenberg – Marquardt algorithm
3. Conjugate Gradient Descent algorithm

Also, we used two different activation functions in output layer:

1. Linear activation function
2. Log sigmoid activation function

The performances of these three training algorithms were tested using different types of activation functions and compared with each other to decide best algorithm that able to capture IPMC behavior. We randomly selected 80% of the total patterns to train the networks. Once a neural network has been trained successfully using MATLAB ®, it can perform the required mappings as a sort of black box. To check the ability of the network to deal with new patterns which are similar to learned patterns (generalization of the network), we used the remaining 10% of the patterns for validation and 10% for testing of the performance of the network.

Table 4 shows the correlation values for the results of the training, and testing results using different training algorithms and different activation functions after 1000 iterations. The selection of the best network will based on which hidden unit gives the lowest testing Error results. The network error (Train Error and Test Error) is calculated as the sum of the squared differences between the actual value (target value) and neural network output.

After examining the performance of different structures with different training algorithms, a network with more than 10 hidden neurons trained by Levenberg-Marquardt algorithm and log sigmoid activation function for output layer showed good performance indices as shown in Figure 7.

Despite many advances, for neural network to find general applicability in real world problems, the crucial question is to determine the most appropriate network size for solving a specific task. The network designer dilemma stems from the fact that both large and small networks exhibit a number of shortcomings. When the network has

too many degrees of freedom (network weights and biases), more local minima, instead of reaching global minima, in addition to the overfitting problem among training patterns makes the network fail to generalize its knowledge acquired during training phase. To solve the problem of choosing the optimal size network, an Optimal Brain Surgeon (OBS) pruning algorithm is used. The aim of an OBS pruning algorithm is to capture the optimal network size by gradually reducing (a large trained) network's degrees of freedom. The algorithm is based on the idea of iteratively removing a single degree of freedom (weight or bias) and then adjusting the remaining weight with a view to maintaining the original input – output behavior [31]-[33].

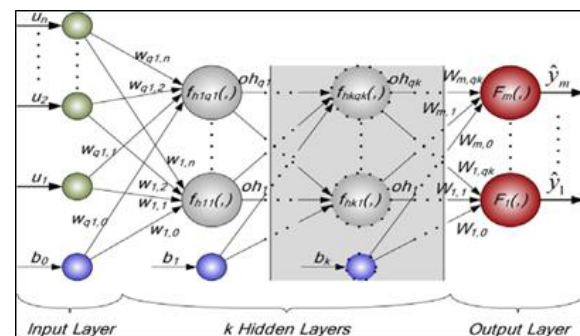


Figure 6. Structure of a Feed Forward MLPNN system [20]

## 5. Modeling Results

The major advantage of neural network predictions is that the model can estimate the IPMC tip deflection accurately once input variables (voltage, frequency, length and width of IPMC, and temperature and humidity of environment) are known.

The developed neural network model is used to estimate the IPMC tip deflection of the available training patterns which show a reasonable agreement between the target and the estimated values as illustrated in Figure 8. From this figure, it is clear that the optimized NBBM model can estimate the IPMC tip deflection with high precision and then be able to be applied to IPMC control system as a "virtual tip deflection sensor" for the self-sensing behavior.

The neural network model can give insight about the effect of each input variables (voltage, frequency, length and width of IPMC, temperature and humidity of environment) on the estimation of the IPMC tip displacement. The effect each of input variable is shown in Table 5. Thus, the temperature and humidity show very limited effect on the proposed NBBM model prediction and can be neglected in practical implementation of the model. The estimated results for the effectiveness of each working-variable on the IPMC tip displacement is highly depended on the working variables ranges and need to repeat the training for any new set of working variables and IPMC specimens.

**Table 4.** Correlation between training error and testing error for deferent neural networks training algorithm and activation function type

No. of hidden neurons	Correlation value					
	Gradient Descent activation function of output layer log sigmoid	Gradient Descent activation function of output layer linear	Levenberg – Marquardt Algorithm activation function of output layer log sigmoid	Levenberg – Marquardt Algorithm activation function of output layer linear	Conjugate Gradient Descent activation function of output layer log sigmoid	Conjugate Gradient Descent activation function of output layer linear
5	0.802599	0.994411	0.938098	0.788558	0.624325	0.962059
6	0.763727	0.744328	0.916023	0.940821	0.644214	0.986909
7	0.819456	0.751879	0.991105	0.489284	0.705154	0.632704
8	0.844334	0.709663	0.992142	0.959573	0.662197	0.613903
9	0.826479	0.725508	0.925715	0.676961	0.804905	0.609026
10	0.810121	0.710661	0.995163	0.85257	0.670168	0.622467
11	0.837673	0.703325	0.998624	0.934037	0.953935	0.648482
12	0.804059	0.665097	0.993454	0.999425	0.668997	0.999909
13	0.835637	0.658603	0.904077	0.994023	0.627829	0.705363
14	0.820606	0.658175	0.999982	0.999772	0.996477	0.582949
15	0.800279	0.724997	0.994709	0.961663	0.65892	0.619741

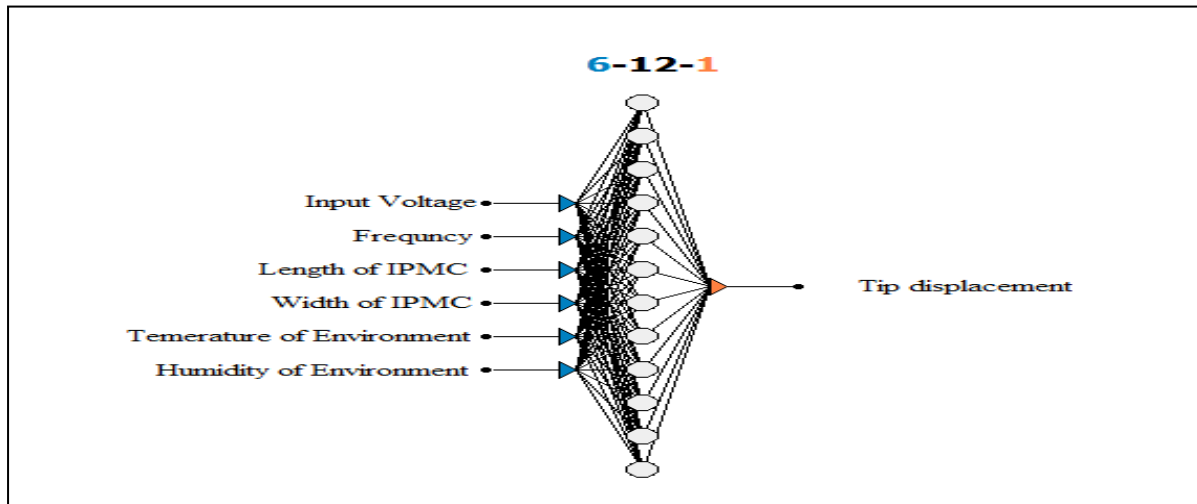


**Figure 7.** Optimized Neural Network Architecture for estimating the IPMC Tip Deflection

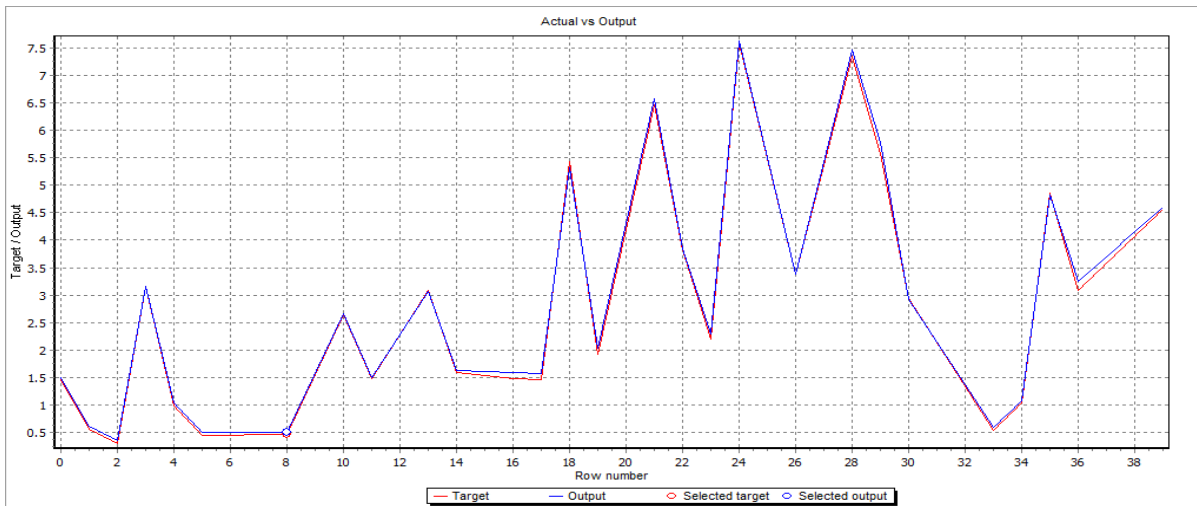


**Figure 8.** The IPMC Tip Deflection using the Proposed Neural Network Model

**Table 5.** The estimated effects of working-variables on IPMC tip displacement as they predicted by NBBM

working variable	Percentage effect on IPMC Displacement (%)
Voltage (mv)	24.577515
Frequency (Hz)	29.769568
Length of IPMC (mm)	18.294952
Width of IPMC (mm)	18.492071
Temperature of Environment (C°)	5.799173
Humidity of Environment (dry/ wet)	3.066722

## 6. Conclusions

In this work we presented a Nonlinear Black-Box Model (NBBM) to estimate IPMC deflection response, the model is based on the multi-layer perception neural network. The results show that the model can well describe the IPMC Tip deflection, corresponding to operation variables for IPMC actuator (Input voltage, frequency, dimensions of length of IPMC, temperature and humidity of environment).

After examining the performance of the suggested neural networks structures, a neural network with 12 hidden neurons trained by the Levenberg-Marquard algorithm, and using log sigmoid activation function, showed good performance indices.

The proposed NBBM model takes into account the dependence of IP2C actuators behavior on environmental temperature and humidity as relevant modifying inputs.

## References

- [1] M. Lopez, B. Kipling, and H. L. Yeager, "Ionic diffusion and selectivity of a cation exchange membrane in nonaqueous solvents," *Anal. Chem.*, Vol. 49 (1977) No. 4, 629–632.
- [2] K. J. Kim and S. Tadokoro, Eds., *Electroactive Polymers for Robotic Applications*. London: Springer London, 2007.
- [3] S. J. Lee, M. J. Han, S. J. Kim, J. Y. Jho, H. Y. Lee, and Y. H. Kim, "A new fabrication method for IPMC actuators and application to artificial fingers," *Smart Mater. Struct.*, Vol. 15 (2006) No. 5, 1217–1224.
- [4] C. Bonomo, P. Brunetto, L. Fortuna, P. Giannone, S. Graziani, and S. Strazzeri, "A Tactile Sensor for Biomedical Applications Based on IPMCs," *IEEE Sens. J.*, Vol. 8 (2008) No. 8, 1486–1493.
- [5] H. Jung and D.-G. Gweon, "Creep characteristics of piezoelectric actuators," *Rev. Sci. Instrum.*, Vol. 71 (2000) No. 4, 1896.
- [6] K. Tsiakmakis, J. Brufau, M. Puig-Vidal, and T. Laopoulos, "Modeling IPMC Actuators for Model Reference Motion Control", 2008 *IEEE Instrumentation and Measurement Technology Conference*, 2008, pp. 1168–1173.
- [7] Z. Chen, L. Hao, D. Xue, X. Xu, and Y. Liu, "Modeling and control with hysteresis and creep of ionic polymer-metal composite (IPMC) actuators", 2008 *Chinese Control and Decision Conference*, 2008, pp. 865–870.
- [8] K. M. NEWBURY and D. J. LEO, "Linear Electromechanical Model of Ionic Polymer Transducers -Part I: Model Development," *J. Intell. Mater. Syst. Struct.*, Vol. 14 (2003) No. 6, 333–342 2003.
- [9] K. Jung, J. Nam, and H. Choi, "Investigations on actuation characteristics of IPMC artificial muscle actuator," *Sensors Actuators A Phys.*, Vol. 107 (2003) No. 2, 183–192.
- [10] A. Punning, M. Kruusmaa, and A. Aabloo, "Surface resistance experiments with IPMC sensors and actuators," *Sensors Actuators A Phys.*, Vol. 133 (2007) No. 1, 200–209.
- [11] S. Nemat-Nasser and S. Zamani, "Modeling of electrochemomechanical response of ionic polymer-metal composites with various solvents," *J. Appl. Phys.*, Vol. 100 (2006) No. 6, 064310.
- [12] T. Wallmersperger, B. Kröplin, and R. W. Gülch, "Coupled chemo-electro-mechanical formulation for ionic polymer gels—numerical and experimental investigations," *Mech. Mater.*, Vol. 36 (2004) No. 5–6, 411–420.
- [13] Y. Toi and S.-S. Kang, "Finite element analysis of two-dimensional electrochemical-mechanical response of ionic conducting polymer-metal composite beams," *Comput. Struct.*, Vol. 83 (2005) No. 31–32, 2573–2583.
- [14] S. Lee, H. C. Park, and K. J. Kim, "Equivalent modeling for ionic polymer-metal composite actuators based on beam theories," *Smart Mater. Struct.*, Vol. 14 (2005) No. 6, 1363–1368.
- [15] T. Wallmersperger, D. J. Leo, and C. S. Kothera, "Transport modeling in ionomeric polymer transducers and its relationship to electromechanical coupling," *J. Appl. Phys.*, Vol. 101 (2007) No. 2, 024912.
- [16] S. Graziani, E. Umana, M. G. Xibilia, and V. De Luca, "Multi-input identification of IP2C actuators," in *2013 IEEE International Instrumentation and Measurement Technology Conference (I2MTC)*, 2013, 1147–1151.
- [17] N. T. Thinh, Y.-S. Yang, and I.-K. Oh, "Adaptive neuro-fuzzy control of ionic polymer metal composite actuators," *Smart Mater. Struct.*, Vol. 18 (2009) No. 6, 065016.
- [18] D. N. C. Nam and K. K. Ahn, "Identification of an ionic polymer metal composite actuator employing Preisach type fuzzy NARX model and Particle Swarm Optimization," *Sensors Actuators A Phys.*, Vol. 183 (2012), 105–114.
- [19] D. Q. Truong and K. K. Ahn, "Modeling of an ionic polymer metal composite actuator based on an extended Kalman filter trained neural network," *Smart Mater. Struct.*, Vol. 23 (2014) No. 7, 074008.
- [20] D. Q. Truong, K. K. Ahn, D. N. C. Nam, and J. Il Yoon, "Identification of a nonlinear black-box model for a self-sensing polymer metal composite actuator," *Smart Mater. Struct.*, Vol. 19 (2010) No. 8, 085015.
- [21] Y. Bar-Cohen, X. Bao, S. Sherrit, and S.-S. Lih, "Characterization of the electromechanical properties of ionomeric polymer-metal composite (IPMC)," in *SPIE's 9th Annual International Symposium on Smart Structures and Materials*, 2002, pp. 286–293.
- [22] B. C. Lavu, M. P. Schoen, and A. Mahajan, "Adaptive intelligent control of ionic polymer-metal composites," *Smart Mater. Struct.*, Vol. 14 (2005) No. 4, pp. 466–474.
- [23] M. Negnevitsky, *Artificial Intelligence: A Guide to Intelligent Systems*. 3rd Edition: Addison-Wesley 2011.
- [24] E. A. Metzbowler, J. J. DeLoach, S. H. Lalam, and H. K. D. H. Bhadeshia, "Secondary effects in neural network analysis of the mechanical properties of welding alloys for HSLA shipbuilding steels," *Math. Model. Weld Phenomena 6, eds, Cerjak and K. D. H. Bhadeshia, London*, p. 231–242, 2002.
- [25] D. M. Eugene Charniak. *Introduction to Artificial Intelligence*. Addison-Wesley Series in Computer Science; 1985.
- [26] C. Vana, Vital Rao; Ratnamb, "Estimation of Defect Severity in Rolling Element Bearings using Vibration Signals with Artificial Neural Network," *Jordan Journal of Mechanical and Industrial Engineering*, Vol. 9 (2015) No.2, 113-120.

- [27] B. I. Kazem, N. F.H. Zangana, "A Neural Network Based Real Time Controller for Turning Process," *Jordan Journal of Mechanical and Industrial Engineering*, Vol. 1 (2007) No. 1, 43-55..
- [28] N. Ashhab, M; Talatb, "Modeling of the MEMS Reactive Ion Etching Process Using Neural Networks," *Jordan Journal of Mechanical and Industrial Engineering*, Vol. 5 (2011) No. 4, 353 - 357.
- [29] B. I. Kazem, YK Yousif, KM Daws, "Prediction of Friction Stir Welding Characteristic Using Neural Network," *Jordan Journal of Mechanical and Industrial Engineering*, Vol. 2 (2008) No. 3, 151-155.
- [30] B. I. Kazem, N. H. Ghaib, and N. M. H. Grama, "Experimental Investigation and Neural Network Modeling for Force System of Retraction T-Spring for Orthodontic Treatment," *J. Med. Device.*, Vol. 4 (2010) No. 2,021001.
- [31] M. Hintz-Madsen, L. Kai Hansen, J. Larsen, M. With Pedersen, and M. Larsen, "Neural classifier construction using regularization, pruning and test error estimation," *Neural Networks*, Vol. 11 (1998) No. 9, 1659–1670.
- [32] G. Castellano, A. M. Fanelli, and M. Pelillo, "An iterative pruning algorithm for feedforward neural networks.," *IEEE Trans. Neural Netw.*, Vol. 8 (1997) No. 3, 519–31.
- [33] B. I. Kazem, Ali Khudhair Mutlag, "Optimal Brain Surgeon Pruning of Neural Network Models of Manufacturing Processes" , *Journal of Engineering*, Vol. 11 (2005) No. 3, 495-508.



# Conceptual Design of Congregational Prayer Chair

Farouk Daghistani \*

*Faculty of Environmental Design, King Abdulaziz University, Jeddah, Saudi Arabia P.O. Box 80210. Jeddah 21589.*

*Received 19 August 2015*

*Accepted 28 February 2016*

## Abstract

Sit-to-stand is regarded as one of the most mechanically demanding daily tasks. Because of body weakness or disability of some Muslims, they cannot assume all the required physical motions of prayers without relying on a conventional chair. However, using a conventional chair when praying in mosques may lead to two main problems: (1) Disturbing the worshipers in the row behind the chair and/or (2) causing the user of the chair to be misaligned with the row of prayer. In the present paper, a novel conceptual design for a congregational prayer chair that alleviates such disturbances and misalignment problems is addressed. First of all, the existing causes and patterns of using conventional chairs while praying in mosques are outlined. Secondly, design criteria for congregational prayer chairs are established. After that, a novel conceptual design for a congregational prayer chair is explained. The obtained results identified 15 existing causes and 18 patterns of using chairs while praying and 2 patterns of chair placement in the row of prayer. In addition, the results show that the most praying position chairs are used for prostration. This study reveals a key feature concept considered in the conceptual design of the chair to solve the aforementioned problems through constructing a predetermined moving seat pan and a seat back so that the user can attain whatever praying positions without changing the placement of the chair.

© 2016 Jordan Journal of Mechanical and Industrial Engineering. All rights reserved

**Keywords:** *Chair, Design, Disability, Congregational prayer, Muslim.*

## 1. Introduction

Sit-to-stand is regarded as one of the most mechanically demanding daily tasks [1]. Unfortunately, difficulty with sit-to-stand motion is common especially among old people [2]. Today, there are different sit-to-stand devices that assist those people. Such devices are available commercially and include active supports (such as lift chairs, lift cushions and powered standing devices) and passive supports (such as grab bars and standing frames that assist stability when users rise) [3]. Despite the range of the various sit-to-stand devices, it is unclear which types of such devices are the most appropriate for persons who are in need for partial assistance [4]. In the particular case of Muslims, some people may need a suitable sit-to-stand device that assists them physically to perform the daily prayers.

Indeed, Muslims are required to pray five times a day. They have to attain a particular set of body positions while performing their prayers. These positions consist of standing, bowing, prostrating, and sitting on the ground or floor for relatively long and short periods of time (Figure 1). They must be tranquil during every position, as tranquillity is one of the pillars necessary for the validation of the prayer [5]. Few seconds of stillness in each prayer's

position are enough to achieve tranquillity [6]. Muslims, especially males, are encouraged to perform obligatory prayers congregationally because the reward is much greater than praying individually. Therefore, millions of worshipers around the world perform such prayers in mosques where the congregation is led by a person (Imam) and the remaining people stand behind him. The congregational prayer requires arranging worshipers' rows in a compact, straight and parallel manner with no gaps in the rows (Figure 2). Unfortunately, because of the age, illness, pregnancy, weakness or disabilities, or other temporary or permanent physical illness, many worshipers cannot assume all the required body positions. Hence, they may rely on a support structure (usually a conventional chair) for sitting while making gestures for the praying positions they cannot perform.

However, using conventional chairs while performing congregational prayer in mosques have at least two main disadvantages: First, the chair may disturb the worshipers in the row behind. Second, the chair user may be misaligned with the row of worshipers. Therefore, a large number of Muslim worshipers around the world would welcome a chair designed to alleviate the disturbance and misalignment problems caused by using conventional chairs. This kind of chair will provide an efficient support to attain all of the required prayer positions while praying in congregation in mosques.

\* Corresponding author e-mail fdaghistani@kau.edu.sa.

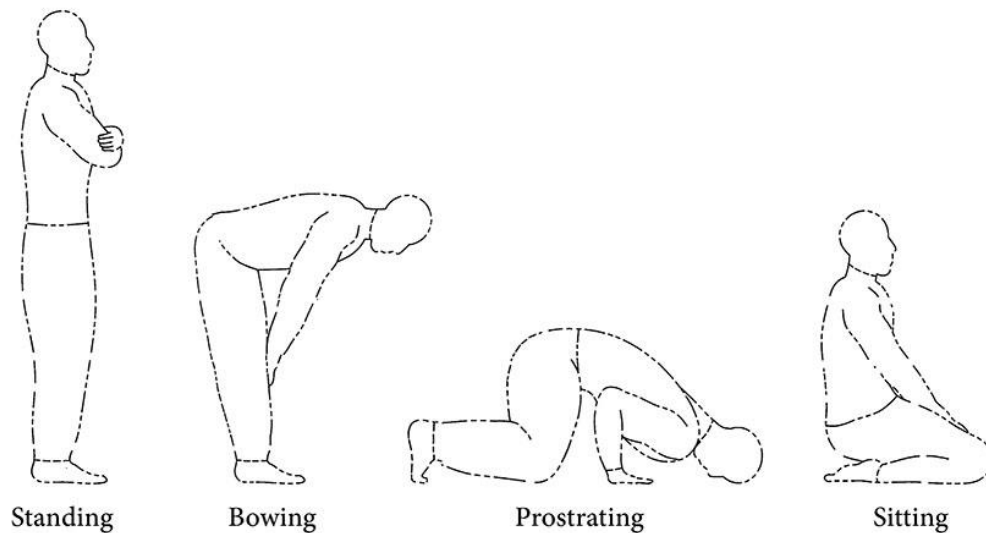


Figure 1. Body positions of praying.



Figure 2. Rows of worshippers in a mosque during a congregational prayer.

Ergonomics (or comfortable and functional design) is the scientific discipline and practice concerned with designing products that reduce fatigue and discomfort. Ergonomics takes proper account of the interaction between products and people who use them. In our case, the design optimization of a chair considers a number of factors including the shape, the width, the height of the seat pan and the backrest, the seat cushioning, etc. All these parts have the potential to influence comfort/discomfort of the seat users [7]. Low levels of seating comfort often lead to musculoskeletal complaints such as Low Back Pain (LBP) [8]. It is important to mention that many researchers revealed that setting for long time by itself doesn't increase the risk of LBP [9, 10, 11]. Therefore, it is essential to have a seat back that minimizes the spinal loading and relax the back muscles of the user. Such minimization and relaxation can be best achieved with a backrest inclined backwards [12, 13]. Chaffin *et al.* found that the stress on the spinal discs can be reduced approximately 40% by reclining the chair 20° degrees [14]. The seat back should be high enough to reach the shoulder blades and wide enough to support the waist breadth [15]. Another factor that enhances ergonomic seating is the inclusion of armrests. Nemoto and Ogawa found that the amounts of body flexion, hip

moment, knee moment are all reduced when using armrests during standing up [16]. Armrests also support the upper body and so reduce spinal loading [17].

Cushioning and the seat pan design are important for comfort/discomfort when sitting for a long duration, as they affect the pressure distribution at the seat-to-user interface. Seats with firm cushions may be regarded as "sporty" while seats with soft cushions may be viewed as more "luxurious" [18].

Ergonomic seating incorporates also a range of adjustability, with controls that are easily to use especially when the chairs are shared among different people [19]. Lastly, and more comprehensively, ergonomic seating considers all of the activities the chair is designed to support (i.e., task seating) [20].

The relevant Islamic regulations in praying with the support of chairs were detailed by Muslim scholars. Here is a brief summary of the most important regulations:

- The worshiper who cannot stand when praying may pray sitting-down [21].
- Whatever the worshiper is able to perform, he/she is obliged to do so, and whatever he/she is unable to perform, is waived for him/her. For example if a worshiper is excused from standing, his/her excuse does not allow him/her to sit on the chair to bow and prostrate. Also, if he/she is exempted from bowing and prostrating, that excuse does not allow him/her not to stand and to sit on the chair instead [22].
- With regard to the placement of the chair in the row:
  1. The one who prays sitting down from the beginning of the prayer until the end should have his posterior in line with the row because it is the place in which the body settles [23]. In this case, the rear legs of the chair must be aligned with the row (Figure 4-b).
  2. The one who prays standing and sitting should level with the row when standing because what matters is the standing position [22]. In this case, the front legs of the chair must be aligned with the row (Figure 4-a).
  3. When the front legs of the chair are aligned with the row, the chair will be behind the row, so it should be

placed in a manner that doesn't disturb the worshipers in the row behind, [22].

Based on the literature review of ergonomic seating, Islamic regulations mentioned above and the findings of a survey carried out by the author, this study aims to establish design criteria for a congregational prayer chair that solves the aforementioned problems. In addition, a proposed design for such a chair is presented.

## 2. Methods

A three-step procedure was used to achieve designing a new congregational chair that solves the aforementioned problems: (1) Defining the existing causes and patterns of using chairs while praying in mosques, (2) establishing design criteria for the congregational prayer chair, and (3) designing a prototype of the congregational prayer chair.

In the first step, the author observed chairs usage in mosques and conducted a short survey of 124 subjects (75 males and 49 females) who use chairs when praying or have used them when praying at least once in the past. The subjects' ages ranged from 18 to 95, with a mean age of 56.4 and a standard deviation of 17.8. The majority of the subjects (81.5%) were 41 years old and older (Figure 3). They were approached mostly at mosques by university students. The subjects were participated on a voluntary and not purely on a random basis.

The main purposes of this survey were to define the various causes of using chairs while praying in mosques and how the chairs were used. As the targeted population of this study is Muslims who use chairs when praying regardless of their ethnicities, and since it is impossible to design a chair that precisely fits the specific body shapes of all of them, the main challenge is to design a visually appealing and comfortable chair that suits the body dimensions of most users and can be adjusted to their specific needs [24, 25]. Therefore, anthropometric data related to the design of chairs which was collected in a study by M. AI-Haboubi have been relied on [26]. In the present study, 19 body dimensions of 408 subjects from 20 different nationalities were measured.

In the second step, the design criteria for the new congregational chair are laid-out based on the outcomes of the first step and relevant literature review.

In the third step, a prototype of the new congregational prayer's chair was developed based on the design criteria that came from the previous steps.

## 3. Results and Discussions

### 3.1. Existing Causes and Patterns of Using Chairs While Praying

Findings of the survey revealed 15 causes for using chairs while praying. Knee problems, aging and back problems were the three most common reasons and accounted for 50.8%, 42.7% and 35.5% of all cases, respectively. Pregnancy, foot problems, disability and extra weight were other less common causes with 5.6%, 4.8% and 4.0% of all causes, respectively. Other rarely mentioned causes accounted collectively for 12.1% include pelvis problems, heel problems, joints problems, accidents, varicose, sciatica, cirrhosis and surgeries (Table1).

**Table 1.** Causes of using chairs while praying.

Causes	No. of cases	Percent of Cases
<b>Knee problems</b>	63	50.8%
<b>Aging</b>	53	42.7%
<b>Back problems</b>	44	35.5%
<b>Pregnancy</b>	7	5.6%
<b>Foot problems</b>	6	4.8%
<b>Disability</b>	5	4.0%
<b>Extra weight</b>	4	3.2%
<b>Other</b>	15	12.1%

The results also identified 18 patterns of using chairs while praying, based on the various combinations of the five praying positions performed with the use of chairs (Table 2). The most repeated pattern is when the worshiper performs all of the praying positions while sitting down on the chair and gesturing. Such pattern is adopted by 29.8% of the study subjects. The second most repeated pattern is performing prostration, short sitting and long sitting praying positions with the support of chairs. Such pattern is adopted by 22.6% of the study subjects. The third most repeated pattern is performing bowing, prostrating, short sitting and long sitting positions with the support of chairs. Such pattern is adopted by 11.3% of the study subjects (Table 2).

Also, this survey revealed that prostration is the most praying position that the users of the chairs make gesture to, and that standing position is the least (Table 3)

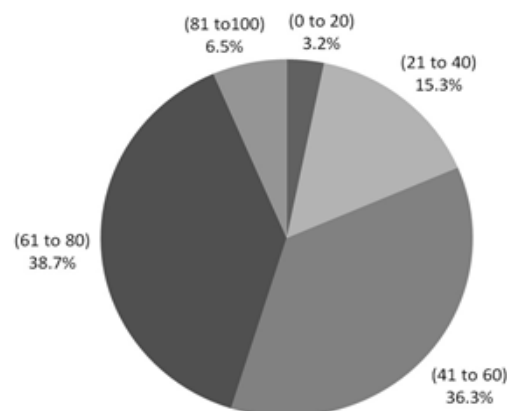


**Figure 3.** Percentage of the subjects in each age group of the study sample.

**Table 2.** The 18 patterns of using chairs, based on the various combinations of praying position(s) where chairs are used.

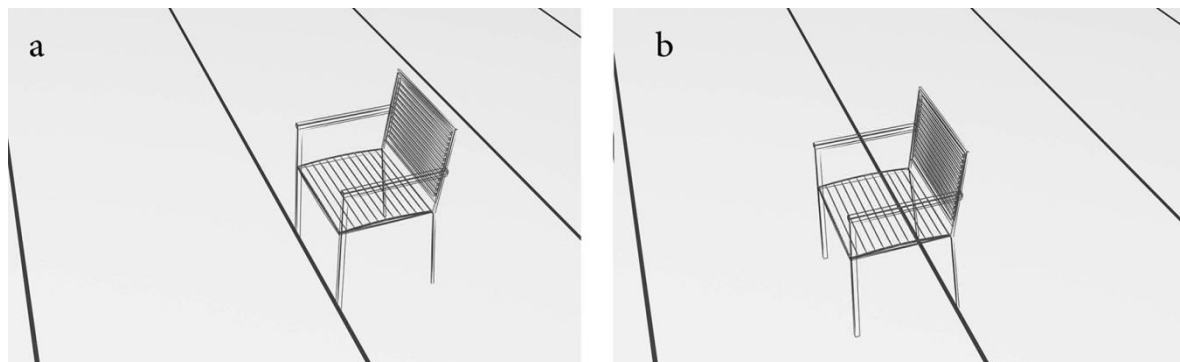
Pattern	No. of cases	Percent	Standing	Bowing	Prostrating	Short sitting	Long sitting
1	37	29.8%	x	x	x	x	x
2	28	22.6%			x	x	x
3	14	11.3%		x	x	x	x
4	8	6.5%		x	x		
5	6	4.8%				x	x
6	6	4.8%			x		
7	4	3.2%	x	x	x		
8	3	2.4%	x	x			
9	3	2.4%		x			
10	2	1.6%	x		x	x	x
11	2	1.6%	x		x	x	
12	2	1.6%	x	x			x
13	2	1.6%	x				x
14	2	1.6%			x		x
15	2	1.6%	x				
16	1	0.8%	x	x	x	x	
17	1	0.8%	x		x		x
18	1	0.8%	x		x		

**Table 3.** Frequency of prayer positions where chairs were used by the study sample.

Causes	No. of cases	Percent of Cases
<b>Knee problems</b>	63	50.8%
<b>Aging</b>	53	42.7%
<b>Back problems</b>	44	35.5%
<b>Pregnancy</b>	7	5.6%
<b>Foot problems</b>	6	4.8%
<b>Disability</b>	5	4.0%
<b>Extra weight</b>	4	3.2%
<b>Other</b>	15	12.1%

Findings of the survey also identified 2 patterns of chair placement in the row of prayer wherein either the front legs of the chair or the rear legs are aligned with the row (Figure 4). Unfortunately, both positions have disadvantages. On the one hand, when the front legs of the chair are aligned with the row, the chair may disturb the worshipers in the row behind the chair. On the other hand, when the rear legs are aligned with the row, the chair user may be misaligned with the row in some of the prayer positions such as the standing position.

Finally, based on observing people when praying, the researcher noted that when the worshiper bows, his body moves horizontally backward (approximately 18-22cm) in order to balance his body (Figure 5). Such observation has to be considered when designing the seat back of the congregational chair as explained later in this paper.

**Figure 4.** Chair placements: (a) front legs of the chair are aligned with the row and (b) rear legs of the chair are aligned with the row.

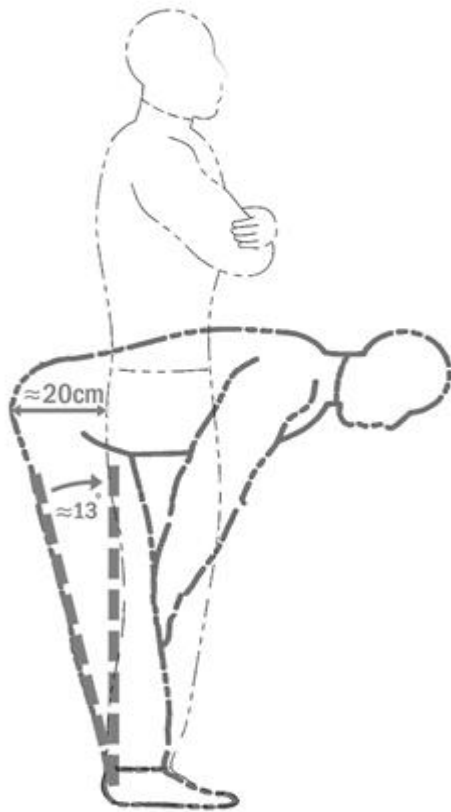


**Figure 5.** Approximate horizontal and angular measurement differences between standing and bowing positions.

### 3.2. Design Criteria for the Congregational Prayer Chair

Based on the literature review and the findings mentioned earlier, the following five basic design criteria for the novel chair of congregational prayers were established:

- It must allow the user to perform any praying position (as in Figure 1) when he/she can, without moving the chair from its place.
- It must allow the user to be aligned with the row when performing any praying position.
- It must avoid disturbing the worshipers in the row behind.
- It must provide stable support for the body.
- It should be comfortable to sit on for a long period of time.

### 3.3. Prototype of the Congregational Prayer Chair

The congregational prayer chair (Figure 6) is constructed with a seat and a seat back supported between two connecting arms. The connecting arms are mounted on chair legs. Grooves and tracks are provided on the arms that permit the seat and the seat back to be moved in a predetermined manner. Accordingly, the chair would permit a worshiper to attain, when he/she can, the five prayer positions (or any selected one of them) without changing the placement of the chair legs. Thus, the chair user will not disturb the alignment of the row and not disturb the worshipers in the row behind the chair.

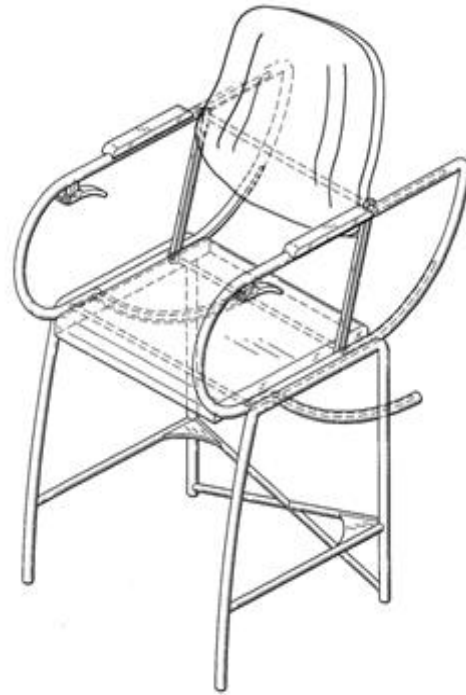


**Figure 6.** The prototype of the proposed congregational prayer chair.

The congregational prayer chair comprises a pair of U-shaped leg members that form spaced-apart front and rear legs. A pair of support bars spans the distance between and connects the front legs to the rear legs. Support bars that crisscross diagonally in X-shaped fashion connect the rear legs to each other. The support bars function to add rigidity and stability to the chair. Respective arm supports are attached to the inner surface of each respective U-shaped leg member. Each arm support is fashioned with a respective curved rear portion for reasons to be explained below. Respective straight portions extend from each curved rear portion to respective front curved portions to define the arm supports. Cushioning pads are mounted on the upper surfaces of the respective support arms. The support arms have inner surfaces that are provided with grooves or tracks therein, forming upper tracks and lower tracks. Additional track members extend angularly and rearward from the arm supports.

A seat member and a seat back are disposed between the arm supports. The seat member has front pins and rear pins attached at each side thereof. The front pins are engaged in lower curved track members for sliding movement therein. The rear pins are engaged in the back curved track for sliding movement therein. The seat back is provided with a pin extending from each side thereof for respective engagement in the upper tracks. A respective connecting arm extends between the seat back and the seat member on each side of the chair. A slot is provided along the length of each connecting arm. At its upper end, each connecting arm is interposed between the seat back and the respective curved portions of the support arms and is mounted for pivotal movement on pins. At its lower end, each of the respective connecting arms is interposed between the seat member and the curved portion of the support arms. Each rear seat pin is mounted for sliding movement in each corresponding slot.

As shown in Figure 7, the seat member and the seat back can assume one of two positions, a forward position (shown in phantom lines) and a rearward position (shown in solid lines). The rearward position is the default position due to a loaded internal-tube tension spring. The forward position can be achieved by pushing down the seat pan until it is locked by a conventional locking mechanism. In such position, the mentioned above tension spring will be further loaded. The locking mechanism consists of spring loaded pins extending from the lower portion of the two arm supports for respective engagement in the seat pan. Handles interact with the locking mechanism to release the seat and seat back for movement to the default position, when desired. In the forward position, the chair functions as a conventional chair and may be employed in this position by worshipers whose age and/or disabilities require the use of a conventional chair. In the rearward position, the seat and the seat back are moved rearward, and the seat swings down to provide open space (approximately 60-70 cm) between the arm supports. The rearward position allows the worshipers who are physically able to attain any of the prayer's position to do so without moving the legs of the chair, thus retaining the alignment of the rows and keeping the worshipers in the row behind the chair not disturbed (Figure 8).

Finally, it is important to mention that if the person who is performing prayer wants to change from the standing position to the sitting position, he or she needs to move forward to allow the seat pan to move to the forward position and vice versa. Such movement might be difficult or impossible to attain by some worshipers due to, for example, illness or not being able to keep their

equilibrium. Using armrests during standing up and sitting down may be helpful for most, but not all, users.

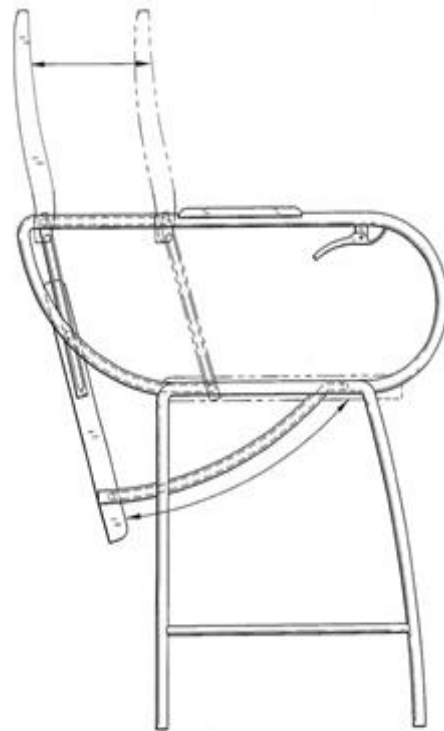


**Figure 7.** The forward and the rearward positions of the congregational prayer chair.

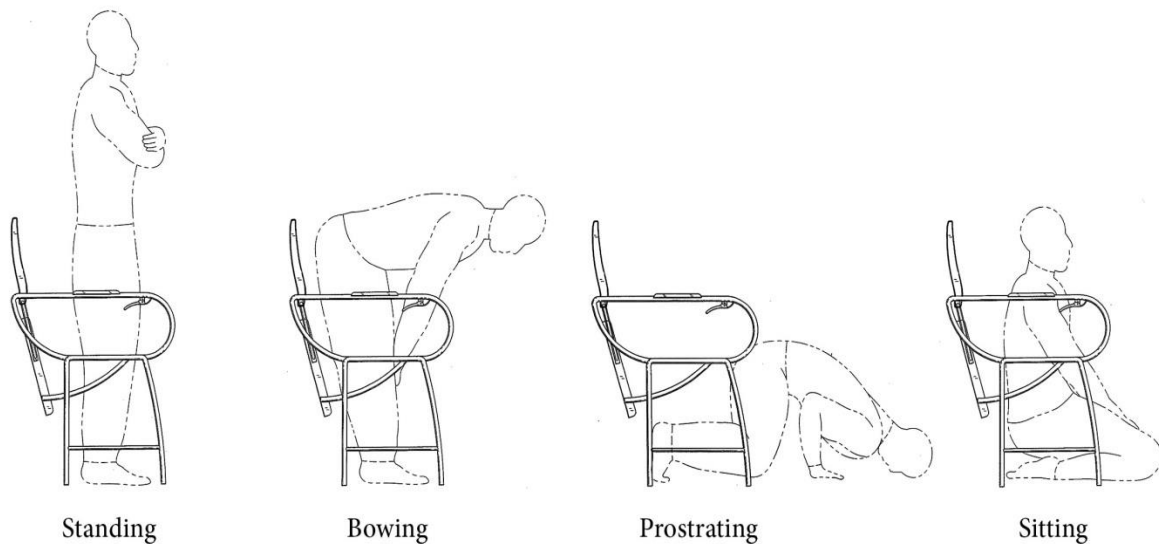


**Figure 8.** The rearward position of the congregational prayer chair allows worshipers to attain all or selected prayer positions whenever they can.

#### 4. Conclusion

In the present paper, a novel conceptual design for a congregational prayer chair is addressed. Such a chair is specially designed to provide needed support for certain worshipers participating in congregational Muslim prayers. Currently, such worshipers rely on conventional chairs for assistance in attaining the prayer positions that they cannot assume. Unfortunately, using such conventional chairs cause disturbance to the worshipers in the row behind the chairs or/and cause misalignment to their users with the rows of prayer. Such problems are well known to all Muslims who pray in the mosques because they occur repeatedly in almost mosques around the world. Also, many Muslim scholars have discussed the Islamic regulations of praying with the support of chairs. They have mentioned the importance of the alignment of the chair's user with the row of prayer and, in the same time, the importance of not causing disturbance to the worshipers in the row behind the chair. However, such two conditions are impossible to be met at the same time when using conventional chairs. Therefore, the challenge of this study was to design a chair that specifically solves the aforementioned problems and in the same time considers ergonomics principles. Based on the literature review and the findings of a survey carried out in this study, five basic design criteria for the novel chair of the congregational prayer were established. Based on those criteria, a prototype of such a chair was developed. The congregational prayer chair is constructed with a seat and a seat-back supported between two connecting arms. The connecting arms are mounted on chair legs. Grooves and tracks are provided on the arms that permit the seat and the seat-back to be moved in a predetermined manner so that a worshiper can attain the required prayer positions without disturbing the alignment of the prayer rows and the other worshipers in the row behind. It is expected, God willing, that Muslim worshipers around the world would welcome this chair that is designed to alleviate the misalignment problems and still provide adequate support to attain all of the required prayer positions

#### 5. Acknowledgement

The author acknowledges the financial and administrative support provided by King Abdulaziz University, Jeddah, Saudi Arabia.

#### Note

The author of this paper was awarded a patent from the United States Patent and Trademark Office for his "Congregational Prayer Chair". The patent number: (US 8,973,996 B2). The patent date: (March 10, 2015).

#### References

- [1] P.O. Riley, M.L. Schenkman, R.W. Mann, W.A. Hodge, "Mechanics of a constrained chair-rise". *Journal of Biomechanics*, Vol. 24 (1991) No. 1, 77-85.
- [2] Leon J, Lair T. Functional status of the noninstitutionalized elderly: estimates of ADL and IADL difficulties. Rockville (MD): US Department of Health and Human Services, Public Health Service, Agency for Health Care Policy and Research; 1990.
- [3] Technology for Long Term Care, "Standing assist devices". Kirtland (OH): Polisher Research Institute and IDEAS Institute; 2015. Available at: <http://www.techforltc.org/producttype.aspx?id=2057,1892>
- [4] J. Jeyasurya, H. F. Machiel Van der Loos, A. Hodgson, E. A. Croft, "Comparison of seat, waist, and arm sit-to-stand assistance modalities in elderly population". *Journal of Rehabilitation Research and Development*, Vol. 50 (2013) No. 6, 835-44.
- [5] IslamicBasics, "The salah has conditions, pillars, and waajibaat". Canada: 2007. Available at: <https://islamicbasics.wordpress.com/2007/10/21/the-salah-has-conditions-pillars-and-waajibaat/Alukah>, "Alrukn Alsadis min arkan alsalah... Altuma'aninah fi alruku'a". (in Arabic), Saudi Arabia: a website supervised by Al-Humaid, S and Al-Juraisi, K; 2015. Available at: <http://www.alukah.net/sharia/0/68327/>
- [7] G.F. Beard, M.J. Griffin, "Discomfort of seated persons exposed to low frequency lateral and roll oscillation: Effect of seat cushion". *Applied Ergonomics*, Vol. 45 (2014) No. 6, 1547-1557.
- [8] P. Vink, and S. Hallbeck, "Editorial: comfort and discomfort studies demonstrate the need for a new model". *Applied Ergonomics*, Vol. 43 (2012) No. 2, 271-276.
- [9] A.M. Lis, K.M. Black, H. Korn, M. Nordin, "Association between sitting and occupational LBP. *European Spine Journal*, Vol. 16 (2007) No. 2, 283-298.
- [10] D.M. Roffey, E.K. Wai, P. Bishop, B.K. Kwon, S. Dagenais, "Causal assessment of occupational sitting and low back pain: results of a systematic review". *The Spine Journal*, Vol. 10 (2010) No. 3, 252-261.
- [11] B.K. Kwon, D.M. Roffey, P.B. Bishop, S. Dagenais, E.K. Wai, "Systematic review: occupational physical activity and low back pain". *Occupational Medicine (Lond)*, Vol. 61 (2011) No. 8, 541-548.
- [12] Adams. M. A., "Wie beeinflusst die Sitpositionen die Lastverteilung in der Bandscheibe und ihre Ernährung?" In: Wilke, H. J. editor. *Ergomechanics 2*. Aachen: Shaker Verlag; 2006, p. 46-63.
- [13] L. Groenesteijn, P. Vink, M. de Looze, F. Krause, "Effects of differences in office chair controls, seat and backrest angle design in relation to tasks". *Applied Ergonomics*, Vol. 40 (2009) No. 3, 362-370.
- [14] Chaffin D, Andersson G, Martin BJ. *Occupational Biomechanics*. 4th ed. New York: John Wiley & Sons; 2006.
- [15] Allsteel SO, Allsteel ET. *Ergonomics and Design A Reference Guide*. Muscatine (IO): Allsteel Incorporation; 2006.
- [16] K. Nemoto, K. Ogawa, "On the effectiveness of armrests for the standing up motion". *Japanese Journal of Ergonomics*, Vol. 42 (2006) No. 1, 1-8.
- [17] M. Dreischarf, G. Bergmann, H. J. Wilke, A. Rohlmann, "Different arm positions and the shape of the thoracic spine can explain contradictory results in the literature about spinal loads for sitting and standing". *Spine (Phila Pa 1976)*, Vol. 35 (2010) No. 22, 2015-2021.
- [18] I. Kamp, "The influence of car-seat design on its character experience". *Applied Ergonomics*, Vol. 43 (2012) No. 2, 329-335.
- [19] Haworth. *The ergonomic seating guide handbook*. USA: Haworth; 2008.
- [20] Springer, T. *The future of ergonomic office seating*. USA: Knoll, Incorporation; 2010.
- [21] [21] Ibn Qudamah A. Al-Mughni. 8th ed. Al-Turki A, Al-Hilo A, editors, (in Arabic), Cairo: Hajr Press; 2013.
- [22] Islam Question and Answer, "Rulings and issues about praying on a chair". Saudi Arabia: a website supervised by

- Al-Munajjid, M; 2015. Available at: <http://islamqa.info/en/50684>
- [23] Al-Ansari ZM. Asna al-matalib fi sharh rawd al-talib. (in Arabic), Beirut: Dar al-Kutub al-ilmiah; 2001.
- [24] M. Graf, U. Guggenbuhl, H. Krueger, "An assessment of seated activity and postures at five workplaces". International Journal of Industrial Ergonomics, Vol. 15 (1995) No. 2, 81-90.
- [25] Hedge, A, Breeuwsma, K. Chair design beyond gender and age. Toronto (ON): Interior Designers of Canada; 2008.
- [26] M. H. Al-Haboubi, "Anthropometry for a mix of different populations". Applied Ergonomics, Vol. 23 (1992) No. 3, 191-196.

# Preparation and Corrosion Behavior of Bronze -40%w Composite

Malek Ali <sup>a\*</sup>, Balakumeren Suppiah<sup>b</sup>, Zaid Muayaduldeen<sup>c</sup>

<sup>a</sup>Department of Mechanical Engineering, University of Tabuk, Saudi Arabia.

<sup>b</sup>Faculty of Engineering and Technology, Multimedia University, Malaysia.

<sup>c</sup>School of Materials and Mineral Resources Engineering, Universiti Sains Malaysia.

Received 5 July 2015

Accepted 28 November 2015

## Abstract

Bronze -40%w Composites are successfully prepared by compacted mixtures powder into pellets. The green compacts of (bronz- 40wt%W) were sintered for (60- 120 min) at 750, 850, 950°C. Scanning Electron Microscopy (SEM) technique was used for microstructure test of the raw powders, and composites. The results obtained reveal that the densities increased with increasing compaction load, sintering time and temperature. The average of Vickers hardness for composites 60wt% bronze -40wt%W was 91.5. Tin electroplating improves corrosion resistance of the bronze/w, by electroplating with tin solution electrolyte and applying suitable current (0.01A) for 4 hour, coating layers of 45- 60 μm were obtained. Corrosion rate measurements were done for different samples with different conditions (non-coating, coating and scratched coating). The corrosion current of scratched coating sample is higher than unscratched samples, due to cathodic protection of exposed area of composite substrate. Consequently, the corrosion rate of scratched coating sample is higher than unscratched.

© 2016 Jordan Journal of Mechanical and Industrial Engineering. All rights reserved

**Keywords:** Bronze Matrix, Composites, Cu-WC, Corrosion.

## 1. Introduction

A considerable interest has been given to metal-metal composites and metal-ceramic composites because of their unique combination of strength, fracture toughness, high hardness, low density, low coefficient of thermal expansion that make them ideal candidates for light weight application [1,2]. Properties of lead, like flexibility, ease in obtaining, corrosion resistance, high density, and low melting point, make it easy to handle and fashion [3]. The combination of high density and good corrosion resistance can be considered as an advantage, which makes lead an excellent material for fishing application, and effective in manufacturing of many types of fishing tackles and angular accessories [4, 5]. Lead is ranked number two in the U.S. government's top 20 hazardous substances propriety list. The U.S. environmental protection agency has listed lead as a toxic chemical and set very restrictive threshold limits for concentrations in air, soil, water and vegetation [6, 7]. However, Lead can be replaced by tungsten because it has higher density and higher melting temperature than lead. Usually adequate mechanical properties and unusual properties are the main reason for fabricating by Powder Metallurgy (PM). Conventional method led to high cost reinforcing phase preparation and poor interface bonding between reinforcement and metal

matrix [8]. Copper alloy powder has been selected as a matrix, due to its availability with a low cost, while tungsten (W) powder, which has high density, has been selected as reinforcement to attain a fishing tackle with high density that imitate lead density. The fishing tackles use in sea water should have a good corrosion resistance. After preparation the sample surface electroplating was used to improve corrosion resistance [8]. Milling of elemental Cu, W and graphite mixture was undertaken by many researchers and they have studied the properties of Cu -W composites by mechanical alloying with different conditions [9-15]. The authors have not studied and comparing the structure, densities, hardness, and corrosion of (bronz- 40wt%W) as replacement composites materials of lead in many applications.

## 2. Experimental

In the present study, the starting materials chosen were bronze powders as matrix (purity 99.9%, purchased from ALDRICH) with a particle size of 325 meshes and tungsten powder (purity 99.9%, purchased from ALDRICH) with average particle sizes 100 meshes. Mixtures of ( bronz - 40wt%W) were subjected to ball milling for 2 h at the speed of 100 rpm then compacted into pellets by different loads (5-15Kgf which is equal 156050- 468152 N/M<sup>2</sup>(stress) when radius of the sample=

10mm) for 3 min. The green compacts of (bronz-40wt%W) were sintered by tube furnace under protective argon gas atmosphere for different sintering time (60 -120 min) and different sintering temperatures (750°C, 850°C, 950°C), The apparent density, green density and sintered density were taken for the powders and composites by using formula of  $\rho=m/v$  and using the gas pycnometer. Tin electroplating to improve corrosion resistance of the bronze/w, by electroplating with tin solution electrolyte and applying suitable current (0.01A) for 4 hour, coating layers of 45- 60  $\mu\text{m}$  were obtained for sample with (2.5 $\text{cm}^2$ ) surface area [14]. SEM technique was used for microstructure examination of the raw powders, and composites. The micro-Vickers hardness was measured at 5 points of the samples. The Corrosion Cell was designed for electrochemical measurements using Tafel extrapolation method with AUTOLAB software for

corrosion rate determination in 3.5 % NaCl solution as simulated environment to sea water. Corrosion rate measurements were done for different samples with different conditions (non-coating, coating and scratched coating).

### 3. Results and Discussion

#### 3.1. SEM and EDX Analysis

SEM micrographs of of bronze alloy powders, as in Fig. 1, show a spherical shape with different sizes.

The SEM image of the reinforcement powder (W) is shown in Fig. 3.2 the shape is clear polygonal with different sizes that are difficult to measure it due its irregularity. Powder characterization is necessary for future repetition and understanding the results.

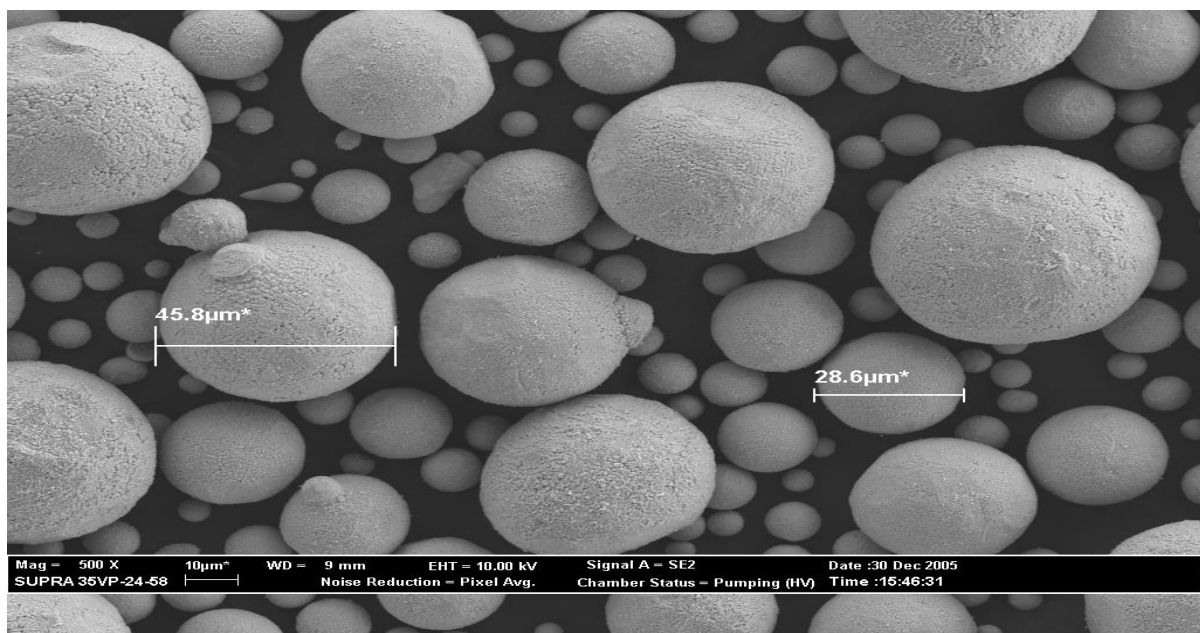


Figure 3.1. SEM micrograph of (a) bronze alloy powders, 500x

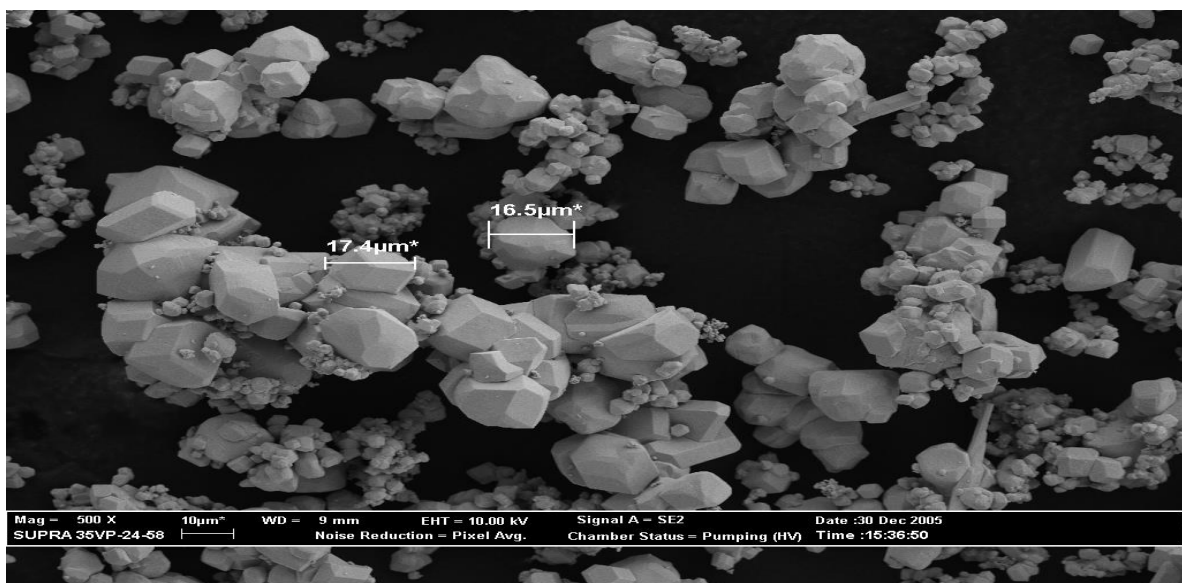


Figure 3.2. SEM micrographs of W powders, 500 X.

The matrixes of bronze alloy has been analyzed using EDX (Energy Dispersive X-ray) technique to determine and confirm its chemical compositions as show in Fig. 3.3 After select the point in the matrixes as show in Fig.

3.4. A uniform dispersion of reinforcement (W) powder in the metal matrix offers improvement in density and the mechanical properties of resultant composites as show in Fig. 3.4

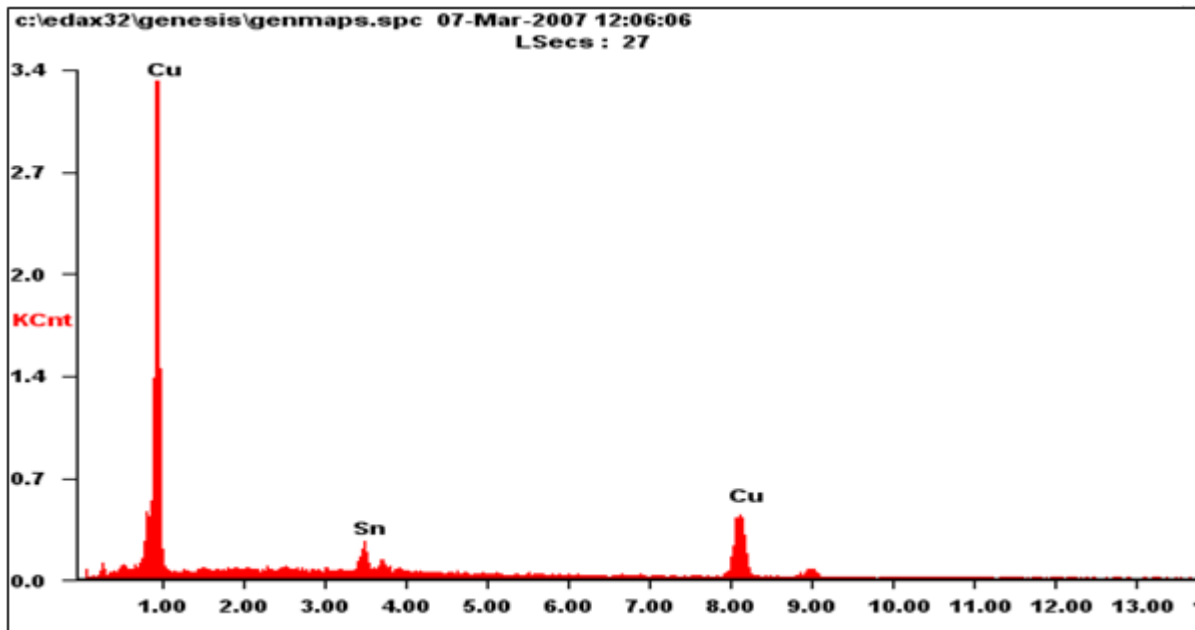


Figure 3.3. EDX microanalysis of matrix.

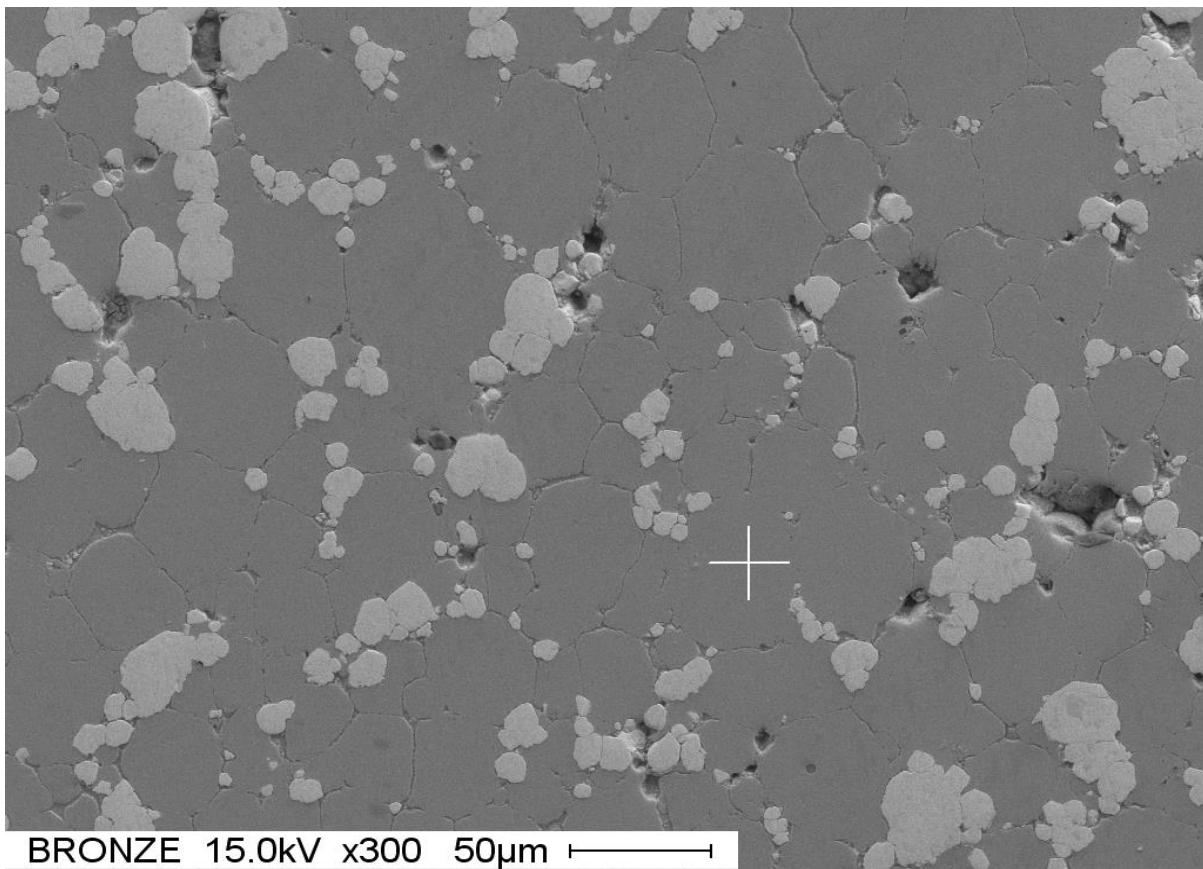


Figure 3.4. SEM micrograph shows the matrix

The reinforcement tungsten (w) has been analyzed using EDX (Energy Dispersive X-ray) technique to determine and confirm its chemical composition, as

shown in Fig. 3.5. After select the point in the reinforcement of composite as shown in Fig. 3.6.

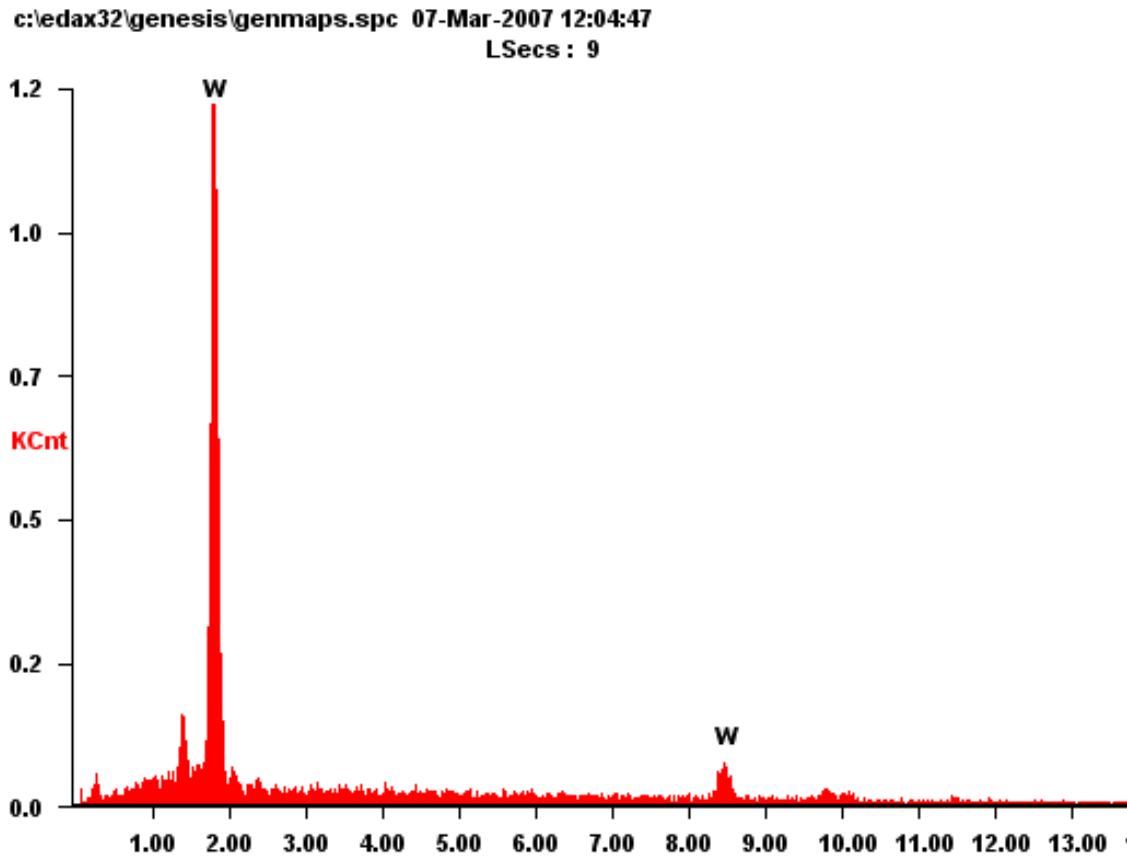


Figure 3.5. EDX microanalysis of reinforcement.

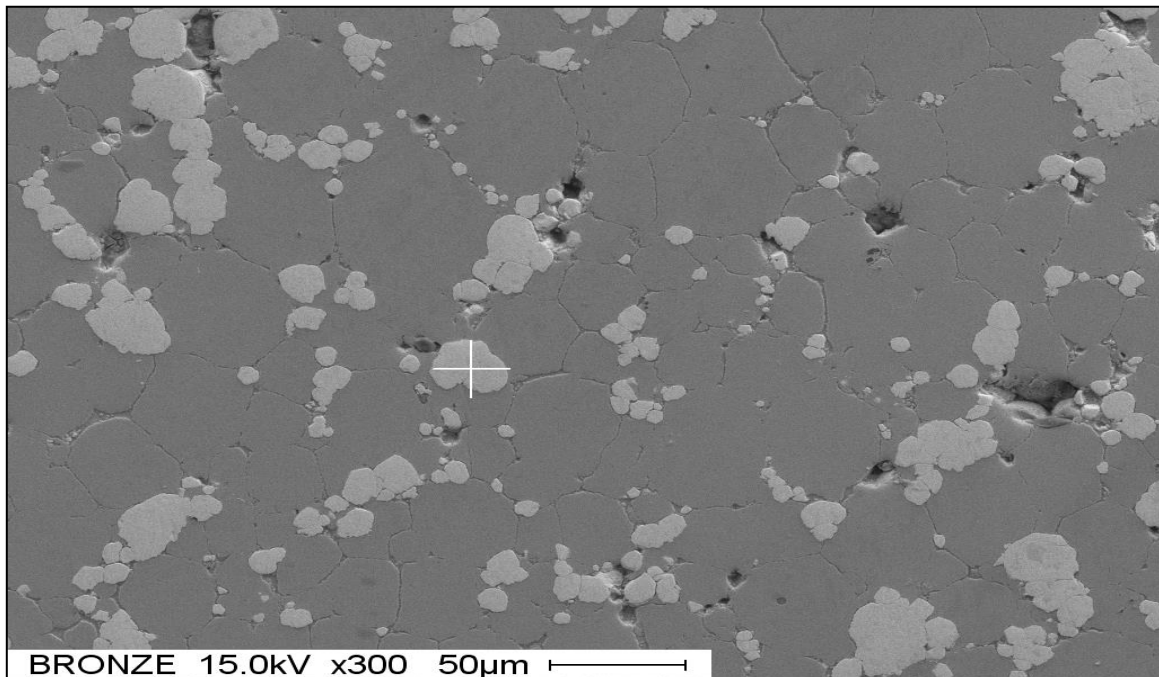


Figure 3.6. SEM micrograph shows the reinforcement

### 3.2. Density and Hardness Measurements

The aim of the present work is to replace the lead by bronze-w composites which have high density, good corrosion resistant and low cost. Therefore, the following of density improvement is required during powder technology process. The sintered densities were measured according to the formula of  $\rho = m/v$  to calculate the sintered density; where:

$\rho$  = density,  $m$  = mass of sample,  $v$  = volume  
 $v = \pi r^2 X d$ ,  $r$  = radius of the die cavity = 0.65 cm,  
 $d$  = thickness.

Apparent density is one of the fundamental properties of a powder, which affects processing parameters such as the design of compaction mould and the magnitude of the pressure motions required to compact. The average apparent density of bronze/tungsten powder was 5.90 g/cm<sup>3</sup> due to bronze has spherical shape as shown in Fig.1. The green density as a function of compacting load showed an increase with increasing the compacting load [17]. Table 3.1 illustrates the compressibility of the composite powder

**Table 3.1:** Compressibility of composite powder

Sample No.	The Type of composite	Load (Kgf)	The height of sample (cm)	$v = \pi r^2 X d$ cm <sup>3</sup>	Weight (g)	Green Density (g/cm <sup>3</sup> )
4	60wt%bronze-40wt%w	5,000	0.35	0.464	4.41	9.83
5	60wt%bronze-40wt%w	10,000	0.33	0.438	4.44	10.1
6	60wt%bronze-40wt%w	15,000	0.31	0.411	4.42	10.75

The green density increases with increasing the compacting load due to decrease the volume of the sample with increasing the load, the formula  $\rho = m/v$  was used to determine the density. From Table 3.1, the high green density of 60wt%bronze-40wt%w due to the bronze compatibility and apparent density, compatibility

depended on the type of the powder and the particle size of powder. From Table 3.1, the varying pressures between 5,000-15,000 (Kgf) were applied, by suitable pressure 10,000 (Kgf) good shapes after ejecting samples from the die were produced. The hardness was calculated from the diagonal length of the indentation optically determined for each indentation. The average of Vickers hardness for composites 60wt% bronze-40wt%W was 91.5. The bronze-w samples were sintered for 60 and 120 minutes at 850 °C under a protective atmosphere of argon gas. 10-ton was applied; sintered densities with 120 minutes were higher than sintered densities with 60 minutes, due to 2-hour sintering time enough to occur good densification (formation and growth of necks). The sintered density increases with increasing the sintering temperature but at high sintering temperature the sample particles were faced distortion and agglomeration because the matrix reached the point, as shown in Figure 3.7.



**Figure 3.7:** Samples bronze-w

A) before Sintering with a diameter of 10 mm

B) after Sintering temperature of 1000 °C (Distorted sample)

### 3.3. Corrosion Rate Measurements

SEM coating examination shows that the coating had a uniform layer, due to clear regularity and shows good coating adhesion with the substrate as shown in Figure 3.8 and the coating thickness varies between 30 μm and 58 μm.

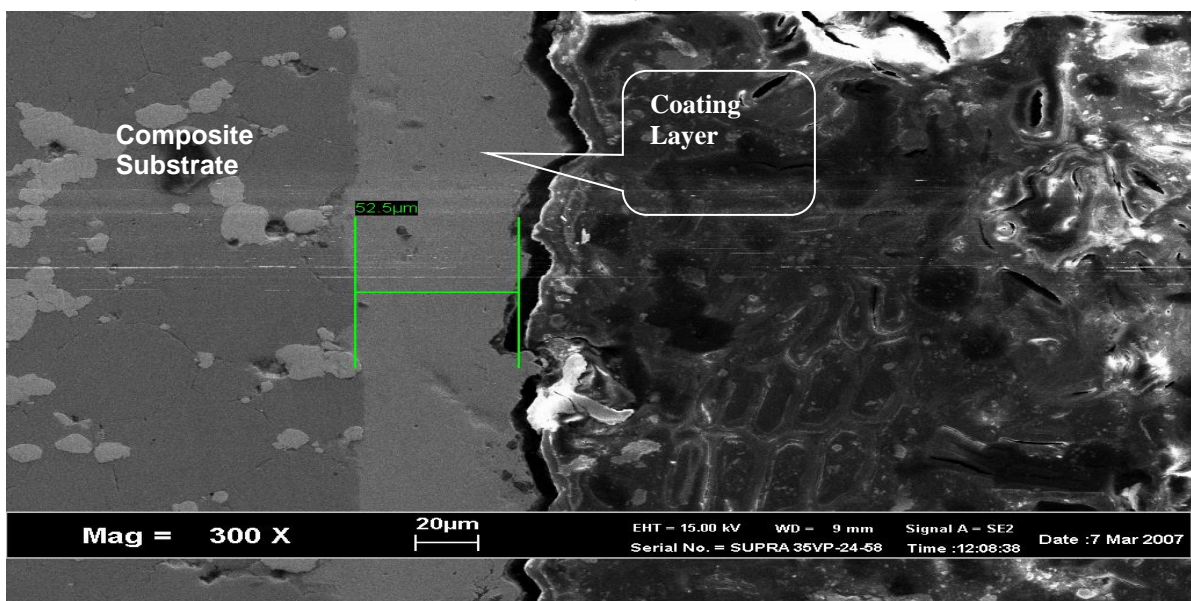


**Figure 3.8:** SEM micrograph shows the tin coating of thickness reveals good adhesion with the substrate (bronze-40%w)

By using AUTOLAB software corrosion rate was easily obtained. With polarization scan rate of 0.0005 V/second, density of sample 8.4 g/cm<sup>3</sup> and surface area 1.453 g/cm<sup>3</sup>. Figures (3.9) show the obtained results of different type of samples composition and conditions (un-scratched coating, scratched coating, and un-coated samples) with Tin (Sn), in 3.5 % NaCl solution at room temperature (25 °C),

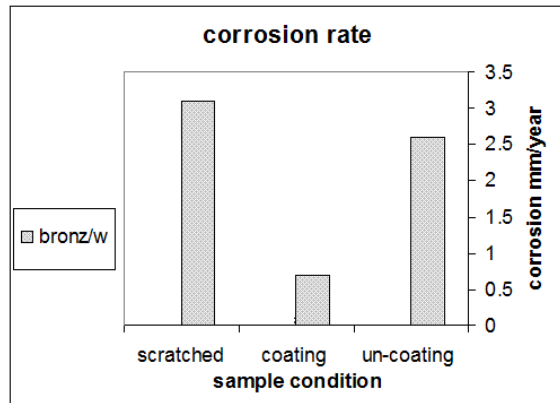


**Figure 3.9:** Corrosion rate for two composite with different condition

The corrosion behavior of a coated part (coating-substrate system) is determined by the corrosion resistance of the coating material in 3.5 % NaCl solution at room temperature medium. The coatings may be have two type defects: pores, damaged by scratches or other wear mechanisms, and other defects after electroplating process, the types of defects allow the corrosive medium to contact the substrate material [18]. That is why a coated sample was scratched with sharp tool to obtain scratched coating samples with scratch length of 10 mm, and 1 mm width. According to electrochemical series of metals, the coating metal which is Tin (Sn), is less noble than the substrate material, which is considered as Copper alloy, (the substrate material is composite material contains of 40 wt% of W reinforcement matrix of (bronze) [19]. It is an example of a corrosion cell, which is provided by an imperfect (scratched) coating of Tin (Sn) on composite samples immersed in 3.5 % NaCl solution. The current generated passes from the copper to the tin by the path of lowest resistance and returns to the copper through the solution by the passage of ions. The tin dissolves and is called the anode; whilst the copper is called the cathode. The corrosion current density of the scratched samples is more than un-scratched coating samples [20]. The corrosion current of scratched coating sample is higher than unscratched samples, due to cathodic protection of exposed area of composite substrate. Consequently, the corrosion rate of scratched coating sample is higher than unscratched.

#### 4. Conclusion

Work has been done to prepare non lead heavy weight composites for fishing tackles application. Composites of bronze with reinforcement of 40 wt%w were produced. Proper powder mixing lead to homogenous tungsten distribution and two hours sintering time at 850 °C was suitable time to improve the density and hardens. Slight improvement in density when sintering temperature

increased from 850-900°C was observed. However sintering at 1000 °C was found detrimental on the final shape due to distortion by melting. Tin electroplating to improve corrosion resistance of the bronze/w, Thickness of coating layers that obtained were 45- 60 μm by electroplating with electrolyte(tin solution) by applied suitable current (0.01A) for 4 hour. The Corrosion Cell was designed for electrochemical measurements using Tafel extrapolation method with AUTOLAB software for corrosion rate determination in 3.5 % NaCl solution as simulated environment to sea water. Corrosion rate measurements were done for different samples with different conditions (non-coating, coating and scratched coating). The corrosion current of scratched coating sample is higher than unscratched samples, due to cathodic protection of exposed area of composite substrate. Consequently, the corrosion rate of scratched coating sample is higher than unscratched.

#### Acknowledgement

The authors would like to acknowledge the financial support this work received from the Deanship of Scientific Research (DSR), University of Tabuk, Tabuk, Saudi Arabia, under grant No. S-1436-0019.

#### References

- [1] A. Al-Hamdan, L. Yassin, J. Ramadan, "Ballistic Impact Fracture Behaviour of Continuous Fibre Reinforced Al-Matrix Composites", *JJMIE*, Vol. 4, 2010, 605 – 614.
- [2] K. V. Gangadharan, K. S. Umashankara, V. Desaia, "Machining Characteristics of Multiwall-CNT Reinforced Al/Al-Si Composites using Recurrence Quantification Analysis", *JJMIE*, Vol. 5, 2011, 345 – 351.
- [3] S. H. Seong, P. K. Hong, H. L. Deok, C. K. Uh, S. K. Joung, "The mode of stress corrosion cracking in Ni-base alloys in high temperature water containing lead", *Journal of Nuclear Materials*, Vol. 275, 2011, 28-36.
- [4] K. Tucek, J. Carlsson, H. Wider, "Comparison of sodium and lead-cooled fast reactors regarding reactor physics aspects, severe safety and economic issues", *Nuclear Engineering and Design*, Vol. 236, 2006, 1589–1598.
- [5] G. C. Leopoldo, W. Bodo, W. Jobst, C. M. Mariela, "Tracing toxic elements sources using lead isotopes: An example from the San Antonio–El Triunfo mining district, Baja California Sur, México", *Applied Geochemistry*, Vol. 59, 2015, 23–32.
- [6] A. Bhattacharya, R. Shukla, K. N. Dietrich, R. L. Bornschein, "Effect of early lead exposure on the maturation of children's postural balance", *Neurotoxicology and Teratology*, Vol. 28, 2006, 376–385.
- [7] F.V. Lenel, "Powder metallurgy principles and application Metal Powder Industries Federation Princeton", New Jersey, 1980, 14-21.
- [8] G. N. Bala, M. K. Vamsi, M. Anthony, "A Review on Processing of Particulate Metal Matrix Composites and its Properties", *International Journal of Applied Engineering Research*, Vol. 8, N. 6, 2013, 647-666.
- [9] M.A. Ashworth, G.D. Wilcox, R.L. Higginson, R.J. Heath, C. Liu, R.J. Mortimer, "The effect of electroplating parameters and substrate material on tin whisker formation", *Microelectronics Reliability*, Vol. 55, 2015, 180–191.
- [10] J.P. Stobrawa, Z.M. Rdzawski, W. Gluchowski, J. Domagała-Dubieli, "Nanocrystalline copper based microcomposites", *Journal of Achievements in Materials and Manufacturing Engineering*, Vol.54, 2012, 49-57.

- [11] S.A. Hewitt, K. A. Kibble, " Effects of ball milling time on the synthesis and consolidation of nanostructured WC–Co composites", *Int J Refract Met Hard Mater* Vol. 27, 2009, 937–48.
- [12] T. Raghu *et al.*, "Synthesis of nanocrystalline copper-tungsten alloys by mechanical alloying", *Materials Science and Engineering A*, vol. 304, 2001, 438-441.
- [13] Y. Li *et al.*, "Properties of W-Cu composite powder produced by a thermo-mechanical method", *International Journal of Refractory Metals and Hard Materials*, vol. 21, 2003, 259-264.
- [14] S. N. Alam, "Synthesis and characterization of W-Cu nanocomposites developed by mechanical alloying", *Materials Science and Engineering: A*, vol. 433, 2006, 161-168.
- [15] Y. Mahani, O. Radzali, H. Zuhailawati, "Mechanical alloying and sintering of nanostructured tungsten carbide-reinforced copper composite and its characterization", *Materials and Design*, Vol. 32, 2011, 3293–3298
- [16] J.P., "Electrodeposition of graphite-bronze composite coatings and study of electroplating characteristics", *Celis Surface and Coatings Technology*, Vol.187, 2004, 293-299.
- [17] S. M. El-Katatny, A.E. Nassef, Aly El-Domiaty, W. H. El-Garaihy, "Fundamental Analysis of Cold Die Compaction of Reinforced Aluminum Powder", *International Journal of Engineering and Technical Research*, Vol.3, 2015, 180-184.
- [18] J K Wood, " Tribo-corrosion of coatings", *Journal of Physics D: Applied Physics* . 40, 2007, 5502–5521.
- [19] A. M.A. Alsamuraee, H. A. Ameen, " The effect of Zinc, Tin, and Lead coating on corrosion protective effectiveness of steel reinforcement in concrete", *AMERICAN Journal of Scientific and Industrial Research*, Vol.2, 2011, 89-98.
- [20] A. Gulec, O. Cevher, A. Turk, F. Ustel, F. Yilmaz, " Accelerated Corrosion Behaviors of Zn, Al and Zn/15Al Coatings on A Steel Surface", *Materiali in tehnologije / Materials and technology*, 45, 2011, 477–482.



# Investigation of Local Hemodynamics Effect in Disturbed Flow Interactions

Abdullah Alshorman \*

Al-Balqa` Applied University – Al-Huson University College - Mechanical Engineering Department, P.O.Box 50, Al-Huson 21510 – Irbid - Jordan

## Abstract

Physiologically, blood flow path has different patterns of geometry, shapes, size and structure within the cardiovascular system. This includes branching, bifurcation and curvature of blood vessels and other cardiovascular components.

Accordingly, the blood micro interactions with the lining layer (Endothelium Layer) of blood vessels and surrounding surfaces are strongly depend on blood constitutions, mechanical properties of endothelial layer and the geometry of blood pathways. This demonstrating the importance of local hemodynamics in controlling disturbed flow interactions, which include leukocytes aggregation and platelets adhesion.

In the present study, a numerical simulation of blood-surface interactions are performed to investigate the complicated behavior of blood flow and how the local hemodynamics control the adhesion and rolling processes around a stagnation point at branching and curvature locations within cardiovascular system. These investigations are carried out under effect of variable shear stress, and different timing of secondary adhesion technique.

The results showed that the discontinuity in the hemodynamic flow enhances cell adhesion under low shear rate at and downstream the disturbed portion in the flow (i.e., stenosis flow). Also, cell prefers to adhere to the surface between the discontinuity and little bit further the stagnation point, but the maximum tendency for adhesion is before the stagnation point, which synchronized with the lowest value of shear rate. However, at higher shear rate (i.e., 19.66 s<sup>-1</sup>) the cell will roll slowly for short time before its rolling velocity gradually increases to reach a maximum value when the shear rate gets higher.

© 2016 Jordan Journal of Mechanical and Industrial Engineering. All rights reserved

**Keywords:** Disturbed blood flow, stagnation point, shear stress, hemodynamics.

Nomenclatures			
$a_c$	Cell radius	$K_f$	The intrinsic bond formation rate constant
$a_{co}$	Characteristics cell radius (Reference value)	$K_{ro}$	The intrinsic bond breakage rate constant
$A(\theta, \phi)$	Individual grid area of the receptors over the cell surface	$L_b$	bond length
$C_x$	Distance from the step	$m$	mass of the cell
$C_y$	Distance between the cell center and the vessel surface	$M_{bz}$	Moment of the bond force in z-direction
$F_b$	The bonding force	$n_{Ro}$	Receptors of density while the
$F_{bi}$	The bonding force in Cartesian Coordinate (i=x,y and z)	$n_{Lo}$	Ligands of density
$F_{fx}$	Hemodynamic force x-direction (Fluid force)	$n_B$	Bonds of density
$F_{fy}$	Hemodynamic force y-direction (Fluid force)	$S$	Stiffness constant
$f_k$	Fraction of bond strain that is dedicated to bond dissociation, (fractional spring slippage)	$S_{ts}$	Transition state spring constant,
$F_s$	Function of $(a_c + h)/a_c$	$T$	The temperature
$G$	Shear rate	$T_{max}$	Overall time of simulation
$G_o$	Characteristic shear rate (Reference value)	$V_{cell}$	Cell velocity
$h$	The minimum distance between the cell and the surface	$V_f$	Velocity of the fluid with respect to the cell velocity $V_{cell}$
$I$	Mass moment of inertia of the cell	$\delta t$	Time step
$K_B$	Boltzmann constant	$\delta c_i$	Indices of the cell center in Cartesian Coordinate (i=x,y and z)
$K_b$	Bond breakage constant	$\lambda$	Stressed bond length
		$\lambda_o$	Equilibrium (unstressed) bond length
		$\mu$	The fluid dynamic viscosity
		$\Omega_i$	The three components of rotational velocity in Cartesian Coordinate (i=x,y and z)
		$\rho$	Fluid density
		$\tau$	Dimensionless time

\* Corresponding author e-mail: alshormana@asme.org.

Anchoring of blood cells to the surface of the blood vessel starts by the migration of cell from the blood stream toward the vessel surface; this may be followed by primary adhesion, rolling or permanent adhesion. These processes are essential events in physiological adhesion for instance Leukocyte accumulation during inflammation, tumor cell metastasis and thrombus formation [1]. However, adhesion and aggregation of platelets and neutrophils to each other and to blood vessel wall are critical events in inflammation and thrombosis, and are relevant to patients with stroke, acute myocardial infarction and coronary angioplasty [2, 3].

Under flow conditions, cell adhesion initiates by cell departure from the main bloodstream toward the vessel wall (cell capture), and then the cell slow rolling takes place (adhesive rolling) before the permanent adhesion happens (secondary adhesion). The driving force for rolling is the hydrodynamic force of the blood stream (hemodynamic force) acting on the adherent cell; rapid formation and breakage of adhesive bonds are required for the adhesive contact between the blood cell and the vessel wall to be maintained and to be translated along the wall during rolling [4,5]. On the way to inflammatory sites, neutrophils attach to and roll on endothelium before their firm arrest and diapedesis. The attachment and rolling of neutrophils are mediated by selectins (L-selectin on neutrophils; P-selectin and E-selectin on endothelium) and their carbohydrate ligands [6].

Fundamentally, cell adhesion/rolling depend on many parameters that are related to the flow conditions, cellular properties, bond characteristics, and interactions activity of the lining layer of the blood vessel (i.e., endothelium layer). Mainly, flow parameters include the flowing path, properties of the working fluid (i.e., blood or plasma), type of flow (laminar and turbulence levels and vessel size and shape), and local hemodynamics. The vascular endothelium cell is subjected at all time to shear forces that act on its surface and has an important role in regulating cell structure in endothelium and cardiac myocytes as a result of flow of viscous blood [7]. However, the viscous effect of blood has an important role in hemodynamics of blood stream, especially at stagnation points (zero velocity point) through the blood flow and at the disturbed portion (the discontinuity in the flow) [8].

The hemodynamic force depends mainly on the rate of shear and on the blood rheology. In addition to hemodynamic force, cell receptors and surface legends densities (site densities) have a crucial role in cell adhesion and rolling. However, the adhesion of cells to surfaces under conditions of flow represents a balance between physical and chemical forces. The chemical bonding force delivered by the receptor-ligand pair balances the hydrodynamic forces on the cell. This chemical bonding

force is derived from the numbers and strength of adhesive linkages between cell and surface, which results from the properties of adhesion molecules [9, 10].

In the light of the above, it is important, therefore, to fully understand the mechanisms of fluid cell, capture, rolling and permanent adhesion under flow conditions. Of particular relevance is the role of local hemodynamics of blood flow in the cell-surface interactions. However, a fundamental quantitative understanding of cellular behavior can lead to better understanding of in vivo phenomena.

Accordingly, this study makes steps towards elucidation of the cell-surface interactions under flow conditions, such that a three-dimensional (3D) computational model was developed to simulate and investigate the effect of local blood hemodynamics in the cell adhesion and motion over the endothelium layer at the bifurcation sites of the cardiovascular system.

## 2. Methods and Model Development

The details of the biodynamical model and the coordinate axes appear through Figures 1-3. In this model, the blood cell (i.e., Leukocytes or neutrophils) is modeled to be an inflexible sphere of radius  $a_c$  covered by uniformly distributed receptors of density  $[n_{R_o}]$  while the substrate (i.e., Endothelium layer) has ligands of density  $[n_{L_o}]$ . The resulting receptors-ligands combination (bonds)-within the contact zone- are modeled as Hookean springs with stiffness constant of  $S$  and equilibrium (unstressed) bond length of  $\lambda_o$ , while the stressed bond length is represented as  $\lambda$ .

Within the contact zone, the rate of bond formation constant ( $K_f$ ) and breakage constant ( $K_b$ ) are determined using the expressions suggested by Bell model [11] which is modified by Dembo *et al.*, 1988 [12]:

$$K_f = K_{f_0} \exp(-S_{is}(\lambda - \lambda_o)^2 / 2 K_B T) \quad (1)$$

$$K_b = K_{b_0} \exp(f_k S (\lambda - \lambda_o)^2 / 2 K_B T) \quad (2)$$

Here  $\lambda$  is the bond length (the magnitude of the vector of Eqn.1),  $f_k$  is the fraction of bond strain that is dedicated to bond dissociation, and is also known as the fractional spring slippage, and is given by  $f_k = [ (S - S_{is}) / S ]$ . The term  $( K_B T )$  is product of the Boltzmann constant and temperature,  $S$  is the spring constant,  $S_{is}$  is the transition state spring constant,  $K_{f_0}$  and  $K_{b_0}$  are the intrinsic bond formation and breakage rate constants [1,13,14].

The bonding force  $F_b$  will depend on the deflection of the bond length  $(\lambda - \lambda_o)$ , which is related to the  $(x,y,z)$  coordinates of the tether on both the cell  $L_1(x_1,y_1,z_1)$  and that on the substrate  $L_2(x_2,y_2,z_2)$ , such that  $F_b$ ,  $L_1$  and  $L_2$  are vector quantities. The vectors  $L_1$  and  $L_2$  change with time as a result of cell rotation and translation, so the bond length at each location can be described by a time varying vector:

$$L_b = L_2 - L_1 \quad (3)$$

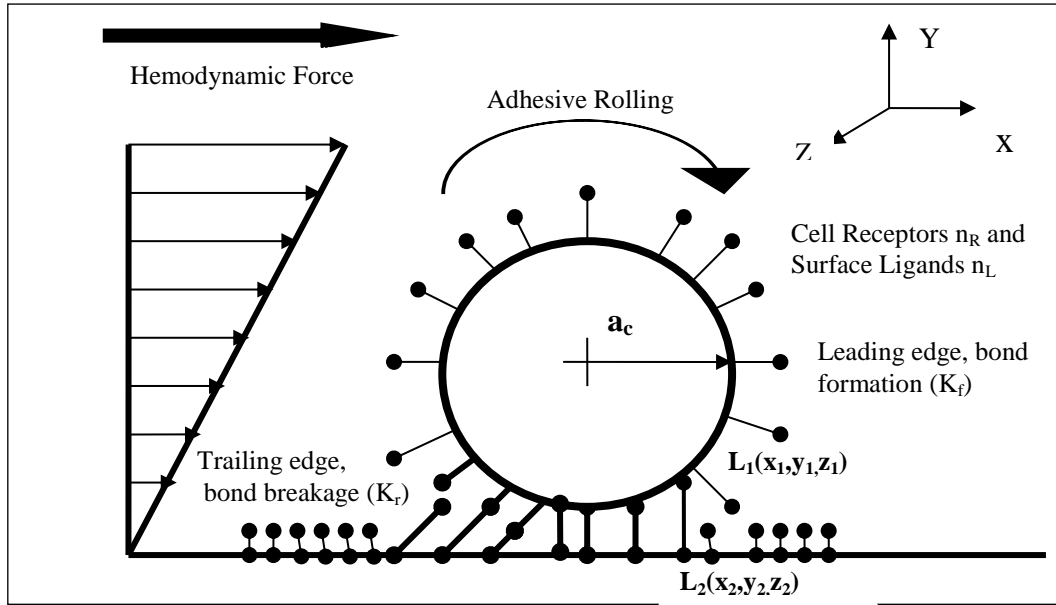


**Figure 1.** The cell is modelled as a sphere of radius  $a_c$ , covered with the receptors with a density of  $[n_R]$ , while the ligands covered the substrate at a density of  $[n_L]$ . Rolling occurs when the bonds at the trailing edge of the cell start to break

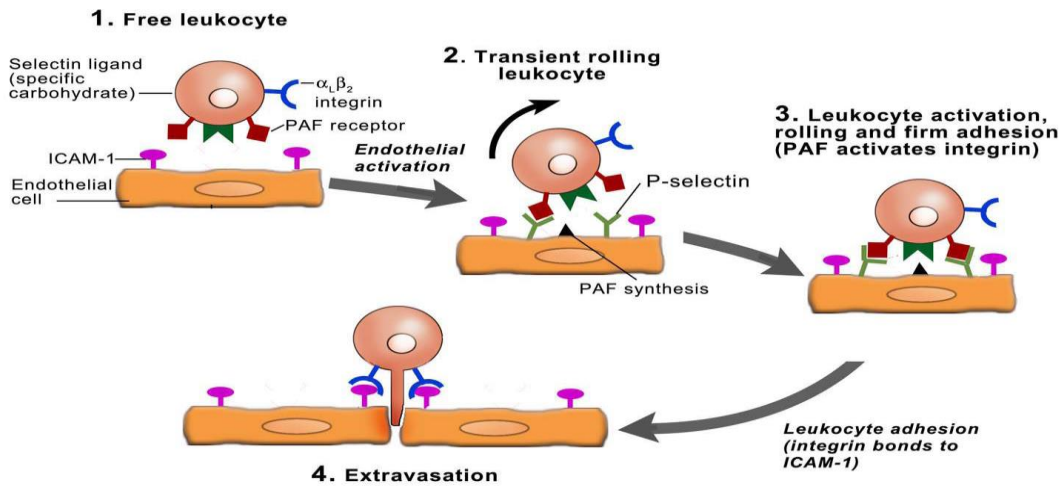


**Figure 2.** The four steps of cell adhesion under effects of shear effects [15]

In the contact region, ligands react with receptors at rate of bond formation ( $K_f$ ) to form bonds of density  $n_B$ , so

the rate of bond formation  $\frac{dn_B}{dt}$  is given by:

$$\frac{dn_B}{dt} = K_f n_R n_L - K_r n_B \quad (4)$$

Where  $n_B$ ,  $n_L$  and  $n_R$  are the density in [number of sites/ $\mu\text{m}^2$ ] of the bond, ligand and receptor, respectively.

Accordingly, the bond force can be resolved in each direction  $F_{bx}$ ,  $F_{by}$  and  $F_{bz}$ , and the associated torques can also be calculated using the above appropriate parameters; subsequently, the single bond force in each Cartesian direction can be expressed as:

$$F_{bx} = S L_{bx} \left( 1 - \frac{L_{bo}}{L_b} \right) \quad (5)$$

$$F_{by} = S L_{by} \left( 1 - \frac{L_{bo}}{L_b} \right) \quad (6)$$

$$F_{bz} = 0.0 \quad (7)$$

Here,  $F_{bz}$  equals zero since there is no cell motion in  $z$ -direction and  $\lambda_z$  doesn't change, while the total bond forces take the following forms:

$$\Sigma F_{bx} = S \lambda_x \left( 1 - \frac{\lambda_o}{\lambda} \right) n_B A(\theta, \phi) \quad (8)$$

$$\Sigma F_{by} = S \lambda_y \left( 1 - \frac{\lambda_o}{\lambda} \right) n_B A(\theta, \phi) \quad (9)$$

$$\Sigma M_{bz} = \lambda_x y_1(\theta, \phi) + \lambda_y x_1(\theta, \phi) \quad (10)$$

Here,  $n_B$  is the bond density, and  $A(\theta, \phi)$  is the individual grid area of the receptors over the cell surface (Fig. 3). Fig. 3 shows the resultant of the bonds in each grid of the cell surface, such that the resultant summation of the individual bonds is located at the center of the grid. Also,  $x_1(\theta, \phi)$  and  $y_1(\theta, \phi)$  are the location distance of the receptors on the cell surface in  $x$  and  $y$  directions.

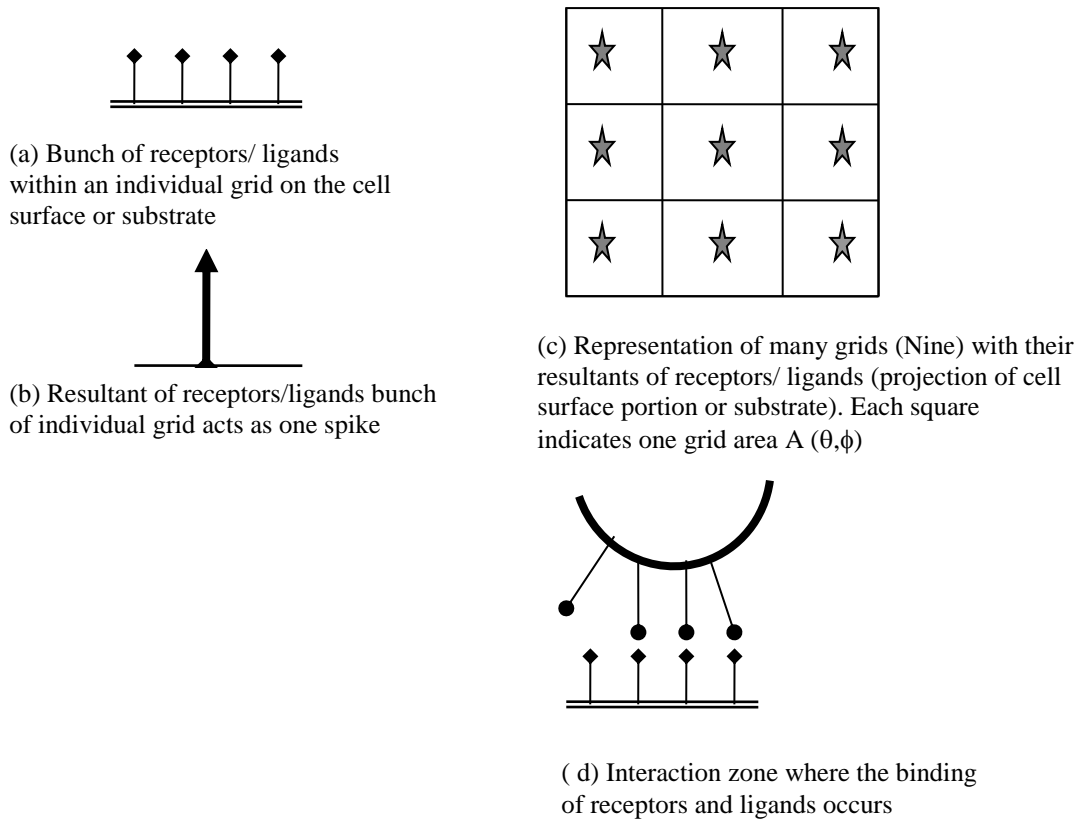


**Figure 3.** Representation of the spherical grid over the cell surface / substrate surface, such that each small square indicates one individual grid area  $A(\theta, \phi)$  and the effect of receptors/ligands resultant acting at the centres of the small squares

The driving effect on the cell is the hydrodynamic (hemodynamic) force such that the effects of bond keep opposing the hemodynamic contribution to achieve the stability of adhesive rolling. However, rolling occurs as long as the hemodynamic force is greater than the integrated effect of bond forces, while permanent adhesion is associated with the dominant role of bond forces against the driving effect. Particularly, hemodynamic force can be derived to take the following form [1, 14, 16, 17, 18]:

$$F_{flx} = 6 \pi \mu a_c^2 (G - V_x / d_y) F_s \quad (11)$$

$$F_{fly} = -6 \pi \mu a_c V_x F_s \quad (12)$$

where  $G$  is shear rate in  $x$ -direction,  $\mu$  is the fluid dynamic viscosity,  $F_s$  is a function of  $(a_c + h)/a_c$  such that  $h$  is the minimum distance between the cell and the surface, the value used for  $F_s$  is (1.7) (Goldman *et al.*, 1967),  $V_x$  &  $V_y$  are the velocity of the cell in  $x$  and  $y$  direction, and  $C_y$  is the distance between the cell center and surface.

As a result of net effects of hemodynamic and bond forces the cell moves at rolling velocities  $V_x$ ,  $V_y$  and  $V_\phi$  under certain values of bond formation and dissociation rates constants ( $K_f$  and  $K_b$ ). The motion of the cell was determined by solving Newton's law of motion, balancing fluid and bond forces with inertia, such that:

$$\Sigma F_x = \Sigma F_{bx} + F_{flx} \quad (13)$$

$$\Sigma F_y = \Sigma F_{by} + F_{fly} \quad (14)$$

Here  $\Sigma F_{bx}$  and  $\Sigma F_{by}$  are determined by Eqns. 8 & 9, while the fluid forces  $F_{fl}$  can be calculated using Eqns. 11

& 12 and the relative velocity of the fluid  $V_f$  with respect to the cell velocity  $V_{cell}$  (i.e.,  $V_f - V_{cell}$ ):

$$F_{fl} = 6 \pi \mu a_c^2 [V_f - V_{cell}] F_s \quad (15)$$

Fluid velocity  $V_f$  can be evaluated as a function of shear rate  $G$  and the distance between the cell center and the surface  $C_y$ , so:

$$V_f = G C_y \quad (16)$$

Then

$$V_f - V_{cell-i} = G - \frac{V_{cell-i}}{C_y}, \quad i = x, y, z \text{ or } \phi \quad (17)$$

The cell velocity components ( $V_x, V_y, V_\phi$ ) are expressed by Eqn. 24 below, while the fluid force components are:

$$F_{flx} = 6 \pi \mu a_c^2 [G - (\frac{\partial c_x}{\partial t C_y})] F_s \quad (18)$$

$$F_{fly} = -6 \pi \mu a_c^2 (\frac{\partial c_y}{\partial t C_y}) F_s^* \quad (19)$$

Where  $\mu$  is the dynamic viscosity of plasma, which is equal to 1-2 centi-poise (cp.) (i.e.,  $\mu = 1 \times 10^{-6} - 2 \times 10^{-6}$  g/ $\mu$ m.s) [10,22,29,32,33],  $G$  is the shear rate,  $C_y$  is the total height of the cell center from the substrate such that  $C_y = \Sigma \delta c_y$ , and  $F_s^*$  is function of the ratio of distance between cell center and substrate  $h$  and cell radius  $a_c$ , ( $F_s^* \sim 1 + (9/16)(a_c/h)$  for small  $(h/a_c)$ ). Numerical values of  $h/a_c$

and their associated values of  $F^*$  are introduced and tabulated by Goldman *et al.*, 1967,  $F^*$  ranges from 1.0 to 1.7005). The shear-induced force approach finite limits as the cell contacts the wall, thus  $F^* = 1.7005$  for the limiting case  $h/a_c = 1.0$ , [16, 17, 23, 24, 25].

Consequently, the general form of equation of cell motion can be expressed in the following form (Eulerian approximation method):

$$\sum F = m \frac{(\partial c_{i+1} - \partial c_i)}{\partial t^2}, \quad i = x, y, z \text{ or } \phi \quad (20)$$

Based on Eqn. 20, cell motion can be characterized by the indices of the cell center in each Cartesian co-ordinate  $\delta c_x$ ,  $\delta c_y$  and  $\delta c_\phi$  that are governed by Eqns.(21-23).

$$\delta c_{x+1} = \frac{(\partial t)^2}{m} \sum F_x + \delta c_x \quad (21)$$

$$\delta c_{y+1} = \frac{(\partial t)^2}{m} \sum F_y + \delta c_y \quad (22)$$

$$\delta c_{\phi+1} = \frac{(\partial t)^2}{I} \sum M_z + \delta c_\phi \quad (23)$$

Where  $\delta c_i$  is the infinitesimal change in cell center position in  $i$ -direction ( $i = x, y$  &  $z$  or  $\phi$ ) at time  $t$ , while  $\delta c_{i+1}$  is that at time  $t + \delta t$  and  $I$  is the mass moment of inertia of the cell as it is modeled as sphere.

The cell moves in both translation and rotation modes with three different components of translation velocity in each Cartesian co-ordinate  $V_x$ ,  $V_y$  and  $V_z$ , while  $\Omega_x$ ,  $\Omega_y$  and  $\Omega_z$  are the three components of rotational velocity. According to the model,  $V_z$ ,  $\Omega_x$  and  $\Omega_y$  are equal zero since there is no translation in  $z$ -direction and no rotation about  $x$  and  $y$  axis. Obviously, the cell translates in the  $x$  and  $y$  directions at  $V_x$  and  $V_y$  and rolls at  $\Omega_z$  or  $V_\phi$  about  $z$ -direction ( $V_\phi$  is considered instead of  $\Omega_z$  for notation consistency). These instantaneous velocity components are modeled to be in the following form:

$$V_i = \frac{\partial c_i}{\partial t}, \quad i = x, y, \phi \quad (24)$$

The cell rolling velocity is evaluated at each time step  $\delta t$  for the whole different stages of adhesion and rolling processes within the time of simulation  $T_{max}$ .

### 3. The Main Features of Flow at Localized Zones under Variable Shear Rate

To highlight the characteristics of the local hemodynamics of blood flow at localized sites (i.e., branching, contraction expansion, tapering), the path flow over the step is investigated since it could be considered as an interpretation for these restricted locations.

The flow over the step has a complicated nature due to discontinuity in the path of flow, circulation and back flow downstream the step, also this type of flow can be considered as primary related to stenosis flow and flow through branching vessels, such as the blood flow over cell adherent accumulation (plaque), or disturbed vessel flow respectively.

The schematic diagram and stream lines of step flow are shown in Figs. 4 and 5, where cell adhesion occurs around the stagnation point and back flow in the circulation zone. While the non-dimensional and the dimensional shear rate distribution over the distance from the step are illustrated in Figs. 6 and 7, respectively. This distribution is for Reynolds number (Re) of 28.5, dynamic viscosity of  $7 \times 10^{-7} \text{ g}/\mu\text{m}\cdot\text{s}$  and  $300 \mu\text{m}$  for the step height.

According to Fig. 6, the shear rate starts from zero at the beginning of the step then decreases in negative to reach its peak negative value after which it increases to come back to zero value at the stagnation point at the non-dimensional distance ( $C_x / a_c$ ) of 162. Here,  $C_x$  is the position distances of the cell along  $x$  axis, while  $a_c$  is the characteristics cell radius. Just slightly next the stagnation point, the shear rate changes sharply from zero up to its maximum value before it takes its constant value ( $G/G_o = 1.0$ ) which is the used characteristics value ( $G_o$ ) for the non-dimensionalizing process.

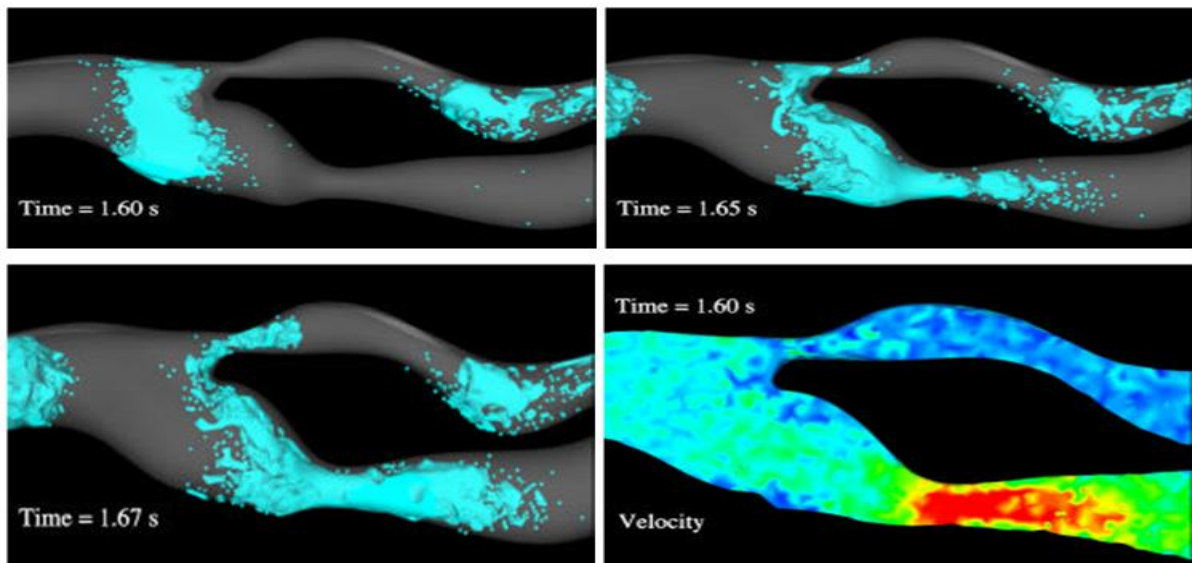


Figure 4-a. CFD of bifurcation flow at different times indicating stagnation points and adhesion regions [26].

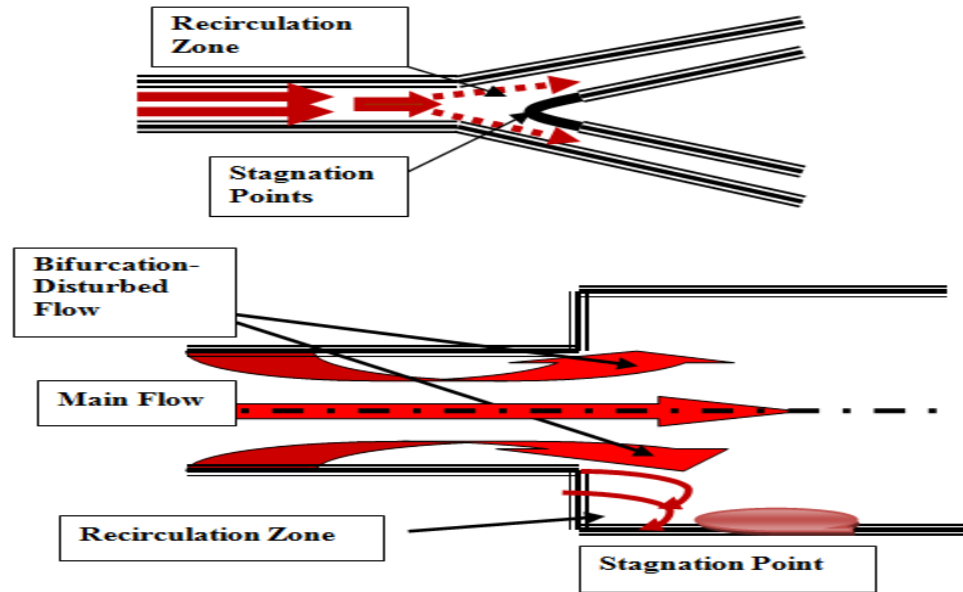
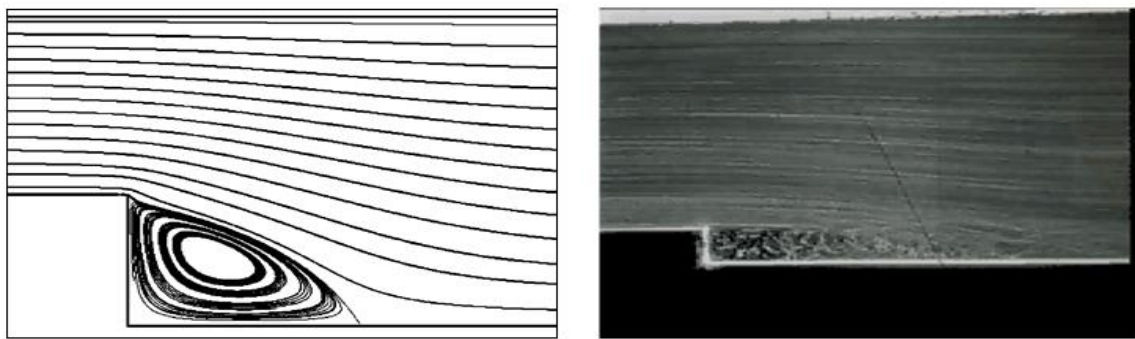


Figure 4-b. Disturbed flow representation: Arteries bifurcation, step flow, recirculation zone and stagnation point



a. CFD visualization

b. Flow visualization [27]

Figure 5. Disturbed step flow field: Circulation zone with back flow, stagnation point and recirculation

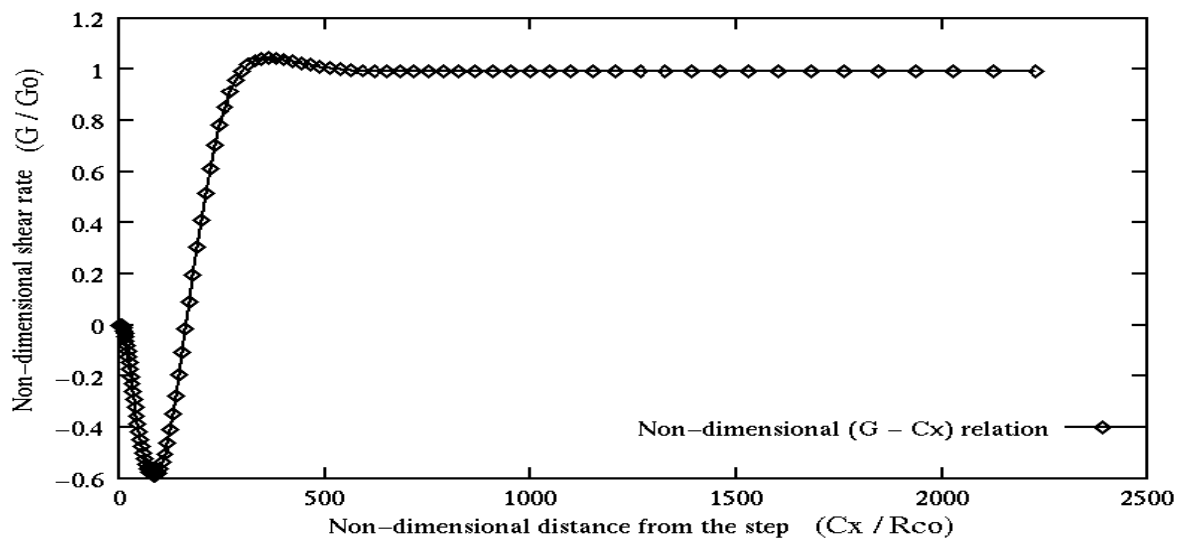


Figure 6. Non-dimensional shear rate distributions over the non-dimensional distance from the step

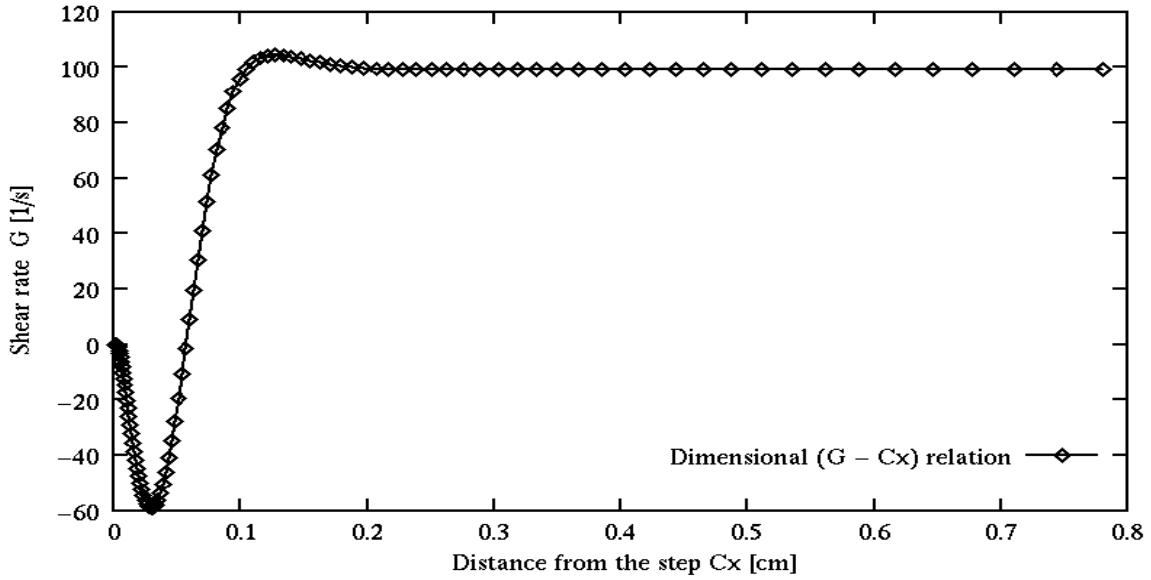


Figure 7. Shear rate distributions over the distance from the step (dimensional values)

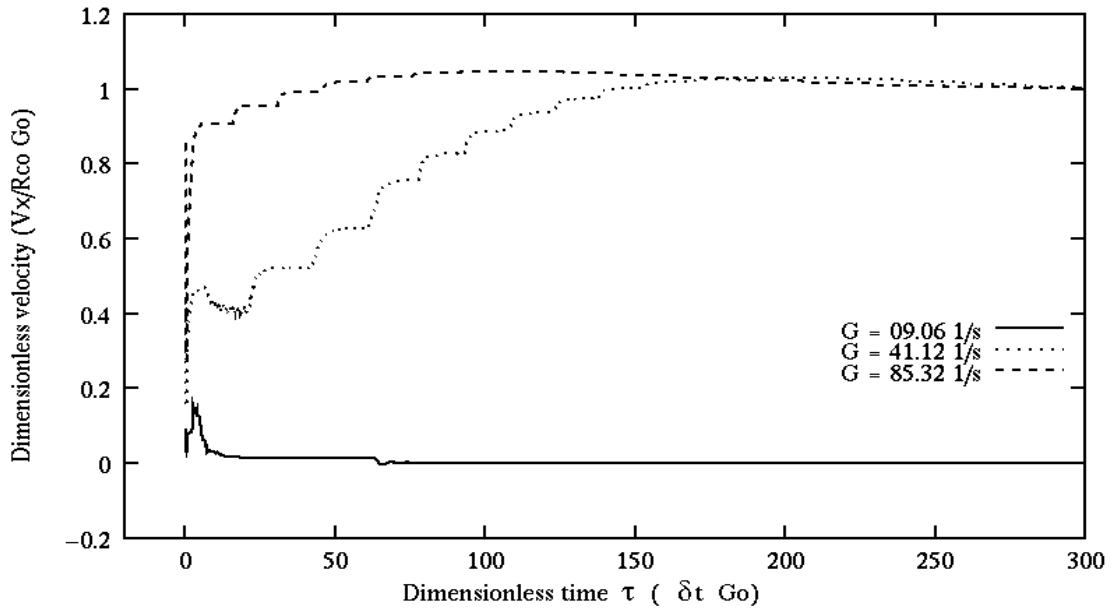


Figure 8. Cell capture, rolling and secondary adhesion under range of positive variable shear rate (after the stagnation point location)

#### 4. Results and Discussion

In the present study, an instantaneous-continuous reading of shear rate is performed at each cell position in each simulation run for the entire data of Fig. 6. Set of simulations were executed to analyze the features of cell capture, rolling and adhesion under the conditions of disturbed flow. The setting of input parameters of simulation are listed in Table 1 and the results are presented through Figs. 8 –10 and 12-13.

The results demonstrate the type of cell behavior within the effective range of shear rate (capture, rolling

or adhesion) and show the direction of cell motion under the conditions of the current flow.

Figure 8 shows the cell capture rolling and secondary adhesion at different starting position with positive initial shear rates of 9.06, 41.12 and 85.32 s<sup>-1</sup>.

It can be noted that the cell has the three stages of cell adhesion (capture, rolling and secondary adhesion) when it starts at  $G = 9.06$  (position of  $C_x/a_c$  of 169.7). But at higher shear rate (i.e., 41.12 and 85.32 s<sup>-1</sup>) the cell will roll slowly for short time before its rolling velocity gradually increases to reach a maximum value

as the shear rate gets higher (no adhesion and continuous rolling).

On the other hand, under most of negative shear rates (upstream of the stagnation point), the captured cell tends to adhere and stop rolling after certain period of time as demonstrated in Fig. 9. This indicates that cells within the effect of these shear rates ranges prefer adhesion after short slow rolling. As expected the cell in this area of flow, follows in the direction of shear rate, so its short rolling was toward the step to the left of the stagnation point, where the adhesion takes place under the negative shear rates.

In their experimental study, Skilbeck *et al.* [28] reported that within the circulation zone, wall shear stress was never so high as to disallow adhesion. This was not the case downstream the reattachment point in a high shear channel. Adhesion quickly dropped off beyond this point as wall shear stress increased. It was difficult to ascertain how many of cells that adhered beyond the reattachment point had been released from the vortex and how many had followed the streamlines that ran close to the wall upstream of the step and stayed downstream. Both types of attachment could be observed to occur occasionally.

To explore the cellular behavior downstream the step, more simulations were executed for different starting locations with dissimilar shear rates using the listed data of Table 1. The results of this simulation analysis are presented in Fig. 10.

By looking at Fig.10, it can be noted that cell adhesion is dominant within the distance between the step and the stagnation point (i.e.,  $C_x/a_c \leq 162$ ), the cells in this range roll shortly in the direction of shear rate (to the left) then adhere to the surface to form the whole/main part of the adhesion length. The cell keeps

on zero rolling velocity at the stagnation point ( $C_x/a_c = 162$ ), where no any previous rolling takes place, however as the starting location become far from the stagnation point under negative shear rate, the cell had short rolling before its permanent adhesion. Nevertheless, at the edge of the step the situation is considerably similar to that at the stagnation point.

On the other hand, under higher shear rate (to the right of stagnation point) the chance for adhesion decreases as the driving force (hemodynamic force) enlarges to enhance rolling. But at the closer locations ( $C_x/a_c = 178.28$ ), to the right of the stagnation point, cells tend to adhere for certain time before the drag force promote them for fast rolling (other end of the adhesion length).

Three conclusions can be assigned based on these findings: First, the discontinuity in the hemodynamic flow enhances cell adhesion under low shear rate at and downstream the disturbed portion in the flow (i.e., stenosis flow). Second, cell prefers to adhere to the surface between the discontinuity and little bit further the stagnation point, but the maximum tendency for adhesion is before the stagnation point, which synchronized with the lowest value of shear rate. This adhesion vanishes just further to the stagnation point where cell starts rolling at different velocities, as the shear rate gets higher. Third, after certain limit of shear rate the cell starts to roll with its maximum rolling velocity when shear is not constant; it increases with location to reach the maximum limit, where the maximum stream velocity takes place.

Based on the above situation, it is possible to determine the adhesion length around the stagnation point and the shear rate limit that allow for adhesion as explained in the next sections.

**Table 1.** Input setting for hemodynamics of disturbed flow under dynamic shear

Parameter	Symbol	Control Value
Cell radius ( $\mu\text{m}$ )	$a_c$	3.5
Characteristic Cell radius ( $\mu\text{m}$ )	$a_{co}$	3.5
Fluid dynamic viscosity ( $\text{g}/\mu\text{m} \cdot \text{sec}$ )	$\mu$	$7 \times 10^{-7}$
Fluid density ( $\text{g}/\mu\text{m}^3$ )	$\rho$	$1 \times 10^{12}$
Mass of the cell (g)	$m$	$1.8 \times 10^{-10}$
Mass moment of inertia of the cell ( $\text{g} \mu\text{m}^2$ )	$I$	$8.82 \times 10^{-10}$
Characteristic receptor density ( $\text{sites}/\mu\text{m}^2$ )	$[nR_{oo}]$	200
Receptor density ( $\text{sites}/\mu\text{m}^2$ )	$[nR_o]$	200
Ligand density ( $\text{sites}/\mu\text{m}^2$ )	$[nL_o]$	200
Bond stiffness (dyne/cm)	$S$	$1.5 \times 10^{-2}$
Transition bond stiffness (dyne/cm)	$S_{ts}$	$1.45 \times 10^{-2}$
Natural bond length ( $\mu\text{m}$ )	$L_{bo}$	0.011
Equilibrium bond formation rate constant ( $\mu\text{m}^2/\text{sites} \cdot \text{sec}$ )	$K_{fo}$	Changed from (0.08) to (0.016)
Equilibrium bond breakage rate constant (1/sec)	$K_{bo}$	Changed from (6.4) to (0.32)
Boltzmann's constant ( $\text{J}/^\circ\text{K}$ )	$K_B$	$1.381 \times 10^{-23}$
The temperature ( $^\circ\text{K}$ )	$T$	310
Shear rate ( $\text{s}^{-1}$ )	$G$	Variable (-58.72 - 100)
Characteristic shear rate ( $\text{s}^{-1}$ )	$G_o$	100

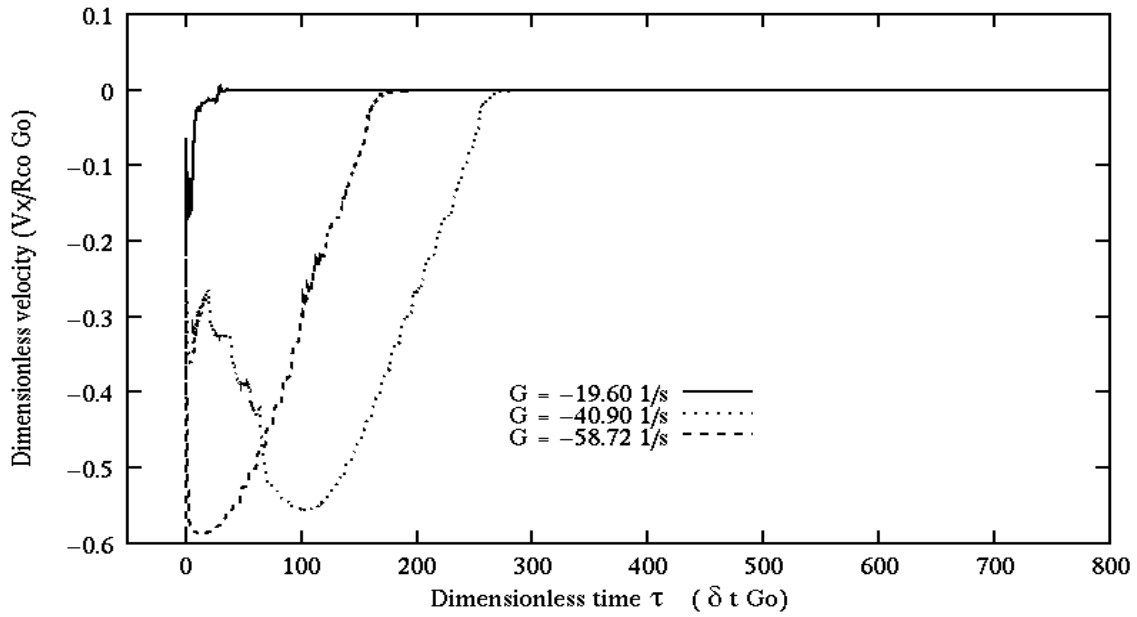


Figure 9. Cell capture and adhesion under range of negative shear rate (before the stagnation point location)

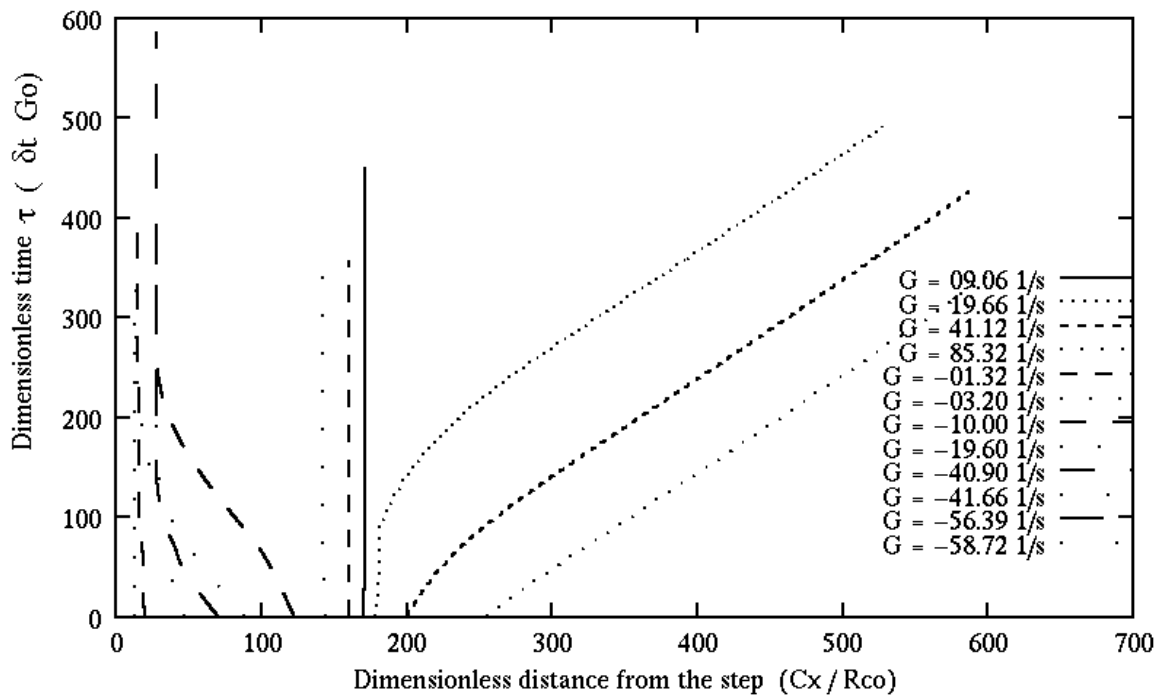


Figure 10. Cellular paths downstream the step (around the stagnation point) for different starting variable shear rate and different location from the step ( $R_{co} = a_{co}$ )

The present simulation was performed using relatively high site density and moderate site density, which means favorable conditions for adhesion. Mainly, the adhesion was dominant in the recirculation zone despite some rolling before the permanent arrest, while rolling has occurred -even under low shear rate- just at the far edge of recirculation zone (bit further the stagnation point). The short rolling downstream the step (recirculation zone) and fast rolling after the stagnation point can be explained by

the critical role of shear rate in cellular behavior within this area rather than the bond kinetics. Also, the rolling within the recirculation zone (low shear rate) is due to the rotational nature of flow (vortex) in this zone, where the shedding of vortices creates an oscillatory lift [20, 29, 30]. The shear rate in this type of flow had stronger effect than any other parameter, so it has strongly controlled the cellular behavior more than bond properties or site density. Accordingly, the results emphasizes that local fluid

dynamics (i.e., shear rate) of the complex flow plays a central role in cell adhesion and rolling within this type of flow, which dominant the other parameters roles [31].

In general, adhesion in the laminar re-established flow was as expected, being efficient at lower shear stress and negligible at higher rate. However, the lack of adhesion under low shear stress (downstream of the reattachment point) can be explained by the expansion of streamlines as they pass from narrower to wider conditions, so the cells effectively move away from the wall [28].

The above findings elucidate the details of cellular motion under disturbed flow, which can be used to explain cell adhesion under certain physiological conditions in the cardiovascular system. The pathophysiological implication of these results is that whereas adhesion may rarely occur in straight arteries, leukocyte could bind successfully in the region of a discontinuity. With regard to pathology, this may be a factor in localization of atheroma to low shear regions of vortices and recirculation associated with arterial junctions and curvature. Enhanced deposition could also influence process such as restenosis in vessels subjected to angioplasty, or thrombosis downstream of

anastomoses following surgical reconstruction of arteries [32].

**5. Ranges of Adhesion and Rolling for Disturbed Flow under Variable Shear Rate**

As an extension to the above analysis, more simulations were performed to determine the ranges of adhesion and rolling for disturbed flow under variable shear rate using data of Table 1 (Fig. 11).

In general, the analysis at this stage concentrate on the third step of cell adhesion and rolling, which is called ‘secondary adhesion’, ‘permanent adhesion’ or ‘arrest’. This type of adhesion is the final stage in the cellular behavior over the wall of the vessel, in addition, it is the dominant event downstream the discontinuity in the flow (Figs. 10 & 11).

Start of secondary adhesion depends on the bio-physicochemical properties of the bond and on the conditions of flow, also the starting time of secondary adhesion determines the end of cell rolling stage, range of adhesion and the shear rate limit for fast rolling.

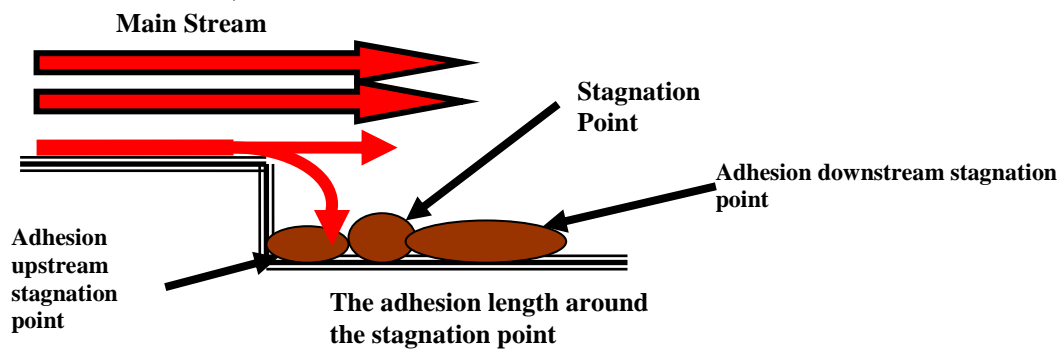


Figure 11. Upstream and downstream stagnation point adhesion for disturbed flow conditions

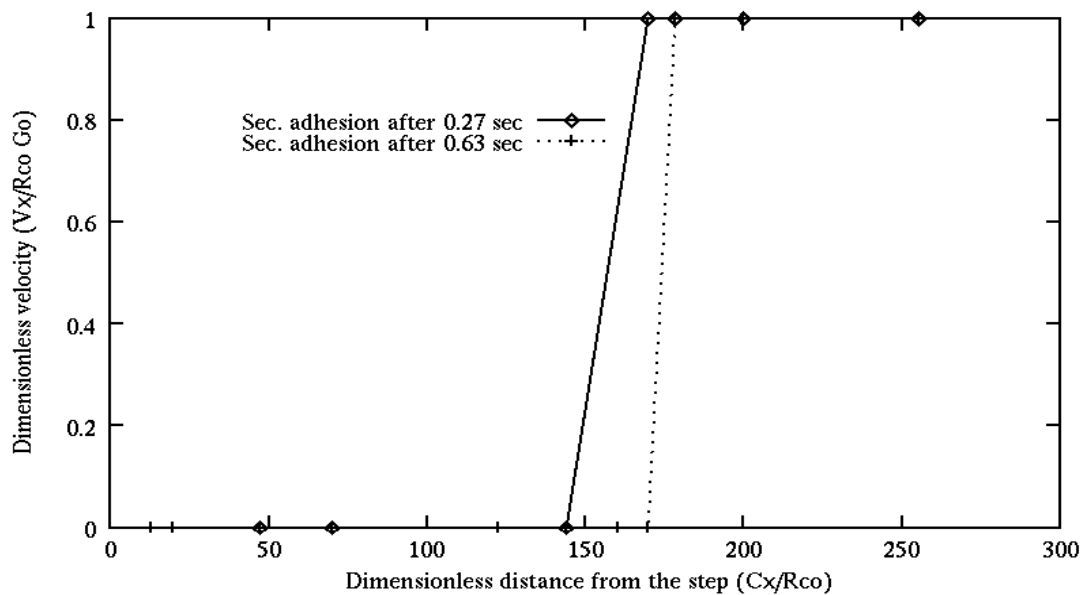


Figure 12. Effect of secondary adhesion start on cell-surface interactions under variable shear rate

In this analysis, the adhesion lengths around the stagnation point have been determined for two different starts of secondary adhesion. Moreover, the shear limits for adhesion and fast rolling were specified and compared to show the effect of secondary adhesion start on cell motion. The results of this analysis are illustrated in Figs. 12 and 13.

Figure 12 demonstrates that as the secondary adhesion starts earlier (early activation of cells that have primary adhesive rolling) the adhesion length will be shorter, so the adhesion length was within  $6.0 \leq C_x/a_c \leq 144.0$  (i.e., length of 483  $\mu\text{m}$ ), and fast rolling started at  $C_x/a_c = 169.7$  (i.e., at  $C_x \approx 594 \mu\text{m}$ ) when the secondary adhesion started at 0.27 sec. However, longer adhesion length was at later start of secondary adhesion (later activation of primary rolling cells). The adhesion was within  $6.0 \leq C_x/a_c \leq 169.7$  (i.e., length of 594  $\mu\text{m}$ ) at the secondary adhesion start of 0.63 sec., while the fast rolling started at  $C_x/a_c = 178.28$  (i.e., at  $C_x \approx 624 \mu\text{m}$ ). It can be noted that the adhesion in this case was on both sides of the stagnation point as it is located at  $C_x/a_c = 162.0$ .

Figure 13 shows the shear ranges for adhesion and rolling for secondary adhesion starts of 0.27 and 0.63 sec respectively. For 0.27 sec start, adhesion was taken place up to  $G/G_0$  of  $-0.196$  (i.e.,  $G = -19.60 \text{ s}^{-1}$  &  $C_x = 144 \mu\text{m}$ ) and the fast rolling limit was at  $G/G_0$  of 0.0906 (i.e.,  $G = 9.06 \text{ s}^{-1}$  &  $C_x = 169.7 \mu\text{m}$ ).

On the other hand, at 0.63 sec, they were  $G/G_0$  of 0.0906 (i.e.,  $G = 9.06 \text{ s}^{-1}$ ,  $C_x = 169.7 \mu\text{m}$ ) for end limit of adhesion and  $G/G_0$  of 0.196 (i.e.,  $G = 19.60 \text{ s}^{-1}$  &  $C_x = 178.28 \mu\text{m}$ ) for begin of fast rolling. This means that delay in starting of the secondary adhesion (delay of activation) allows the bonds to withstand more effect of drag force, and causes late cell rolling. Moreover, when the cell had long adhesive rolling under increasing shear rate before its secondary adhesion (late secondary adhesion start), the bond formation will be promoted to maintain the adhesive nature rolling. So when the secondary adhesion starts

under these conditions, another factor is added to support adhesion in the opposite of shear rate, which enable for longer adhesion length and delay fast rolling.

**6. Conclusion**

It is possible to determine cell adhesion location ranges, adhesion length and rolling limits for disturbed flow under variable shear rate. In addition, the adhesion length will be longer and on both sides of the stagnation point if the cell starts its secondary adhesion in a while, even though at higher shear rate. However, when the cell starts its secondary adhesion earlier, the adhesion will be shorter and mainly concentrated before the stagnation point, while rolling is dominant beyond this point.

These findings can be used to explain the cellular behavior (i.e., cell adhesion) at junctions, bifurcation and stenosis in the cardiovascular arteries. Also, clear idea can be obtained about cell type in regarding to its permanent adhesion, its ability to support adhesion/rolling and its kinetic activity (rates of bond formation and breakage) by analyzing the ranges of adhesion and rolling.

Another important point can be mentioned here, cell adhesion and rolling can be considerably controlled by secondary adhesion start technique. It is possible to extend or limit the ranges of cell adhesion or rolling under the same conditions of flow, by alteration of  $K_{bo}^-$  and  $K_{fo}^+$ , which means different type of bonds, furthermore, the timing of secondary adhesion has a particular role in cell motion. However, secondary adhesion can be also achieved using the same type of bonds, by changing of the site density or shear rate.

Finally, it is significant to remember that this technique can be employed to get more stable or low rolling under high shear rate or low site density to study the cell motion under wide ranges of parameters or more complicated flow conditions.

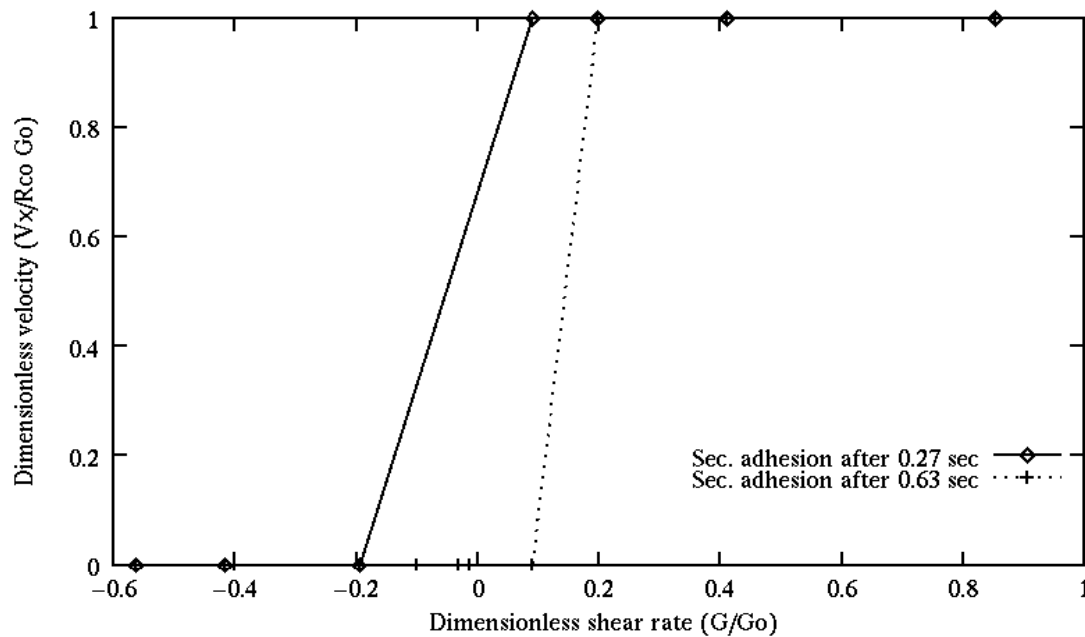


**Figure 13.** Effect of secondary adhesion start on shear rate limit for adhesion under variable shear rate

## References

- [1] Hammer, D. A., and Apte, S. M., "Simulation of cell rolling and adhesion on surfaces in shear flow: general results and analysis of selectin-mediated neutrophil adhesion," *Biophys. J.* 63, 1992, pp. 35-57.
- [2] Hammer, D. A. and Lauffenburger, D. A., "A dynamic model for receptor-mediated cell adhesion to surfaces," *Biophys. J.* 52, 1987, pp. 457-487.
- [3] Schmidtke, D. W., & Diamond, S. L., Direct observation of membrane tethers formed during neutrophil attachment to platelets or P-selectin under physiological flow, *The J. of Cell Biology*, Vol. 149, May 2000, 719-729.
- [4] Lei, X., Lawrence, M. B., & Dong, C., "Influence of cell deformation on leukocyte rolling adhesion in shear flow," *J. of Biomechanical Engineering, ASME*, Vol. 121, 1999, pp. 636-643.
- [5] Chen, S., & Springer T. A., "An automatic braking system that stabilizes leukocyte rolling by an increase in selectin bond number with shear." *The J. of Cell Biology*, Jan., Vol. 144, No.1, 1999. pp. 185-200.
- [6] Shao, J., Ting-Beall, H., & Hochmuth, R., "Static and dynamic lengths of neutrophil microvilli," *Proc. Natl. Acad. Sci., USA*, , Vol. 95, 1998, pp. 6797-6802
- [7] Malek, A. M., & Izumo S., Mechanism of endothelial cell shape change and cytoskeletal remodeling in response to fluid shear stress, *J. of Cell Science*, 109, 1996, 713-726.
- [8] Abueg, E., *The Effects of Flow on Adhesion Molecule Expression and Monocyte-Endothelial Interactions In Vitro*, Ph.D. thesis, Rensselaer Polytechnic Institute, Troy, New York, 2008  
<http://proquest.umi.com/pqdlink?did=1746891101&Fmt=14&VType=PQD&VInst=PROD&RQT=309&VName=PQD&TS=1274706241&clientId=79356>
- [9] Ravensbergen J. W. ; Krijger J. K., Hillen B., Hoogstraten H. W., "Localizing role of hemodynamics in atherosclerosis in several human vertebrobasilar junction geometries," *Arterioscler Thromb Vasc Biol.*; 18, 1998, pp. 708-716.
- [10] Swift, D. G., Posner, R. G., & Hammer, D. A., Kinetics of adhesion of IgE-sensitized rat basophilic leukaemia cells to surface-immobilized Antigen in Couette flow, *Biophys. J.*, Vol. 75, 1998, 2597-2611.
- [11] Bell, G. I., "Models for specific adhesion of cells to cells, *Science*," Vol. 200, 1978, pp. 618-627.
- [12] Dembo, M., Torney, D. C., Saxman, K., and Hammer D., "The reaction-limited kinetics of membrane-to-surface adhesion and detachment," *Proceeding R. Soc. London*, B234, 1988, pp. 55-83.
- [13] Krasik, E. F., Adhesive Dynamics Simulation of Neutrophil Arrest with Deterministic Activation, *Biophysical. J.* 91, 2006, 1145-1155.
- [14] Krasik, E. F., and Daniel A. Hammer, A Semianalytic Model of Leukocyte Rolling, *Biophysical. J.* 87, 2004, 2919-2930.
- [15] [http://mitocw.udsm.ac.tz/NR/rdonlyres/5059F757-7204-45F4-9409-EDC762C28456/0/lec\\_25\\_slides.pdf](http://mitocw.udsm.ac.tz/NR/rdonlyres/5059F757-7204-45F4-9409-EDC762C28456/0/lec_25_slides.pdf)
- [16] Goldman, A. J., Cox, R. G., and Brenner, H., "Slow viscous motion of a sphere parallel to a plane wall- I. Motion through a quiescent fluid," *Chemical Engineering Science*, 22, 1967, pp. 637-651.
- [17] Goldman, A. J., Cox, R. G., and Brenner, H., "Slow viscous motion of a sphere parallel to a plane wall- II. Couette flow," *Chemical Engineering Science*, 22, 1967, pp 653-660.
- [18] King, M., R., and Hammer, D., Multiparticle Adhesive Dynamics Interactions between Stably Rolling Cells, *Biophysical journal*, 81, 2001, 799-813.
- [19] Lawrence, M. B., and Springer, T. A., "Leukocytes roll on a selectin at physiologic flow rates: distinction from and prerequisite for adhesion through integrins," *Cell*, 56, 1991, pp. 859-873.
- [20] Dinnar, U., "Cardiovascular fluid dynamics", CRC press, Inc. Florida, USA, 1981
- [21] Bausch A. R., Moller, W., & Sackmann, E., Measurement of local viscoelasticity and forces in living cells by magnetic tweezers, *Biophys. J.* Vol. 76, Jan. 1999, 573-579.
- [22] Chang, K., Tees, D. F. J., & Hammer, D. A., The state diagram for cell adhesion under flow: Leukocyte rolling and firm adhesion, *Proc. Natl. Acad. Sci., USA*, Vol. 97, No. 21, Oct. 2000, 11262-11267.
- [23] Cozens-Roberts, C., Quinn, J. A., and Lauffenburger, D. A., "Receptor-mediated adhesion phenomena-model studies with radial detachment assay," *Biophys. J.* 58, 1990, pp.107-125.
- [24] Alon, R., Chen, S., Puri, K. D., Finger, E. B., & Springer, T. A., "The kinetics of L-selectin tethers and the mechanics of selectin-mediated rolling," *The J. of Cell Bio.* Vol. 138, No.5, 1997, pp. 1169-1180.
- [25] Tozeren, A. and Ley, K., How do selectins mediate leukocyte rolling in venules? *Biophys. J.* 63, 1992, 700-709.
- [26] Sinnott, M., Cleary, P. W., and Prakash, M., 2006, An Investigation of Pulsatile Blood Flow in A Bifurcation Artery Using a Grid-Free Method, Fifth International Conference on CFD in the Process Industries, CSIRO, Melbourne, 13-15-Dec. 2006, Australia- URL: [http://www.cfd.com.au/cfd\\_conf06/PDFs/119Sin.pdf](http://www.cfd.com.au/cfd_conf06/PDFs/119Sin.pdf)
- [27] <http://www.bakker.org/dartmouth06/engs150/11-bl.pdf> @ 20/5/2010
- [28] Skilbeck, C., Westwood, S.M., Walker, P.G., David, T., and Nash, G.B., "Dependence of adhesive behaviour of neutrophils on local fluid dynamics in a region with recirculating flow," *Biorheology*, 38 (2-3), 2001, pp. 213-227.
- [29] Fung, Y. C., "Biomechanics: Motion, flow, stress and growth", Springer-Verlag, New York, Inc. USA, 1990.
- [30] Massey, B. S., "Mechanics of fluids", 6<sup>th</sup> ed., Chapman & Hall, London, UK, 1988.
- [31] Chiu, J. J., Wang, D. L., Chien, S., Skalak, R., and Usami, S., "Effects of Distributed flow on endothelial cells", *J. Biomechanical Engineering*, Vol.120, 1998, pp.2-8.
- [32] Skilbeck, C., Westwood, S.M., Walker, P.G., David, T., and Nash, G.B., "Population of the vessel wall by leukocytes binding to P-selectin in a model of disturbed arterial flow", *Arterioscler Throm Vasc Bio*, 21, 2001, pp. 1294-1300.





الجامعة الهاشمية



المملكة الأردنية الهاشمية

المجلة الأردنية  
للمهندسة الميكانيكية والصناعية

JJIMIE

مجلة علمية عالمية محكمة  
تصدر بدعم من صندوق البحث العلمي

<http://jjmie.hu.edu.jo/>

ISSN 1995-6665

# المجلة الأردنية للهندسة الميكانيكية والصناعية

## مجلة علمية عالمية محكمة

المجلة الأردنية للهندسة الميكانيكية والصناعية: مجلة علمية عالمية محكمة تصدر عن  
الجامعة الهاشمية بالتعاون مع صندوق دعم البحث العلمي في الأردن

### هيئة التحرير

#### رئيس التحرير

الأستاذ الدكتور أحمد الغندور.

قسم الهندسة الميكانيكية و الصناعية، الجامعة الهاشمية، الزرقاء، الأردن.

#### الأعضاء

الأستاذ الدكتور ناصر الحنيطي  
الجامعة الاردنية

الأستاذ الدكتور محمد أحمد حمدان  
الجامعة الاردنية

الأستاذ الدكتور محمد هياجنه.  
جامعة العلوم والتكنولوجيا الاردنية

الاستاذ الدكتور نسيم سواقد.  
جامعة مؤتة

الاستاذ الدكتور أمين الربيدي.  
جامعة البلقاء التطبيقية

### فريق الدعم

#### تنفيذ وإخراج

م . علي أبو سليمة

#### المحرر اللغوي

الدكتور قصي الذبيان

ترسل البحوث إلى العنوان التالي

رئيس تحرير المجلة الأردنية للهندسة الميكانيكية والصناعية

الجامعة الهاشمية

كلية الهندسة

قسم الهندسة الميكانيكية

الزرقاء - الأردن

هاتف : 00962 5 3903333 فرعي 4537

Email: jjmie@hu.edu.jo

Website: www.jjmie.hu.edu.jo